MEASUREMENT OF THE COSMIC-RAY ENERGY SPECTRUM USING A NOVEL APPROACH TO MODEL THE APERTURE OF RADIO ARRAYS

Zur Erlangung des akademischen Grades eines
DOKTORS DER NATURWISSENSCHAFTEN (Dr. rer. nat.)
von der KIT-Fakultät für Physik des
Karlsruher Instituts für Technologie (KIT)

genehmigte

DISSERTATION

von

Vladimir Lenok, inzh. fiz. (M.Sc. äquiv.)

aus Angarsk

Karlsruhe
Dezember 2021

Tag der mündlichen Prüfung: 17.12.2021

Referent:	Prof. Dr. Frank Gerhard Schröder (Assistant Professor, University of Delaware, USA)
Korreferent:	Prof. Dr. Ralph Engel

ABSTRACT

Measurement of the Cosmic-Ray Energy Spectrum Using a Novel Approach to Model the Aperture of Radio Arrays

A WIDE RANGE OF QUESTIONS related to the most violent objects and environments in the Universe is closely related to cosmic rays of the highest energies, which are the most energetic nuclei ever observed. Those cosmic rays reaching the Earth's atmosphere initiate particle cascades called air showers. These nuclei are rare and observations of them in sufficient amount requires instrumentation covering large areas on the ground to detect the air showers initiated by them. These particle cascades generate radio emission which has been a subject of active research of the last two decades resulting in an accurate understanding of the emission mechanisms and in the development of reconstruction procedures capable to estimate the most important air-shower parameters from the measured radio signals. At present, the radio technique of air-shower measurements has matured and is ready for usage in upcoming large-scale cosmic-ray instruments.

The present work describes a calibration of the absolute energy scale of the Pierre Auger Observatory via the measurements of air-shower radio emission with the Auger Engineering Radio Array (AERA) and a dedicated end-to-end, full-fledged simulation study performed for cross-checking the energy scale obtained with the AERA measurements. The cross-check indicates that the obtained scales are close to each other.

The central topic addressed by this work is the estimation of the efficiency and aperture of a radio array. The physics of air-shower radio emission is such that the strength of the radio emission strongly depends on the incoming direction which affects the efficiency of a radio instrument and makes it dependent on the air-shower incoming direction. This behavior of the radio efficiency is unusual in comparison to other cosmic-ray detection techniques. Since the complexity of Monte-Carlo simulations of the air-shower radio emission hampers using them for accurate estimation of the radio efficiency, the present work presents a novel explicit probabilistic approach to this problem and develops a corresponding model, built for the Tunka Radio extension, Tunka-Rex, as an example. The unique location of Tunka-Rex at the site of the Tunka-133 Cherenkov timing array operating at full efficiency over the entire Tunka-Rex energy range allowed for a successful validation of the efficiency model not only against Monte-Carlo simulations, but also against observations.

The efficiency model was used to estimate the full efficiency regions of Tunka-Rex and calculate its aperture, which enabled the reconstruction of the cosmic-ray energy spectrum from the Tunka-Rex air-shower observations. This represents the first measurement of this kind performed with a cosmic-ray radio array.

ZUSAMMENFASSUNG

Messung des Energiespektrums kosmischer Strahlen mit Hilfe eines neuartigen Ansatzes zur Bestimmung der Apparatur eines Radioantennen-Messfelds

Viele Fragen über die energiereichsten Objekte und Umgebungen im Universum stehen in engem Zusammenhang mit der kosmischen Strahlung höchster Energien. Diese stellen die energiereichsten Atom Kerne dar, die je beobachtet wurden. Diese kosmischen Teilchen, die die Erdatmosphäre erreichen, lösen Teilchenkaskaden aus, die als Luftschauer bezeichnet werden. Um hochenergetische Luftschauer in ausreichender Menge zu beobachten, sind Instrumente erforderlich, die eine große Fläche am Boden abdecken. Die, Radioemission von Luftschauern war Gegenstand aktiver Forschung der letzten zwei Jahrzehnte, was zu einem besseren Verständnis der Emissionsmechanismen und zur Entwicklung von Rekonstruktionsverfahren führte, die in der Lage sind, die wichtigsten Luftschauerparameter aus den gemessenen Radiosignalen abzuschätzen. Diese Methoden zur Messung von Luftschauersignalen sind mittlerweile ausgereift und bereit für den Einsatz in zukünftigen grossflächigen Detektoren kosmischer Strahlung.

Die vorliegende Arbeit beschreibt die Kalibrierung der absoluten Energieskala des Pierre-Auger-Observatoriums anhand von Messungen der Radioemissionen von Luftschauern mit dem Auger Engineering Radio Array (AERA) sowie eine umfassende Simulationsstudie, die zur Überprüfung der, mit den AERA-Messungen erhaltenen, Energieskala durchgeführt wurde. Die Überprüfung zeigt, dass die ermittelten Skalen Konsistent sind.

Das zentrale Thema dieser Arbeit ist die Berechnung der Effizienz und der Apertur eines Messfelds von Radioantennen. Wegen der Physik der Luftschauerradioemission hängt die Stärke der Radioemission stark von der Einfallsrichtung ab, weshalb auch die Effizienz eines Antennefelder von der Einfallsrichtung abhängt. Dieses Effizienzverhalten ist ungewöhnlich im Vergleich zu anderen Methoden zum Nachweis kosmischer Strahlung. Die Komplexität von Monte-Carlo-Simulationen der Luftschauerradioemission erschwert ihre Verwendung für eine genaue Abschätzung der Radio-Detektioneffizienz. Deshalb wird in der vorliegenden Arbeit ein neuartiger expliziter probabilistischer Ansatz für dieses Problem vorgestellt und ein entsprechendes Modell entwickelt, das für die Tunka-Radio-Extenstion, Tunka-Rex, als Beispiel verwendet wurde. Die einzigartige Lage von Tunka-Rex am Standort des Tunka-133 Cherenkov-Timing-Arrays, das über den gesamten Tunka-Rex-Energiebereich mit voller Effizienz arbeitet, ermöglichte eine erfolgreiche Validierung des Effizienzmodells nicht nur anhand von Monte-Carlo-Simulationen, sondern auch anhand von Messdaten.

Das Effizienzmodell wurde verwendet, um den vollen Effizienzbereich und die Apertur von Tunka-Rex zu berechnen, was die Rekonstruktion des Energiespektrums der kosmischen Strahlen aus den Tunka-Rex-Luftschauermessungen ermöglichte. Dies ist die erste Messung dieser Art, die mit einem Antennefeld durchgeführt wurde.

CONTENTS

INTRODUCTION

Cosmic rays are an important component of the Universe, containing a significant part of its total energy and participating in many processes that form observable objects and phenomena. The present work is devoted to cosmic rays of the highest energies, the relativistic nuclei carrying information about the most violent objects and environments.

A special interest towards the cosmic-ray research stems from its connection to a wide range of the unsolved astrophysical problems. The main problem is understanding the origin of cosmic rays of the highest energies. The others include the origin of the cosmic-ray spectrum and the cosmic-ray mass composition, effects of the cosmic-ray propagation in the Galactic and intergalactic media, acceleration of the nuclei in jets and shocks. Moreover, a special group of open questions is related to the physics of hadronic interactions at the highest energies and in kinematic regimes not accessible at the modern particle-acceleration experiments. All these questions related to the cosmic-ray research are essential for the coherent understanding of our Universe.

The cosmic rays of the highest energies are rare. At present, it is only possible to study them indirectly, by observing air showers they produce as they enter the atmosphere. Particles of the air showers and radiations emitted by them propagate through the atmosphere and can be detected on the ground with arrays of particle detectors of various kinds, special telescopes, or arrays of radio antennas.

The fact that air showers generate radio emission during their development was discovered in the 1960's after a theoretical work suggesting an existence of such emission. After about a decade of extensive observational and theoretical research, the interest towards these kind of measurements started to disappear since in those times the radio technique did not provide a reliable estimation of parameters of air showers from the observed radio signals. Nowadays, the advances of electronics and computers have allowed for reliable estimation of air-shower parameters, which are renewing interest towards the radio technique. The extensive studies of the radio emission performed in the 2010's with modern approaches to measurements and simulations settled our knowledge on the radio emission mechanisms and provided reliable methods capable to estimate the cosmic-ray energy and the depth of shower maximum from the measurements. This progress brought us to the stage where the radio technique can provide measurements competitive to the other techniques and bring its advantages to cosmic-ray research.

To derive accurate astrophysical conclusions from cosmic-ray measurements they should have, among other characteristics, an energy scale as accurate as possible. The Pierre Auger Observatory, which operates the world's largest cosmic-ray detector complex, uses measurements of the air-shower fluorescence light as an established technique for the energy scale calibration. An alternative technique for this purpose can be the measurements of the air-shower radio emission, which is closely related to the electromagnetic component of air showers, the same as the fluorescence light, but is available almost

all the time rather than only in clear nights. The present work describes a simulation study performed for the Auger Engineering Radio Array (AERA). The essential idea has been to process air-shower simulations with the complete detector response and the realistic reconstruction for obtaining the absolute energy scale, and, then, compare it with the energy scale obtained from an analysis of the AERA measurements.

The efficiency and aperture of an air-shower radio array and their estimation are the central topic of this work. The advances of the last decade suggest that the next logical step in the development of the radio technique is studying the cosmic rays as an astrophysical phenomena rather than the individual air-showers they produce. Proper understanding of the efficiency and aperture becomes essential in this stage. In contrast to the other techniques, the nature of the radio emission causes an unusual behavior of the instrument efficiency as function of the air-shower incoming direction. A large computational complexity inherent in the Monte-Carlo simulations of the radio emission limits their applications for studies of the efficiency and aperture. It is extremely challenging to produce a sufficient amount of simulations required for a fine coverage of the instrument area and the range of incoming directions. Thus, the problem of the efficiency and aperture estimation for a radio array was not solved satisfactory up to now. The present work describes a new approach to this problem and presents a corresponding model based on an explicit probabilistic treatment of the radio emission footprint and the process of signal detection. The model is applied to the Tunka-Rex array as an exemplary radio instrument. The Tunka-Rex array is a unique instrument for studying the efficiency of a radio array since its triggered with the Tunka-133 array, which is fully efficient in the entire energy range relevant for Tunka-Rex. Thus, it was possible to validate the model of the Tunka-Rex efficiency not only against Monte-Carlo simulations, but also against the observational data. The developed model has a generic nature. With appropriate adaptations it can be applied to any cosmic-ray radio array.

Knowledge of the comprehensive behavior of the efficiency enables the estimation of a full-efficiency region in sky coverage and energy and the estimation of the corresponding aperture. It was found that the two-dimensional aperture integral can be solved semi-analytically with high accuracy. The newly developed model for aperture calculation and the updated reconstruction of the air-shower parameters provide all necessary components to reconstruct the cosmic-ray energy spectrum based on the radio measurements only.

CHAPTER ONE

COSMIC RAYS

The present Universe is a composition of dark energy, dark matter, and ordinary matter with relative fractions of about 0.70, 0.25, and 0.05 respectively [1]. All of them together comprise the essential subject of astronomy and astrophysics — celestial objects united in galaxies, interstellar and intergalactic gas and dust pierced by cosmic rays, neutrinos, and photons of various frequencies. These components form a large and complex system.

Cosmic rays are defined as the charged component of cosmic radiation [1, 2]. They include high-energy nuclei and elementary charged particles, like electrons and positrons. The phenomenon of cosmic rays was discovered in the beginning of the last century as a result of extensive research on the ionization radiation observable everywhere around the globe and of unknown origin [3]. The term "cosmic rays" may seem a bit archaic nowadays, but back then it reflected the fact that neither nature nor content of this radiation was known, and it was initially believed by some that they were photons of high penetration power [4]. However, already early deep investigations revealed that this initial hypothesis is not correct [3].

The energy density contained in the cosmic rays, about 1 eV/cm^{-3} [5] in the Galaxy, reveals their significance in the structure of the Universe. A comparison shows that they are as significant as the interstellar magnetic fields, the local density of the starlight, and the cosmic microwave background. The interstellar magnetic field has an energy density about 2 eV/cm^{-3} for a magnetic field of about 7 µG, which is typical for radio-faint spiral galaxies like ours [6]. The local energy density contained in the starlight is about 0.4 eV/cm^{-3} [7]. The energy density of the Cosmic Microwave Background is also about 0.3 eV/cm^{-3} [1].

Consideration of the energy density of the highest-energy cosmic rays shows that it is on the same level as those for neutrino and photons of the highest energy (Figure 1.1 shows the cosmic ray flux scaled with square of kinetic energy which is proportional to the energy density of the cosmic rays per decade). These similarities suggest a close link between all these components [8].

Cosmic rays are an essential component of the Universe. On the one hand, they are important by themselves. They play a crucial role in forming the chemical composition of the interstellar medium, heating the interstellar gas, and determining the dynamics of the molecular clouds [9]. In turn, this influences star formation and the evolution of galaxies [10]. Cosmic rays cause diffuse electromagnetic radiations close to their sources

and during their propagation in the interstellar medium [2, 11, 12]. On the other hand, along with others, cosmic rays are messengers of the non-stationary, non-thermal, and high-energy processes in the Universe [11, 13]. The origin and exact nature of the cosmic rays, especially of the highest energies remain not fully understood [14].

1.1. ENERGY SPECTRUM

One of the most important features of the cosmic rays is the spectrum of their energies. Figure 1.1 shows a collection of the recent measurements of the cosmic-ray flux as a function of kinetic energy for selected nuclei: hydrogen [15–17], helium [16–18], oxygen [5, 18–20], and iron [5, 19, 20], for all cosmic-ray charged particles [21–27], electrons [28, 29] and positrons [30, 31], antiprotons [32, 33], photons corresponding to the extra-galactic radiation background [34], and astrophysical neutrinos [35]. The spectra are scaled with the square of the kinetic energy. This transformation makes the scaled values proportional to the energy density per decade of energy. The left-hand side of the plot contains the data of the direct measurements performed in space and high-altitude atmospheric flights. The right-hand side of the plot contains the data on the all-particle spectra of the cosmic rays obtained indirectly, with air-shower observations. The labels indicate prominent features of the all-particle spectrum.

The energy spectrum reveals several striking features. First of all it clearly shows that the nature of cosmic rays is far from thermal since their spectrum does not follow the Planck's law. The cosmic-ray energies span over more than thirteen orders of magnitude and their flux dramatically varies from about one particle per square meter per second at 100 GeV to about one particle per square kilometer per year at 5 EeV. Recent measurements made by the Voyager probes provided evidences that outside of the heliosphere cosmic rays have energies down to 10 MeV. Close to the Earth their energies span from about 1 GeV, where the solar magnetosphere influence becomes less significant, to the energies of a few hundred EeV, corresponding to the energy estimations of the most energetic cosmic rays observed to date. The overall spectral shape of all components and complementary radiations obeys power laws.

Another neutral component shown on the plot is the best estimation of the astrophysical neutrino flux from the observations as a corresponding band of 68% confidence interval.

Recent years brought discoveries and results over the whole range of the cosmic-ray energies. The following paragraphs cover some of the most outstanding ones.

1.1.1. Low-Energy Cosmic Rays

The lowest energy cosmic rays observable close to the Earth, with energies below about 10 GeV, come to the Solar System from the Galaxy by diffusing through the solar wind outflowing magnetized plasma. The solar plasma decelerates the cosmic rays and partially removes them from the internal part of the solar system, which causes variations in the flux observed over the solar cycle. This effect is known as solar modulation. Solar activity

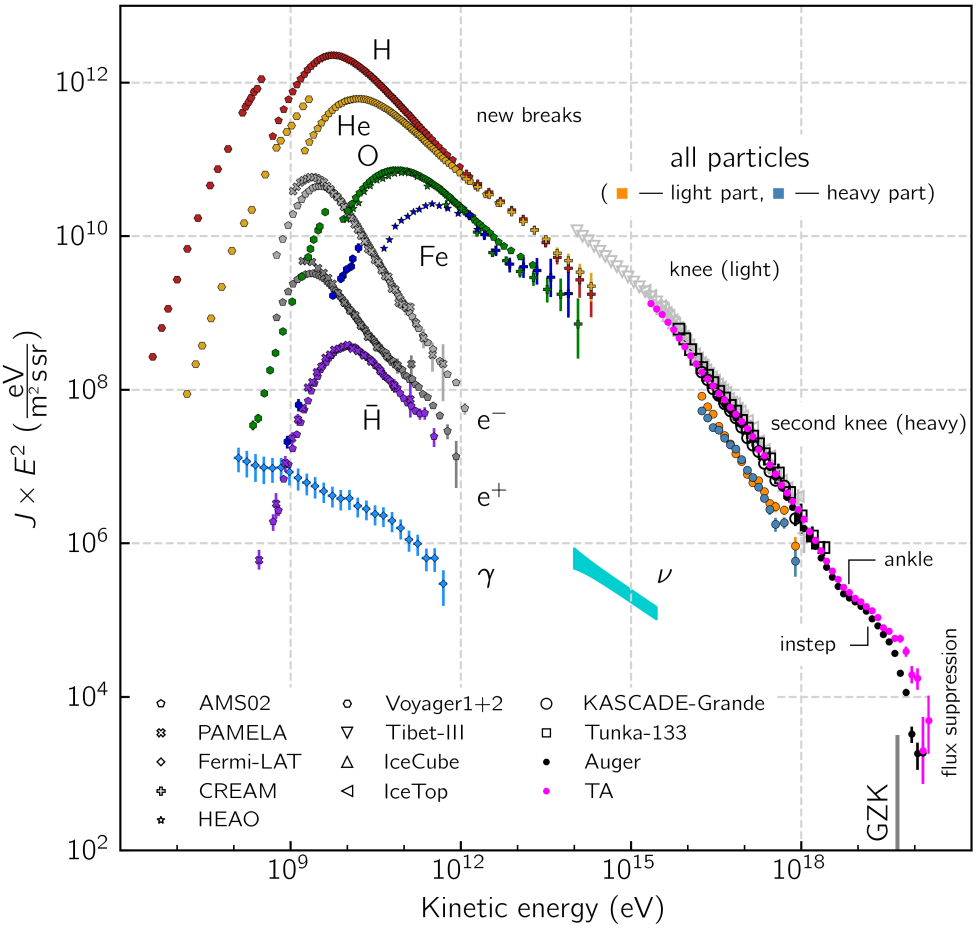

Figure 1.1: A collection of selected contemporary measurements of the cosmic-ray energy spectrum and high-energy neutral messengers (gamma-rays and neutrinos). The labels indicate the corresponding type of the nuclei or electrons, positrons, photons, neutrino. The scaling of the spectrum with the square of the energy gives a quantity proportional to the energy density of cosmic rays, photons, or neutrinos per energy decade. The data for the plot are taken from the following databases [36–38].

changes the observed flux of the low-energy cosmic rays so that their flux drops during the phases of solar activity and rises while the Sun is quiet [39, 40]. The phases of solar quietness allow for measurements of the cosmic-ray fluxes without large disturbances.

Recently, it became possible to measure low energy cosmic rays outside of the Solar System. It happened due to a remarkable event — the Voyager probes crossed the heliopause [5, 17], the boarder of our solar system defined by location where the solar wind is stopped by the interstellar medium. Now these probes provide observations of

the cosmic rays directly in the local interstellar medium. The most important feature of these observations is that the solar activity does not affect the cosmic-ray flux in that region. The results of these observations are depicted in Figure 1.1. The shapes of the spectra show that the spectral indexes of various resolvable components are similar.

1.1.2. Medium-Energy Cosmic Rays

Recent measurements of cosmic rays in the energy region from about 10 GeV to about 1 TeV reveal the clearest picture of this energy region, yet. This provided the discovery of several new features opening new problems in astrophysical research[1].

On the one hand, it was discovered and recently confirmed that the fraction of positrons in cosmic rays increases with energy starting from about 100 GeV [42–44]. This observation is in contradiction with earlier theoretical models even though earlier observations showed indications of this effect [45]. On the other hand, other components like the ratio of hydrogen to anti-hydrogen, and the ratio of boron to carbon, do not show such an increase [46–48]. The observations of the electron spectrum reveals its relatively flat behavior [28, 29].

Even more discoveries happened recently in the realm of cosmic-ray nuclei astrophysics. The recent data provide clear evidence that the helium spectrum is flatter than the hydrogen one. This spectrum shape might provide an important clue on the helium acceleration mechanisms that are not fully understood yet [16–18].

Another discovery related to helium and hydrogen astrophysics is detecting breaks in the hydrogen and helium spectra at the same rigidity [15, 49, 50]. Also, there are hints that heavier nuclei have breaks at the same rigidity. Such a correlation most likely is not occasional and suggests a closeness in their origin.

A very important realm of the cosmic-rays is the study of antimatter. The measurements of the ratios of antiprotons to protons, protons to positrons, and positrons to antiprotons reveal that these ratios are almost energy independent in a wide energy range [32]. This fact supports a hypothesis about the origin of the positrons in shock waves, but not in pulsars or the dark matter annihilation.

Radioactive isotope detection provides a piece of important historical information. An analysis of recent heavy-ion measurements showed the presence of the ^{60}Fe radioactive isotope in the cosmic rays. The presence of such an unstable isotope tells us about an explosion of a supernova close to the Earth a few millions year ago [51].

1.1.3. High-Energy Cosmic Rays

At energies of around a few PeV, the general behavior of the all-particle spectrum changes. The spectral index gradually deviates from 2.7 to larger values around 3.0 forming a kink in the slope, the so-called “knee,” at about 3 PeV [52]. Then the flux falls further down, forms another kink, the “second knee,” at about 100 PeV [53–57], and continues to fall until the energies where the spectral index rises once again at the “ankle.” The

[1]The following content in this section is inspired by [41].

cosmic rays from this wide energy range from about 500 TeV to about 1 EeV form a special energy region where one expects to observe a transition of the cosmic-ray origin from the galactic to extra-galactic due to the fact that the Galaxy with its size and magnetic fields cannot hold the cosmic rays of high- and ultra-high-energies [58, 59].

Starting from these energies and higher, the state-of-the-art technologies allow for measuring only all-particle spectra and mass groups but do not provide a way to deduce information about individual nuclei. Despite this, recent data provide vital information about this energy region, which indicates the nature of the cosmic rays at these energies.

The mass sensitive measurements provided evidence for rigidity-dependent break in the region between the two apparent kinks in the energy spectrum (the "knee" and the "second knee") [24]. It can be seen in Figure 1.1 as two additional spectra for the light and heavy parts of the all-particle spectrum. They indicate that the relatively light composition at the knee gradually changes to the relatively heavy composition at the second knee. This finding might be the first evidence of a Peters' cycle [60, 61] — a series of rigidity dependent cutoffs in energy spectra of individual nuclei, which appears as a smooth feature of the all-particle energy spectrum. Although, the specific sources of the cosmic rays at this energy region are not known, the plausible possibility of presence of a Peters' cycle provides an important clue paving a way towards the source identification.

1.1.4. Ultra-High-Energy Cosmic Rays

After the apparent break at 100 PeV, the cosmic-ray energy spectrum keeps dropping till it hardens at about 5 EeV energy and finally reaches a region of suppression with the most energetic cosmic rays ever observed yet. The cosmic rays of energies above about 1 EeV are refereed to as ultra-high-energy cosmic rays.

Recently, statistically accurate observations from the Northern and Southern hemispheres brought new insights into this highly energetic cosmic rays whose origin and nature remain not fully understood. First, these measurements [26, 27] confirmed previously known spectral features: a spectral kink at 5 EeV, known as "ankle" [55, 57, 62, 63], and the suppression above 50 EeV [63]. Second, the measurement revealed a new feature — an "instep" at 13 EeV in the all-particle spectrum [64, 65]. These breaks are likely not isolated features but a part of more general picture. It is likely that the appearance of the whole region results from the composition of the spectra of individual nuclei, each with a cutoff at a specific energy. There exist few scenarios for the explanation of the overall sequence of the spectral kinks of the individual nuclei:

The first scenario is that the structure of the energy region is formed by propagation effects of the cosmic rays through the intergalactic and galactic photon fields. On the course of propagation from the sources to the Earth, nuclei interact with photons that cause photoproduction and photodisintegration of new particles. The most known effect of this kind is the so-called Greisen–Zatsepin–Kuz'min (GZK) cutoff [66, 67], which is simply the known reaction of photoproduction of pions by protons on the photons of the Cosmic Microwave Background (CMB) in the kinematics relevant for the cosmic-

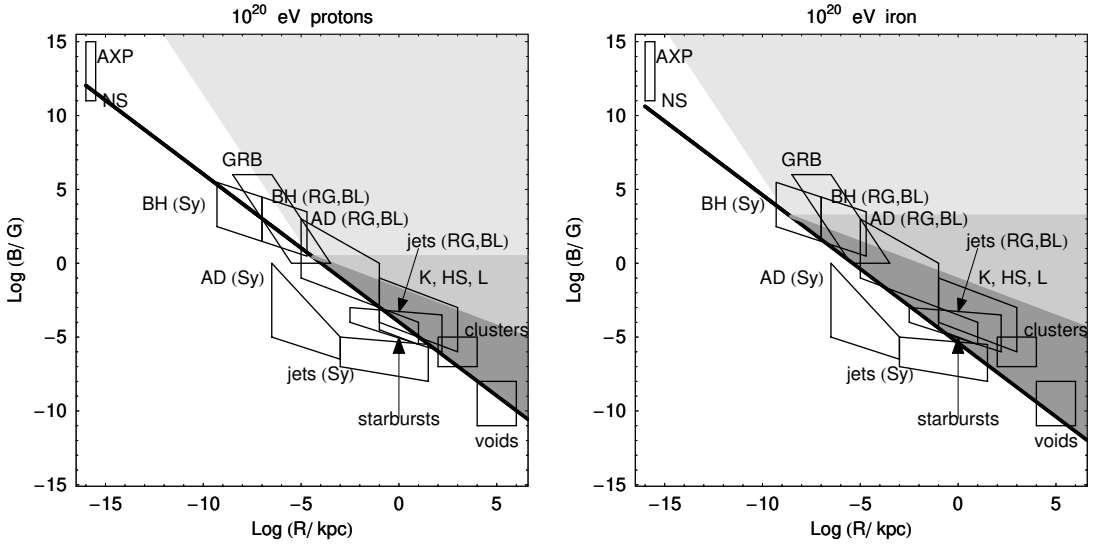

Figure 1.2: The contemporary version of the Hillas diagram [58]. The plots summarize the size and magnetic fields of various sources and depict the areas required for accelerating proton and iron to the energy of 10^{20} eV. The bold line corresponds to the lower boarder of the area allowed by the Hillas criterion. The gray areas correspond to the regions allowed by different models of the accelerating and radiative losses. The plot presents information about the following objects: neutron stars (NS), anomalous X-ray pulsars and magnetars (AXP), supermassive central black holes (BH) of active galactic nuclei, central parsecs (AD) of active galaxies, relativistic and non-relativistic jets, starburst-galaxies, gamma-ray bursts (GRB), galaxy clusters, inter-cluster voids, and knots (K), hot spots (HS), and lobes (L) of powerful active galaxies (RG and BL). The galaxy types, specified in the brackets, are: Seyfert galaxies (Sy), powerful radio galaxies (RG), and blazars (BL). The diagram is taken from [59].

ray propagation. The cutoff happens at the energy of propagating protons of about $5{\times}10^{19}$ eV. The propagation of heavier nuclei through the CMB photon field causes similar cutoffs but at lower energies, but remain similar for iron nuclei. For processes occurring during the propagation nuclear effects become crucial. One of the most relevant processes during the propagation is the process of photodisintegration, the process of a transformation of a nuclei into a nuclei of another type after an interaction with a photon. This process causes a gradual change of the cosmic-ray mass composition during the propagation and corresponding change of the energy spectrum. This and other nuclear processes relevant for cosmic-ray physics are complex and nucleus specific [14, 68].

The cosmic-ray acceleration sites reaching their maximum energy constitutes the second possible scenario. Disregarding the particular acceleration mechanism, the maximum energy of a nucleus depends on its charge. Hence, the maximum energy must be proportional to the charge. Thus, in the framework of this scenario, the energies, at which the kinks in the spectra of individual nuclei are located, increase with increasing nucleus charge [58, 59].

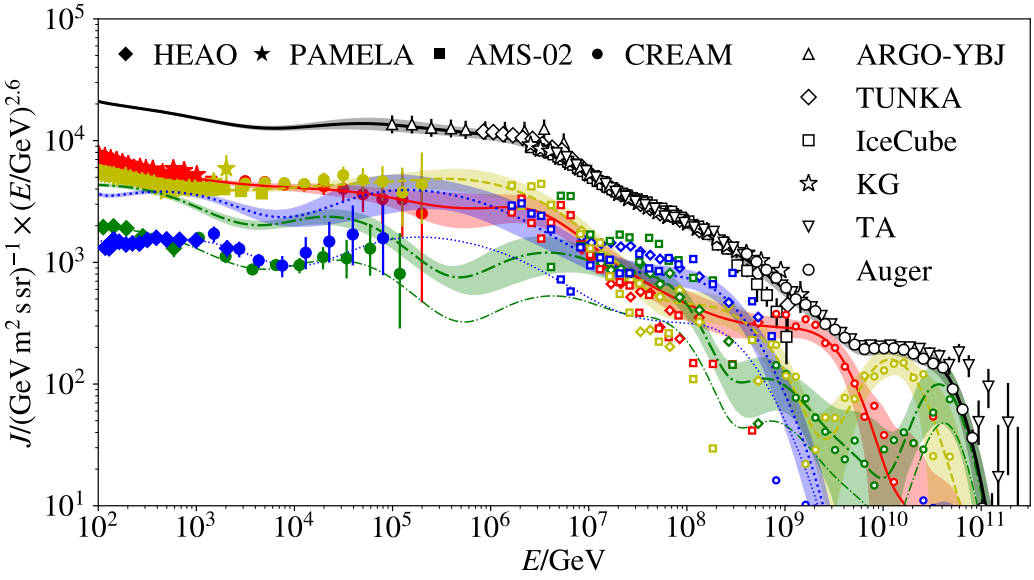

Figure 1.3: The estimation of the energy spectrum for all cosmic rays and individual nuclei groups (represented by corresponding 68% confidence intervals of the individual nuclei groups depicted by different colors; red — hydrogen, yellow — helium, green — oxygen group, blue — iron group). The plot is taken from [70].

Even though the latest mass-composition measurements favor the second scenario, they are not entirely conclusive, which makes it difficult to distinguish which scenario is dominant [69]. Future observations with higher exposures might resolve the puzzling nature of the most energetic particles in the observable Universe.

The presence of the ultra-high-energy cosmic rays is challenging to explain. The acceleration mechanisms capable to provide nuclei with a spectral shape and energies close to the observed ones are not fully understood for the time being [71]. A reliable generic way to assess capabilities of potential sources to accelerate nuclei to certain energies is a so-called Hillas criterion. The essence of the criterion lies in the assumption of gradual modes of acceleration, where particles move within the source while gaining energy. Thus, the accelerator magnetic field and geometrical size of a source should be sufficient to hold nuclei of certain energies. In other words, the gyro-radius of a nucleus moving in the magnetic field of the source should be smaller than the size of the source. The criterion was originally suggested in [58]. The recent updates of this considerations also include constrains coming from the radiation losses presented in [59]. Figure 1.2 shows a contemporary version of the Hillas diagram from this work.

The uncertainties of air-shower measurements of the cosmic-ray properties do not yet allow for distinguishing energy spectra of the individual nuclei, which would be a powerful clue to resolve the problem of acceleration mechanisms and the problem of transition from the galactic to extragalactic sources. Various models of the cosmic-ray flux exist [72–

76], however, all of them are built on particular assumptions on the cosmic-ray sources, details of their spectrum, and propagation effects. Recently, a new assumption-free model was created (Figure 1.3). The model is a result of a new data-driven approach to the flux parametrization. The approach is to use the data from the directly measured spectra of individual nuclei and indirectly observed all-particle spectrum and nuclei-group spectra wherever they are known and to perform a global spline fit to this data. Due to this, the model is known as the Global Spline Fit model [70].

1.2. AIR SHOWERS

A cosmic ray of sufficiently high energy entering the atmosphere travels through the air until it collide with a nucleus. This interaction initiates an extensive air shower — a cascade of secondary particles produced in consecutive interactions of the particles with the atmospheric nuclei and in particle decays. Let us consider the typical details of this process for a cosmic ray of the ultra-high energy.

After entering the atmosphere, the cosmic ray propagates through its rarefied part without interactions. Reaching a denser part of the atmosphere it collides with a nucleus and creates a large number of secondary particles (Figure 1.4). The products of this collision are light mesons, mainly pions, light baryons, protons and neutrons, and other particles in a much smaller amount. These secondary particles propagate further and create more particles in the consecutive collisions with atmospheric nuclei. The energy of the cosmic ray is distributed over the secondary particles of the cascade. Every collision shares the energy of the initial particle among the products; thus, the kinetic energies of the secondary particles created in consecutive reactions rapidly drops. When the energies of the particles become lower than the threshold energy required to create new particles, the cascade diminishes.

Air shower has three distinctive components [2, 77, 78]: electromagnetic, muonic, and hadronic. Let us consider the most important processes contributing to the cascade development.

In hadronic cascades, short-living unstable particles that decay in the atmosphere contribute the most to the cascade development [79]. The most common particles of this kind are pions. The neutral pion lifetime[2] is $8.52(18) \times 10^{-17}$ s. Their main decay mode is into two photons

$$\pi^0 \to \gamma + \gamma$$

happening with a probability of 98.823(34)%. The photons produced by this reaction have sufficient energy for producing electron and positron pairs in the electric fields of the atmospheric nuclei

$$\gamma + \gamma \to e^- + e^+,$$

which initiates an electromagnetic cascade due to the electron bremsstrahlung. There

[2] All numerical values for particle lifetime, decay modes and their probabilities given within this section are taken from [1].

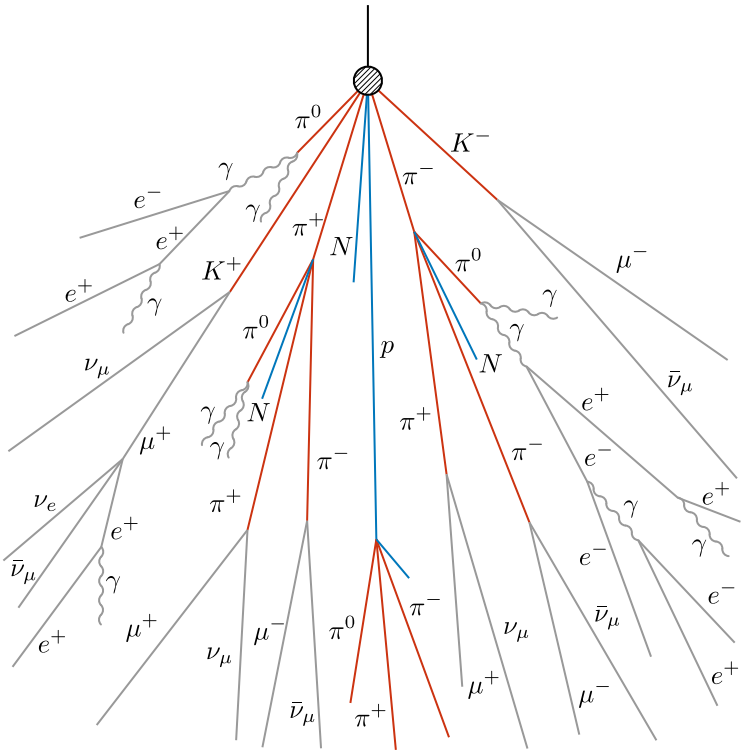

Figure 1.4: Sketch of an air-shower. The sketch represents a generic idea of the cascade development. The incoming cosmic ray (the top vertical line) collides with a nucleus in the atmosphere. The first interaction (hashed circle hides the detail of the interaction) ends with the first secondary particles that interact and decay further. The gray lines represent leptons, the red lines represent mesons, the blue lines represent other baryons.

are only three processes relevant for driving the development of the electromagnetic cascades. A fast electron or positron can produce a photon in bremsstrahlung radiation process or, if it has lower energy, bring into the cascade more electrons by ionization of the atmospheric atoms. A photon with a sufficient energy can create a pair of an electron and positron in the atomic field in the same manner as mentioned above. The interplay of these processes between photons, electrons, and positrons creates several generations of such particles forming the cascade. On the course of the propagation through the atmosphere, the particles forming the electromagnetic cascade are subject to multiple Coulomb scattering on the atmospheric atoms causing the spread of their lateral distribution [2, 78, 80–86].

The charged pions have a lifetime of $2.6033(5) \times 10^{-8}$ s that is much longer than that of the neutral pions. Such a long lifetime allows for propagation of this kind of pions for significant distances in the atmosphere before they decay. The main decay mode, happening in 99.98770(4)% of the cases, is the creation of a muon and a muon neutrino. Depending on the pion charge the modes are

$$\pi^+ \to \mu^+ + \nu_\mu \qquad \text{and} \qquad \pi^- \to \mu^- + \bar{\nu}_\mu.$$

The muons created in these decays contribute to the muonic part of the cascade. The muons are unstable with a lifetime of $2.1969811(22)\times10^{-6}$ s. They decay into an electron and neutrinos

$$\mu^- \to e^- + \bar{\nu}_e + \nu_\mu \qquad \text{and} \qquad \mu^+ \to e^+ + \nu_e + \bar{\nu}_\mu.$$

However, the muon lifetime is quite large and the majority of the muons created in the cascade reach the ground level due to the time dilation. Their common observation is a great every-day example confirming the special relativity theory.

The light baryons are produced in the first collision and further in interactions within the cascade form the hadronic part of the cascade. Interactions of these baryons with atomic nuclei produce mainly pions that decay afterwards contributing to the electromagnetic and muonic part of the cascade. The physics describing the interactions of the first cosmic-ray interaction and further baryon interactions is not entirely understood yet and nowadays constitutes the main uncertainty in the description of the hadron-induced cascades (see the current status of the field in [69, 87]).

Recent measurements of muons in a wide range of shower energies revealed that the hadronic models developed up to now do not describe this component of the cascade well enough [88, 89]. This discrepancy additionally limits the present mass-composition measurements and impose queries towards our knowledge of the high-energy hadronic interactions [69].

Description of air showers is one of the central problems in the cosmic-ray research. Fist analytical models of air showers started to appear in the late thirties and were mainly focused on the electromagnetic showers and understanding the mechanisms of the underlying cascade process [80, 81, 90]. With progress of particle physics, it was quickly realized that the complexity of the hadronic interactions, especially at the high energies, hampers to use analytical techniques for the hadronic air shower and some numerical methods should be used for modeling and simulations [91, 92]. The situation did not change much since those early times [69]. The hadronic interactions remain a complex scientific topic up to date and the theory describing them remain a topic of active research [93]. In addition to this, the forward kinematics of air showers poses another problem since it requires using phenomenological models of hadronic interactions rather then the highly accurate perturbative techniques used for center-to-center collision description and processes with high momentum transfer. The various phenomenological models and numerical techniques implemented in the modern software addresses all these complexities [94–97].

The modern software can be split into two logical branches: the software numerically solving the cascade equations [98] and the software numerically generating realistic air showers or the so-called event generators [99–101]. If the former software is useful for studying physics of air showers and influence of different models to the macroscopic properties of air showers, the later software is the tool actively used for research involving interaction of air-shower particles and radiations they produce with instrumentation.

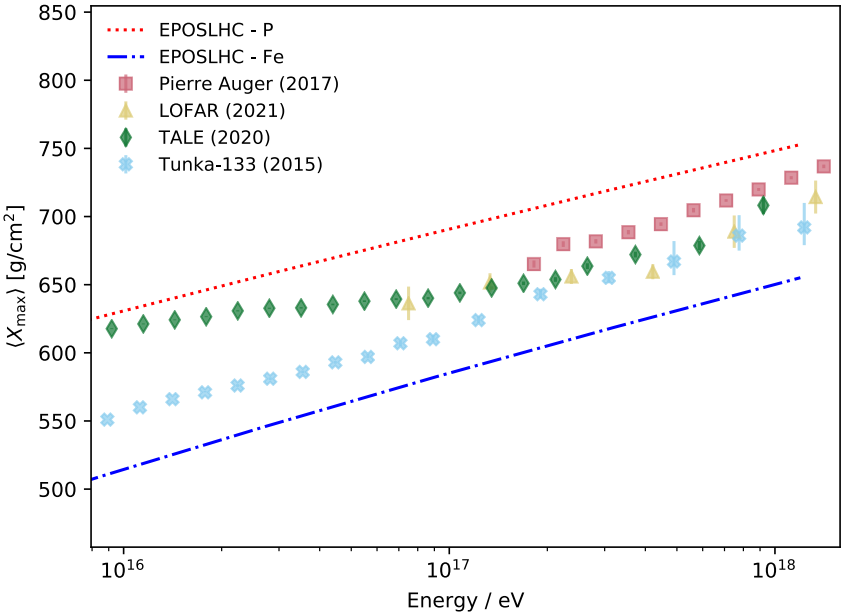

Figure 1.5: Collection of recent measurements of the averaged X_{max}. The red and blue lines show the corresponding model prediction with EPOS-LHC model for describing the high-energy hadronic interactions. The plot is adopted from [102].

Throughout this work the CORSIKA software was used for all air-shower simulations. The main motivation for this choice is that this software is an in-house development of the Karlsruhe Institute of Technology, where the present work was performed.

1.3. X_{MAX} PARAMETER MEASUREMENTS

The X_{max} parameter is another important observable after the cosmic-ray energy. It is sensitive to the mass of the cosmic-rays initiating air showers. Thus, X_{max} measurements provide insights to the cosmic-ray mass composition, which, in turn, imprints the properties of both, the cosmic-ray accelerators and the cosmic-ray propagation [61].

The present capabilities of technology for direct observations limit the achievable exposure of the instruments measuring cosmic rays. Thus, direct observations are sensitive to only relatively large cosmic-ray fluxes, limiting the directly observable energy range. Ground-based observations are the only possibility nowadays to study the cosmic rays of PeV energies and higher. The ground-based observations are possible essentially only because the detectors, whatever they are, have an enormous natural calorimeter attached to them — the Earth's atmosphere. Thus, this kind of observations deal with secondary particles and radiations from the cascades initiated by the cosmic rays hitting the atmosphere, which impedes the characterization of the cosmic ray.

The observation of the depth of air-shower maximum, or shortly X_{max} parameter, in the atmosphere is one of the prominent techniques to estimate the cosmic-ray nuclei composition. Air showers initiated by different nuclei exhibit their maximum at different

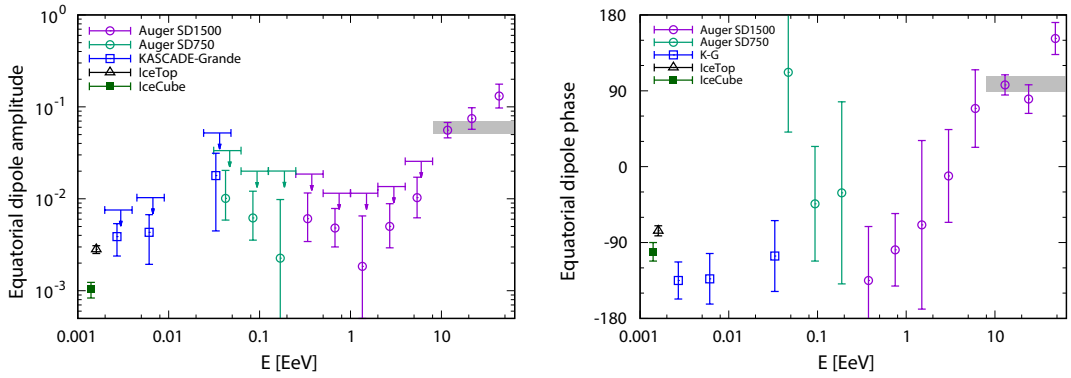

Figure 1.6: Plots summarizing the recent measurements of the large-scale anisotropy of the cosmic-ray incoming directions in the framework of the dipole model. The plots show the amplitude and the phase of the dipole. The plot is taken from [104].

depth in the atmosphere. However, due to shower-to-shower fluctuations, the $X_{\max}$ distributions corresponding to the individual nuclei are overlapping, which restricts measurements to the mean and the fluctuations of $X_{\max}$ at a given energy. Figure 1.5 shows a collection of recent measurements of the mean $X_{\max}$. Such measurements suffer from systematic uncertainties, which are likely not yet under full control. Due to this situation, the mass-composition remains uncertain since the data are inconclusive.

In some cases, deeper statistical analysis of the mass-composition data allows for deducing separate nuclei groups [22, 24, 103]. Such separation of the individual nuclei components provides an important insight into the astrophysics of the cosmic-ray acceleration and propagation, which, in turn, gives clues about the cosmic-ray origin.

1.4. ANISOTROPY OF THE INCOMING DIRECTIONS

The fact that cosmic rays are charged particles makes them affected by magnetic fields in intergalactic, interstellar, and interplanetary environments. Even though these magnetic field strengths are small relative to those we have in a laboratory on the Earth, the tremendous distances the cosmic rays travel through space make their motion highly perturbed by these magnetic fields. This makes finding the cosmic-ray sources by observation of their incoming directions challenging. Indeed, observations of the cosmic rays' incoming directions show that its distribution over the sky is fairly isotropic.

The degree of this isotropization depends on the cosmic-ray energy. The higher the energy, the less the isotropization effect. Observationally it appears as a slight but very significant anisotropy in the arrival-direction distribution pointing towards the possible cosmic-ray sources outside of the Galaxy. Recent high-exposure observations revealed the presence of this kind of anisotropy.

Figure 1.6 shows the results of the recent measurements of the anisotropy of the cosmic-ray incoming directions. In this figure the estimations of the anisotropy are performed using a dipole anisotropy model, a model with a region of deficit and excess of

the flux, which has only two parameters: the orientation of the dipole and its amplitude. These parameters are measured in the wide energy range from 1 PeV and higher. The orientation of the dipole indicates a transition of the cosmic-ray origin by turning around 1 EeV from the direction towards the Galactic center to the direction outside of the Galaxy. This recent discovery shows a clear spatial indication of the extra-galactic origin of the ultra-high-energy cosmic rays [105].

Reconstruction of the anisotropy in the observations is one of the important activities in cosmic-ray research nowadays.

1.5. PHOTONS AND NEUTRINOS

Photons and neutrinos are closely related to cosmic rays. In the acceleration sites and on the course of propagation, cosmic rays undergo interactions with magnetic and photon fields, hadron interactions, and decays. These processes lead to the creation of neutrinos and photons of various wavelengths from radio waves to high-energy gamma rays. Increased intensities of these messengers observed from some objects or regions usually indicate the presence of the cosmic rays. Moreover, photons and neutrinos are the only non-charged stable components of the Standard Model that can directly carry information from the sources bypassing the influence of the magnetic fields in space. In addition to this, measurements of the galactic and extra-galactic photon radiation provides information on the cosmic-ray propagation processes in those regions.

It is worthwhile mentioning a recent discovery of an ultraviolet arc in Ursa Major [106]. A new analysis of astrophysical-survey data in the ultraviolet range revealed a previously unknown large-scale structure in the sky in the constellation of Ursa Major, which is likely associated to a relatively old supernova. The further investigation of this new structure is ongoing. This discovery shows that even in our close proximity we can find new structures related to unknown old supernova, which can be potentially responsible for the local cosmic-ray composition. The recent discovery of ^{60}Fe, mentioned in Section 1.1.2 on the medium-energy cosmic rays may be related to this new shock-wave-like structure.

The origin of majority of the cosmic rays in the local interstellar medium is likely by processes related to supernovae as it was suggested a long time ago in [107]. However, for a long time it was not settled whether the bulk of the cosmic rays come from galactic or extra-galactic sources (Reference [108] discusses some historical aspects of this long-term problem). Measurement of the gamma-ray flux intensity from the Small Magellanic Clouds have resolved this problem. The cosmic rays propagating in that galaxy undergo nuclei interactions and generate neutral pions, which decay into high-energy photons. Since the gas density in those region is well known, the gamma-ray flux depends only on the cosmic-ray intensity. These measurements are carried on recently. The measurements reliably excluded the hypothesis of extra-galactic origin of the majority of the cosmic rays that we observe in the local galactic media. They show that the average cosmic-ray density in the Small Magellanic Cloud is approximately 15% of the cosmic-ray density measured locally in our Galaxy [109]. Such a large difference indicate that the bulk of

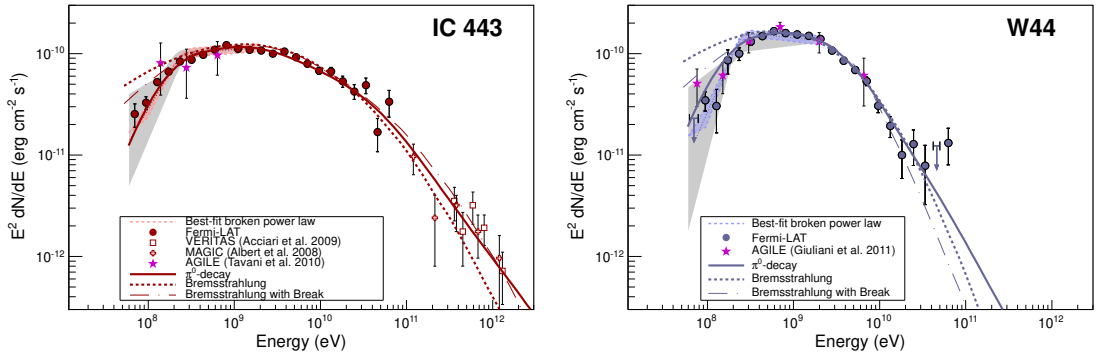

Figure 1.7: Energy spectra of two high-energy gamma-ray sources (IC 443 and W44). The precision of the spectrum allows for concluding that the shape of the spectra are caused by the neutral pion decay rather then the inverse Compton scattering. Presence of the pions indicate that these sources are cosmic-ray accelerators [111].

the cosmic rays originate inside of the galaxies itself rather than permeate into them from the outer space.

The gamma-ray flux can also be used to measure the cosmic ray flux within our Galaxy. Currently, efforts exist on exploiting the Giant Molecular Clouds in close proximity as targets for hadronic interactions to infer the parameters of the low-energy cosmic rays in those regions of the local Universe [110]. Since the density of the clouds are well known, the gamma rays originated from the decaying neutral pions from the interaction of cosmic rays and the neutral gas of the clouds carry information about the cosmic ray flux. It appears from the observations that the differential spectral index and absolute fluxes are similar to those in our Local Interstellar Medium.

The spectral density distribution of photons from astrophysical objects can provide comprehensive information about the acceleration processes happening in the object and in close proximity to it. This information is encoded in the shape of the distribution. The shape of the most energetic part of the photon spectrum is related to the acceleration mechanism of the most energetic primary cosmic rays.

Figure 1.7 shows results of recent measurements of the gamma-ray spectra from two supernovae remnants. The spectral shape reveals the first direct observation of the characteristic neutral pion decay in supernova remnants. This discovery indicates the correctness of the hypothesis that supernovae are high-energy accelerators of nuclei.

Recent observations of very-high-energy photons provided few new indications that some sources are capable to accelerate cosmic rays up to PeV energies. First, it was found that the center of our Galaxy radiates high-energy gamma rays beyond 100 TeV without evidence of a cut-off in the spectrum. Even though the particular processes in the Galactic center remain unknown, it is clear that the Galactic center is a potential candidate for PeV cosmic-ray sources [112]. Another discovery of the last years is the observation of the gamma-ray spectrum of the Crab Nebula up to the PeV energy range without a visible cut-off [113]. A similar situation is observed for a number of

other galactic sources [114]. This might indicate PeV-energy-range acceleration processes in this objects. Whether this process is hadronic or leptonic, however, remains unclear. Moreover, new insights in astrophysics of gamma-ray bursts are provided by the discovery of a gamma-ray emission from a nearby, bright GRB 180720B [115].

In context of the search for the cosmic-ray acceleration sources, the photon observations have limited capabilities. While propagating from the source to the Earth, the photons traversing the space photon fields can interact with them and create electron-positron pairs. This process forms a so-called horizon — photons of certain energy beyond that distance cannot reach the Earth. In the PeV energy range the horizon is slightly larger than the distance to the Galactic center.

Neutrino observation is another way to search for the objects or sites connected to cosmic-ray acceleration. In contrast to photons, the weak nature of neutrino interactions makes the Universe visible to vast distances. The recent progress in the neutrino detection resulted in the great discovery of the astrophysical neutrino flux. The origin of this flux is not fully understood yet. The number of observed astrophysical neutrinos is limited and they do not show any signs of significant clustering [116].

Recently, it was realized that combined observations of neutrinos and photons from the same direction can bring more comprehensive information on the possible sources of high- and ultra-high-energy cosmic rays and the processes happening in the sources. This approach combined with contemporary instruments, which are able to reconstruct parameters of the observed events with very small time lags, has recently led to the first observation of neutrinos from a flaring blazar TXS 0506+056 [117], which is an active galactic nuclei seen by the observer from the side of the jet. The observations showed that detection of high-energy neutrinos was correlated with photons of various wavelengths. Both messengers came from the same direction. This is an important indication to the hadronic processes happening in the source and, thus, to the cosmic-ray acceleration. Moreover, the analysis of the neutrino measurements from the direction of this blazar revealed a significant emission within several month of 2014–2015. Figure 1.8 shows a summary of this observation. This further supports the hypothesis that this blazar is a cosmic-ray accelerator. Another indication of a hadronic acceleration site comes from a recent observation of a correlation between neutrinos and photons for a tidal disruption event [118], a phenomenon of a gravitational disruption of a star approaching a black hole.

Another method was suggested recently for performing multi-messenger observations — use of a temporal and spatial correlation of observed high-energy neutrinos with multiwavelength activity of the active galactic nuclei. The method is new, however, already shows promising results [120, 121].

Even though the quest for the cosmic ray acceleration sites is far from conclusion, the observations of photons, especially in correlations with neutrinos, currently constitutes the most promising method that can shade light on this problem.

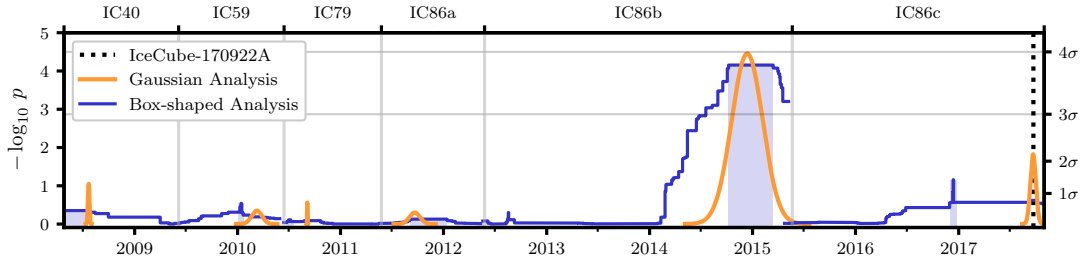

Figure 1.8: Neutrino emission from the direction of TXS 0506+056. The lines of two colors represents results for two time profiles (Gaussian and box-shaped widow analysis). The vertical dashed line indicates the time when the prominent high-energy neutrino was detected by IceCube, which initiated the multiwavelength follow-up observations. In the period of 2012–2015 a significant excess of neutrinos was detected. The plot is taken from [119].

1.6. DETECTION TECHNIQUES

Detection of cosmic rays is a diverse field. The main division is whether the instrument interacts with the cosmic ray itself or it detects secondary components of the interaction of the cosmic ray with the atmosphere. The former are direct techniques, the latter are indirect techniques. Since the focus of the present work lies on an indirect technique, this review will cover mainly them and the direct techniques are discussed only briefly.

1.6.1. Direct Detection

Even though the preferable way to detect the cosmic rays is outside of the Earth's atmosphere, the present capabilities of the aerospace technologies limit weight and volume of instrumentation, which can be placed in the space or sent to a balloon flight. Thus, space-born or balloon-born instruments usually provide a small exposure making them effective only for detection of relatively high fluxes of cosmic rays, which limits their use to energies up to few hundreds TeV [1].

The design of the detectors depends on the goals of a particular instrument. However, the direct instruments are nowadays usually designed with a calorimeter as a central detector allowing measurements of the cosmic ray energy. More advanced instruments can include a magnet and a particle tracker for measurements of the particle momentum and cosmic-ray charge estimation [122–124], or a dedicated charge measurement system. Also, they may use calorimeters of a special design, imaging calorimeters, measuring spacial distribution of the energy deposits [125, 126].

1.6.2. Indirect Detection

When entering the atmosphere, a cosmic ray initiates an extensive air shower, a cascade of particles and radiation. The indirect detection techniques are those which use these secondary particles and radiations for estimating the cosmic-ray properties [127]. The

following sections briefly discuss the features of widely used, selected techniques.

Particle detectors. Particles appearing in the cascade and reaching the ground level, muons, electrons, and photons can be detected by particle detectors. These are widely used in cosmic-ray research since its early days [3]. Contemporary versions of these detectors usually operate according to the following principles. First, detectors measuring the energy deposited by a particle in form of ionization. Scintillation detectors, one of the very widely used particle detectors these days [102, 128, 129], operate on this principle. While a charged particle passes through the sensitive material of the detector, it deposits energy by ionization of the material. Passing uncharged particles, like photons, interact with the material and either create a pair of an electron and positron or knock out an electron from the material. In both cases, the charged particle ionizes the material of the detector. The scintillation material of the detector converts the ionization charge into light, which in turn can be detected [130]. The amount of the detected light is proportional to the amount of ionization left by the passing particles. Another detector type operating in a similar manner and used nowadays are resistive plate chambers [131]. The only difference from the scintillation detectors is that these detectors measure the ionization electronically [132].

Second, detectors measuring the energy deposit by a particle in form of Cherenkov radiation [133]. The contemporary detectors of this kind use either water [134] or water ice [135] as detector media. The charged particles passing through the detector or generated inside the medium and traveling with sufficient velocity generate Cherenkov radiation, which provides a measure of the deposited energy [136].

Particle detectors are a very reliable technique that is able to reach full-time duty cycle [134]. However, this kind of detectors provide information only about the particles reaching the ground.

Cherenkov detectors and telescopes. The high-energy particles of extensive air shower have a relativistic velocity larger than the speed of light in air [127]. It leads to atmospheric Cherenkov radiation from the cascading charged particles [127, 133]. This radiation can be detected in two ways. The first way is to detect the Cherenkov radiation with wide-angle detectors. These detectors use a so-called non-imaging method, or timing method [137–139], providing the information about the arrival times and intensities of the Cherenkov light. Based on this information the properties of the air shower can be reconstructed. Another way to detect the Cherenkov light is to detect it with a telescope [140, 141], which essentially means to make a picture of the shower in Cherenkov light. The parameters of the image become the basis of the analysis of the air-shower properties.

Since the majority of the charged particles of the cascade are electrons and positrons [2, 127], the Cherenkov technique provides a measurement of the electromagnetic component of the air shower.

The main limitation of the instrumentation using this technique is that its duty cycle

is restricted to clear moonless nights. However, despite this fact, in the realm of high-energy ground-based gamma-ray astronomy the Cherenkov telescopes are the main observational instrument, due to their unprecedented power of identifying photon-initiated air showers on an intensive background of hadron-induced, cosmic-ray air showers.

Fluorescence light detection. While propagating through the atmosphere, an air shower excites molecules of air on its way [127]. This excitation results in an isotropic emission of fluorescence light with intensities proportional to the particle density in a given volume of air. The main contribution to this excitation comes from the electromagnetic part of the cascade. The resulting light can be detected with dedicated fluorescence telescopes [142]. This measurement provides the longitudinal shower profile, the particle density as function of the depth in the atmosphere, which is one of the best ways to measure the position of the depth of the shower maximum, $X_{\max}$ [143], and calorimetric energy of the air shower. Also, these measurements, similar to the Cherenkov-light measurements, can be done only during clear moonless nights.

Radio emission detection. The charged particles of the cascade constitute a macroscopic time-varying volumetric charge distribution rapidly moving through the atmosphere [144, 145]. This charge motion generate radio emission, which can be detected on the ground and provide information about the cosmic-ray and cascade properties. The main contribution to the radio signal comes from the electromagnetic part of the cascade, which makes the radio technique a good method to probe its properties. The details about the physics behind the radiation will be discussed in the next chapter.

In contrast to the previously mentioned techniques related to light detection, it is possible to detect radio emission from air showers round-the-clock and in almost all weather conditions [145].

1.7. OPEN QUESTIONS AND OUTLOOK

Cosmic rays are subject of research for a long time. Despite this, some important aspects of them are not yet fully understood. Two big, specific questions exist which remain unclear. The first one is the question, which appeared already in the early stages of research, about the origin of the cosmic rays [3, 146–148]. The second one appeared quite recently with detailed studies of the cosmic-ray air showers; and is the Muon Puzzle [149].

The current and near-future cosmic-ray air-shower observatories that also include radio detection as one of its channels should improve our knowledge about the mentioned questions. The following chapter describes some details about the radio emission coming from air shower and about tools used for estimation of their parameters.

CHAPTER TWO

RADIO EMISSION OF AIR SHOWERS

Air showers are cascades of relativistic particles moving through the Earth's atmosphere and magnetosphere. While moving, these particles have a complex dynamics, which, in turn, causes the generation of the radio emission that can be observed. In contrast to other air-shower detection techniques, the atmosphere does not disturb the propagation of the radio emission since it is transparent in the used frequency band [150]. The only effect occurring in the propagation of radio waves in the atmosphere is their slight delay, which is, however, not important for all questions discussed in the present work. This chapter reviews the main mechanisms of the radio emission and the main features of the produced radiation.

2.1. MAIN MECHANISMS CONTRIBUTING TO RADIO EMISSION

Propagation through the geomagnetic field and the atmosphere leads to several effects causing the spatial and temporal variation of the charged particle distribution in the air-shower front [151–153]. This rapidly moving variable charge distribution causes electromagnetic radiation in the radio band [154–156]. This radiation has few distinctive features. The radiation is coherent which means that some part of the air shower generating emission acts as a system of charges rather then individually contributing charges. The consequence of such coherence is the quadratic behavior of the yield of radio emission as a function of the cosmic ray energy. Another aspect is that the produced radiation is beamed forward towards the air-shower propagation direction. Together with the fact that the atmosphere is practically transparent for the radio emission, the beamed character of the emission means that the energy carried by the beam is conserved while it propagates through the atmosphere. The last but not least important aspect is that the air shower radio emission originates mainly from the electromagnetic part of the cascade. This aspect and the previously mentioned beam-like, absorptionless propagation through the atmosphere makes the radio emission an ideal tool for the absolute energy calibration and cross-calibration of the air-shower measurements.

Two main effects drive the variation of the charge causing the radiation: the geomagnetic effect [127, 157, 158], and the charge excess effect [159]. They gave the names of the corresponding radio emission mechanisms [144, 145, 151, 152, 159–161]. The following sections describe the physics behind these mechanisms and features of the radiation they produce.

2.1.1. Geomagnetic Mechanism

A particle with a charge q propagating with a velocity $\boldsymbol{v}$ through a magnetic field $\boldsymbol{B}$ is influenced by the Lorentz force, $\boldsymbol{F} = q\,(\boldsymbol{v} \times \boldsymbol{B})$, deflecting it from its straight motion. This phenomena is the key in the geomagnetic effect [151, 152][1]. Charged particles of an air shower moving through the geomagnetic field are influenced by the Lorentz force creating a time varying current within the shower front [144, 145]. This current is oriented perpendicularly to the geomagnetic field and in accordance with the classical electrodynamics generate electromagnetic radiation in the radio band [154]. The fact that the charges of the shower move faster than the speed of light in air causes a Cherenkov compression effect for the emitted radiation [162]. This emission of radio waves due to the geomagnetically induced currents in the shower front constitutes the "geomagnetic mechanism."

The orientation of the geomagnetically induced currents sets the polarization of the radio waves. Since they are oriented within the shower plane and turned perpendicularly to the geomagnetic field, while propagating with the shower front these currents induce a linearly polarized electromagnetic emission with the polarization vector aligned with the currents [154–156]. Another component of this effect also comes from the Lorentz force. The strength of the force has a strong dependence to the angle between the direction of the particle propagation and the direction of the geomagnetic field orientation. This can be easily seen if we rewrite the Lorentz force in the form $F = q\,|\boldsymbol{v}|\,|\boldsymbol{B}|\sin\alpha_g$, where α_g is the so-called "geomagnetic angle," which is very important for the discussion of the air-shower radio emission (see details in Section 2.2.1). Thus, the closer the shower comes from the direction of the geomagnetic field orientation, the weaker the radio emission caused by the geomagnetic effect.

The geomagnetic effect is the strongest within the traditional frequency band from 30 to 80 MHz [144, 145, 162]. Its main features, the strong dependence on the geomagnetic angle and linear polarization pattern across the footprint, form the main properties of the observable radio emission on the ground.

2.1.2. Charge Excess Mechanism

Another mechanism significant for the radio emission of air showers is the charge excess mechanism or the Askar'yan mechanism [159, 161]. The bulk of the air-shower particles are the electromagnetic particles: electrons, positrons, and photons [2, 78, 79, 127]. Their dynamics constitute the relevant effects for the radio emission.

While the air-shower front progresses through the atmosphere, the particles of the shower produce an equal number of electrons and positrons [2, 78, 79, 127]. Three processes change these numbers and contribute to the formation of a negative charge excess: annihilation of the positrons in flight, dragging of Compton and δ-electrons into

[1] It is interesting to note that the first article [159], which initiates the work on search for the air-shower radio emission [160], already mentioned the geomagnetic mechanism as a second possibility to give rise to coherent radio emission.

the shower. The interplay of all effects together builds up a negative charge excess in the shower front. This excess forms a time-varying [144, 145] charge asymmetry along the shower axis of the propagating shower front which initiates the radio emission. Since the shower charges move faster than the speed of light in air, the appearing emission undergoes the Cherenkov compression effect [162]. This emission has radial polarization pattern relative to the shower axis [163]. Recent detailed simulation studies showed that the charge excess fraction changes with variation of the air density at the position of $X_{\max}$ [164].

It is important to mention that in all processes happening in the air shower, including those mentioned in this section, the total charge remains conserved. This is a fundamental property of the quantum-field nature of our world [165–167].

The radiation coming from the charge excess mechanism is in most situations a minor contribution to the total radio emission from air showers, which is formed by the interference of the charge-excess emission and the geomagnetic emission described in the previous sections [144, 145]. However, the charge-excess mechanism contributes the most to the radio emission from particle cascades in dense media [144, 145].

2.1.3. Other Relevant Emission Mechanisms

The two radio emission mechanisms described above are certainly not the only possibilities to induce radio emission. As it is clear from classical electrodynamics, emission of electromagnetic waves always occurs when a charge or a current distribution accelerates or has oscillating multipole moments [154–156]. Moreover, changes of the electromagnetic properties of the media where charges or currents propagate induce a certain radiation as well [168]. Transition radiation is a particular example of the radiation occurring due to such changes. Despite the fact that mechanisms other than the geomagnetic and charge excess ones are certainly possible [169, 170], the observational evidences of their relevance for the air-shower radiation emission are not found to date [144, 145]. At least partially, this can be attributed to the present accuracy of the air-shower radio emission on the level of 10–15% of the absolute scale [144, 145].

2.2. MAIN FEATURES OF AIR-SHOWER RADIO EMISSION

The air-shower radio pulses appear as short, wide-band signals. Figure 2.1 shows an example of a measured air-shower radio pulse. The amplitudes of these signals have special features.

The two emission mechanisms described in the sections above and the relative size of the air-shower front to the radio wavelength form the main features of the air-shower radio emission. These features (the coherence, the polarization pattern, and axial asymmetry of the resulting footprint) are briefly described in the following sections. They are preceded with a brief introduction of the geomagnetic coordinate system — the main, physically motivated coordinate system used for the description of the air-shower radio emission.

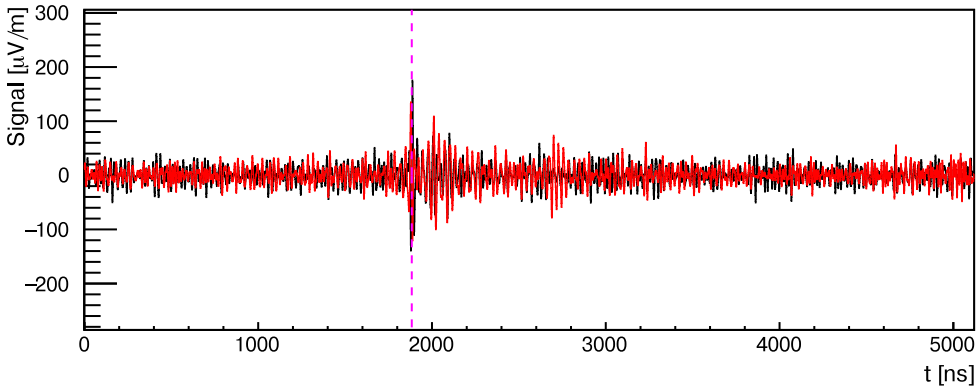

Figure 2.1: Radio signal measured by Tunka-Rex (antenna #14, event #855 observed on November 9th, 2012). The vertical line indicates the peak time of the reconstructed signal. The black line shows the electric field in the $\hat{\boldsymbol{V}} \times \hat{\boldsymbol{B}}$ axis, the red line shows the electric field in the $\hat{\boldsymbol{V}} \times \left(\hat{\boldsymbol{V}} \times \hat{\boldsymbol{B}}\right)$.

2.2.1. Geomagnetic Coordinate System

The air-shower radio emission is the result of the interference between the emission coming from the two mechanisms described above, the geomagnetic mechanism and the charge-excess mechanism. As it was mentioned, the emissions produced by these two mechanisms have specific polarization patterns for each of those mechanisms, the linear pattern for geomagnetic and the radial pattern for the charge-excess one. The interference of these two contributions form the observable air-shower radio emission on the ground. The difference in the interfering polarization patterns give rise to the asymmetric footprint of the radio emission observed on the ground. The geomagnetic effect provides the main contribution to the total magnitude of the radio-emission electric field. The emission coming from the charge excess of an air shower only modifies the main contribution. These considerations lead to the idea of introducing a special coordinate system for the description of the radio footprint, a coordinate system which follows the physics of the air-shower radio emission. This is the geomagnetic coordinate system. Thus, this coordinate system follows the principles of symmetry, where the geomagnetic emission has an axial symmetry and the charge-excess emission breaks it.

The geomagnetic coordinate system reflects the physics of the radio emission of air showers. The orientation of its axis goes as follows. The first axis follows the direction of the air-shower propagation, $\hat{\boldsymbol{V}}$. The second axis follows the direction of the Lorentz force, $\hat{\boldsymbol{V}} \times \hat{\boldsymbol{B}}$, which results from the cross product of the air shower direction of propagation and the direction of local geomagnetic field $\hat{\boldsymbol{B}}$. The third axis points perpendicular to those two axes in a way that that three axes form a right-handed coordinate system.

The mathematical form of the geomagnetic coordinate system is

$$\begin{aligned} \hat{\boldsymbol{e}}_x &= \hat{\boldsymbol{V}} \times \hat{\boldsymbol{B}}, \\ \hat{\boldsymbol{e}}_y &= \hat{\boldsymbol{V}} \times \left(\hat{\boldsymbol{V}} \times \hat{\boldsymbol{B}} \right), \\ \hat{\boldsymbol{e}}_z &= \hat{\boldsymbol{V}}. \end{aligned} \tag{2.1}$$

The hats above the vectors denote unit vectors. Additionally, two angles within this coordinate system are used for the radio footprint description: the "geomagnetic angle" $\alpha_g = \angle(\boldsymbol{V}, \boldsymbol{B})$, reflecting the angle relevant for the geomagnetic mechanism, and "geomagnetic azimuth" $\phi_g = \angle(\hat{\boldsymbol{e}}_x, \hat{\boldsymbol{e}}_y)$, a polar angle within the shower plane between vector $\hat{\boldsymbol{e}}_x$ and a vector within the shower plane.

2.2.2. Effects of Coherence

Radio emission of air showers might be the only air-shower phenomena where coherence effects appear in a clear way. Radio waves have macroscopic sizes, the waves corresponding to the middle of the traditional frequency band are six-meter long. This fulfills the prerequisites for coherent emission [162] since the scale of the air shower core is less than a meter and the scale of the air shower front, its thickness, is about a meter close to the shower axis region [127][2].

Let us consider the coherent effects in the framework of H. Allan's theory of air-shower radio emission [162, 172, 173]. In this theory the radio emission at a distance r is given by the integral

$$\mathcal{E} = \kappa \int_{h_0(r,\nu)}^{h_1(r,\nu)} \frac{N(h)}{h}\, dh. \tag{2.2}$$

The function $N(h)$ denotes the density of the particles at a given height h ($h = 0$ corresponds to the observation level), and ν denotes the observation frequency in MHz. The integration limits are solutions of the equation

$$\Delta t\left(r, h_c(\nu)\right) + \frac{1}{2\pi\nu} = \Delta t\left(r, h_{1,2}(\nu)\right), \tag{2.3}$$

where $\Delta t(r, h)$ is the time delay due to the Cherenkov effect. The integration limits essentially cut out the region of the shower, which is visible at a given lateral distance from the shower axis. The region within which we can observe the significant part of the air shower defines the coherence region. Figure 2.2 shows a particular example of the coherence limits.

The coherence of the radio emission leads to an important effect. The total power of the radio signal increases quadratically with the energy of the cosmic ray because of the coherent summation of the contributions from the individual particles of the cascade [174].

Another aspect which can be understood via the coherence of the radio emission is the size of the radio footprint. Figure 2.2 indicates which range of the distances

[2] The content of this section is inspired by [171].

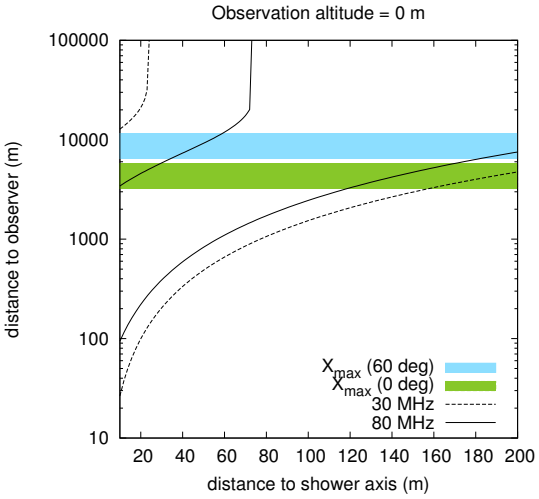

Figure 2.2: Coherence limits during air-shower development with respect to the observer. The color bands indicate the depth range from 500 to 700 g/cm^2 for vertical (in green) and inclined (in blue) air showers estimated with a corresponding atmospheric model. The radio emission is summed coherently within the marked bands. The bands correspond to the frequency range from 30 to 80 MHz. The picture is taken from Reference [171].

along the shower axis contribute to the emission coming to a particular lateral distance from the shower axis. It is visible, that starting from a certain distance the region of the coherent emission located close to the shower maximum starts to disappear or stops to contribute to the observed emission. For the particular example on the plot this distance is approximately 160 m for the vertical showers. This distance limits the observed footprint of the radio emission from the shower. This effect is an interplay of the position of the location of the coherence region in the air shower and the Cherenkov compression effect making different ranges of the distances contributing to different distances from the shower axis.

2.2.3. Polarization Pattern

The radio emission coming to a given spatial point on the shower plane has a slight elliptical polarization due to a small time delay between the arrival time of fields generated by the two emission mechanisms [175]. Besides that ellipticity, the polarization of the radio emission in its peak value has a particularly interesting behavior connected to the origin of the emission. The orientation of this polarization over the shower plane is the subject of this section, hereafter the corresponding vector field is referred to as polarization pattern.

The electromagnetic radiation coming from the geomagnetic and charge-excess mechanisms form an asymmetric footprint on the ground due to the interference of the polarization patterns specific for each of the two mechanisms. Since the geomagnetic radiation is dominant in the majority of the cases, its linearly polarized pattern shapes the radio footprint on the ground. The charge-excess radiation, with the radially polarized pattern and as a minor contribution, slightly modifies the radio footprint and makes it asymmetric. This behavior is generic except for shower directions within a few degrees from the geomagnetic field direction. It is independent of the strength of the radio emission. That is why it is interesting to look at this qualitative behavior in some details. This

section describes a simple model for the observations of the main effects resulting from the summation of the linear and radial polarization patterns.

Let us consider two vector fields in the geomagnetic coordinate system with the linear polarization

$$\begin{aligned} x_l &= L(r), \\ y_l &= 0, \end{aligned} \tag{2.4}$$

and with the radial polarization

$$\begin{aligned} x_r &= R(r)\cos\phi_g, \\ y_r &= R(r)\sin\phi_g. \end{aligned} \tag{2.5}$$

The functions $L(r)$ and $R(r)$ represent the radial profile of the linearly and radially polarized fields, which corresponds to radiation coming from the geomagnetic and charge excess mechanisms. The interference is the vector summation of the two fields

$$\begin{aligned} x &= L(r) + R(r)\cos\phi_g, \\ y &= R(r)\sin\phi_g. \end{aligned} \tag{2.6}$$

This resulting field shows the polarization pattern of the radio footprint of the air shower. The left plot in Figure 2.3 shows the pattern for the given particular profiles taken in the form to mimic the measured radio footprint shape

$$\begin{aligned} L(r) &= N_L\, G\left(\sigma_L\right), \\ R(r) &= N_R\, \left(G\left(\sigma_{R1}\right) - G\left(\sigma_{R2}\right)\right). \end{aligned} \tag{2.7}$$

The symbol $G(\sigma)$ denotes an unnormalized Gaussian function with a standard deviation σ centered at the origin. The constants N_L and N_R are corresponding amplitudes of the Gaussian functions. The values for N_L and σ_L set the strength of the geomagnetic emission and the width of the corresponding footprint. The values for N_R and σ_{R1} set the strength of the charge-excess emission and the overall width of the corresponding footprint. The value for σ_{R2} sets the width of the central region of the charge-excess footprint with a suppressed strength. This simple model reveals the overall linearly polarized pattern coming from the dominant, geomagnetic contribution with its only slight modification due to the charge-excess contribution.

We can take one more step and obtain the magnitude of the resulting vector field (2.6) by following the standard analytical technique

$$I = \sqrt{x^2 + y^2} = \sqrt{L^2(r) + R^2(r) + 2L(r)R(r)\cos\phi_g}. \tag{2.8}$$

This equation can be written for the square of the magnitude, which corresponds to the energy of the field and is deeply connected to the energy-fluence measurements, which have become a popular topic recently [174]. The rewritten form is

$$I^2 = \left(L^2(r) + R^2(r)\right) + 2L(r)R(r)\cos\phi_g. \tag{2.9}$$

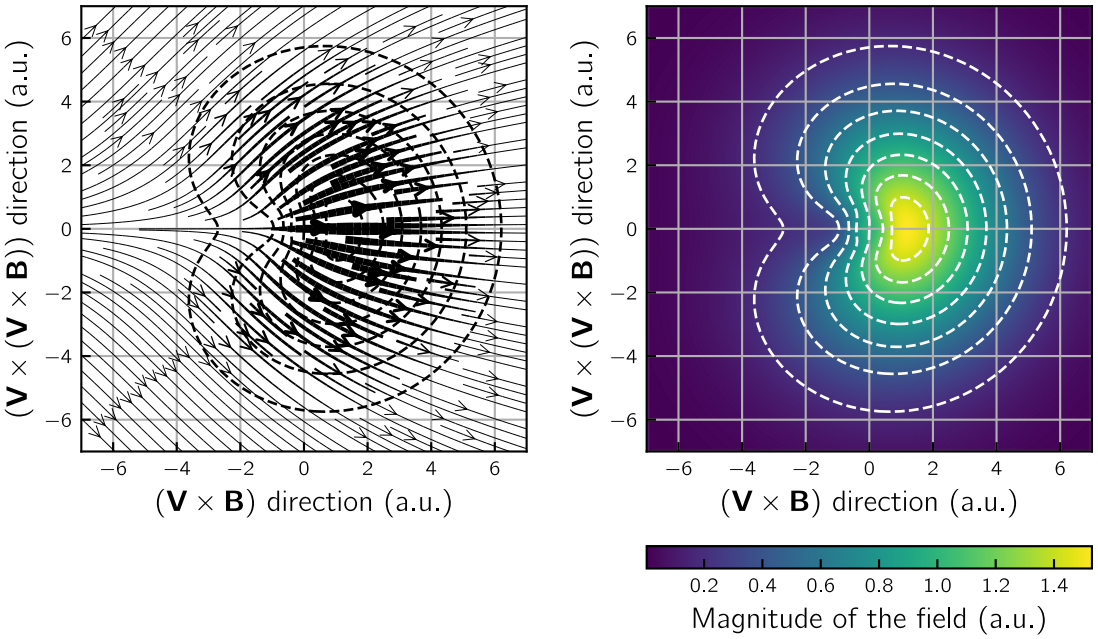

Figure 2.3: Features of the air-shower radio emission appearing in the simple model described in the text. The shower core is located in the origin. Both plots are shown in the geomagnetic coordinate system (see Section 2.2.1 for details). *Left*: Polarization pattern. The overall radiation remains mainly linearly polarized due to the dominance of the geomagnetic emission. The direction of the arrows shows the local orientation of the polarization of the radio emission. The thickness of the arrows shows the magnitude of the electric field vector of the radio emission. *Right*: The spatial distribution of the radio emission strength in term of the magnitude of the electric field vector over the shower plane. The axially asymmetric shape of the distribution is clearly visible.

It is noticeable that the equation has a certain structure. Namely, $a + b\cos\phi_g$. It is clear that this structure stays the same disregard the particular form of the profiles of the geomagnetic and charge-excess emissions as soon as they are centered in the same point, which appear to be the case from the measurements of air showers [164] because they are both centered around the shower axis. The term with the cosine is very important since it shows the asymmetry of the radio footprint in its generic form.

The right plot in Figure 2.3 shows the radiation strength pattern in terms of the magnitude of the electric field vector for the same profiles as for the polarization plot described above. It shows the apparent asymmetry of the footprint.

The profiles are selected for illustration purposes only, in a way that they mimic the observed, distinctive air-shower radio footprint characteristics. Thus, the shown profiles do not correspond to a shower with particular macroparameters, like energy, $X_{\max}$, etc.

The described approach has further practical implementations. One of those is the so-called GeoCE model of the lateral distribution function (the name GeoCE refers to the Geomagnetic and). This model uses exactly the same approach as described above,

but went further and connected the parameters of the radio footprint to the air-shower parameters [164].

Another important aspect of the simple model above is to show that the geomagnetic mechanism contributing the most sets the overall polarization pattern of the footprint which means that the polarization measurements can distinguish the dominant emission mechanisms. This became clear already in the early days of the research on the air-shower radio emission. Thus, already in that time, before any accurate quantitative model for estimating the strength of the radio emission, it was realized from the polarization measurements that the main contribution to the emission comes from the geomagnetic mechanism [176–181]. Recent measurements with newer instruments, digital radio arrays, confirmed this result [175, 182–185].

2.3. MODELS OF THE AIR-SHOWER RADIO EMISSION

The computation of the radio emission of air showers is a subject of classical electrodynamics. If the trajectories of the all particles are known, the problem of the radio emission consists of careful computation of all contributions in the Liénard-Wiechert potentials [186, 187]. It is clear that the straightforward approach to this computational problem is hampered by the large number of particles generated in the cascade and the complexity of their trajectories. There are two developed approaches to this problem: the macroscopic approach and the microscopic approach.

Models using the macroscopic approach exploit the known phenomenological properties of the collective motion of the charged particles within the shower front to simplify computations. The MGMR model [188, 189] is an example of such a model. To perform practical computations it uses a charge distribution from CONEX [190]. Analytical models of this kind were very popular in the early days of air-shower radio-emission research since very little computational resources were available in those times. However, these models paved the way towards our present knowledge about the radio emission mechanisms [162]. One of the most prominent work of this kind described the geomagnetic mechanism as the main contribution to the radio emission of the air shower [151]. The main works about the charge excess in air-showers and its possible contribution to the observable radio emission were also analytical. They described, in a very concise and physics clear manner, the second-major emission mechanism [151, 159, 161].

The macroscopic approach to the computation uses the Liénard-Wiechert potentials applied to individual particles of the cascade to estimate the final electric field in the observation point. Two formalisms exist following the microscopic approach: ZHS [186] and the end-point formalism [187]. It is important to note that these formalisms introduce no model assumptions and are only ways of discretizing the initial problem.

The ZHS model [186], implemented in the ZHAires software [191], uses the particle trajectories from the Aires software [100]. The end-point formalism, implemented in the CoREAS software, takes the trajectories from the CORSIKA software [99] to calculate the radio emission. In contrast to the macroscopic models the microscopic models provide

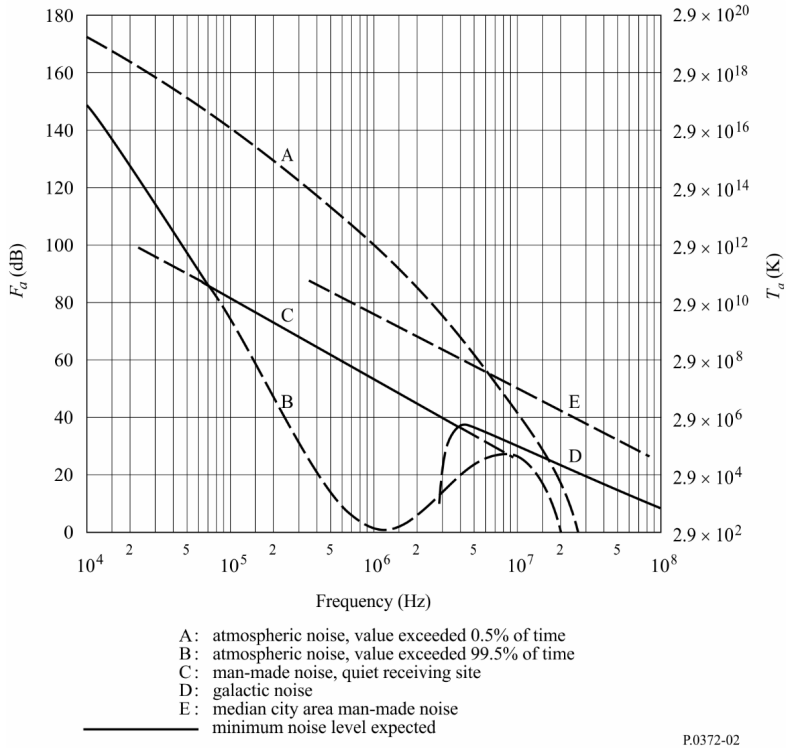

Figure 2.4: Power of radio noise over frequency with indication of individual contributions. The picture is taken from [194] together with the original legend.

highly accurate predictions of the radio emission for air showers with particular parameters and incoming directions. This approach to the electrodynamical computations is now the main tool in the reconstruction of the air-shower parameters from measurements and in further studies of the emission mechanisms. A detailed comparison of the models reveals the internal consistency of the present microscopic air-shower radio emission models [153, 192].

The CoREAS model was used throughout this work for all simulations of the air-shower radio emission. This model, including the corresponding software, is an in-house development of the Karlsruhe Institute of Technology which was one of the main reasons to use this model in this work. Moreover, it was shown that the model predictions match with measurements [193].

2.4. RADIO NOISE

Talking about measurements it is impossible to avoid matters related to backgrounds and noises. For the radio measurements, the noise, or broadly speaking, the nuisance radio emission can be of different kinds. It can be a quasi-steady-state noise with certain parameters, narrow-band interfering signals, and sporadic broad-band signals, known as radio frequency interference (RFI). Each of these components heavily influences radio measurements of faint air-shower radio signals.

The typical noises of the quasi-steady-state kind are the electronics thermal noise and the natural Galactic noise. While the level of thermal noise of the electronics is mostly a design issue, the galactic noise has a natural origin and is completely beyond our control. The galactic noise is always present in the measurements and interferes with them. However, the galactic noise is relatively well understood in terms of absolute values, which is the foundation of the current efforts to exploit it for the absolute energy scale calibration of the air-shower radio emission measurements [164, 195–197].

The noise of narrow band interfering signals can usually be easily removed from the radio spectrum of the signal, however, the sporadic wide-band signals or RFI impose a real issue for the measurements. These background radio pulses are vitally important for the present air-shower observatories measuring radio emission since no method exists to reliably identify and suppress such signals. Recent advances in application of the machine-leaning methods to the problem of signal denoising reveal a possible solution, however, these applications are only in a research phase and are not widely used by the cosmic-ray observatories [198, 199].

Figure 2.4 shows the spectra of different contributions to the steady-state radio noise at a typical observational site. It is apparent that different frequency bands have different main sources of the noise. In the band relevant for the present work, ranging from 30 to 80 MHz, the main source is the natural radio emission from the Galaxy. The man-made noise typical for city-center environments is usually not present at the remote sites of the cosmic-ray air-shower observatories.

2.5. OPEN QUESTIONS AND OUTLOOK

Despite the long way from the discovery to the utilization of the radio emission as a tool for measuring air-shower properties, there are still open questions. However, now they are more related to finer details. The first branch of open questions is related to remaining discrepancies between the macro- and microscopic models for computation of the radio emission, particularly MGMR and CoREAS. This discrepancy reveals our lack of knowledge about the emission mechanisms in a level of detail sufficient for pure macroscopic computations of the radio emission. The main region where this remaining effects exist is the near-shower-core region.

Another branch of open questions is related to, loosely speaking, effects of propagation. These kind of effects become more pronounced these days since the current and near-future radio instrumentation is intended to measure inclined showers and, sometimes, near-the-horizon showers [102, 200]. The column density of the atmosphere passed by an air shower becomes very large, making the radio emission coming from very large geometrical distances. This situation differs from the near-vertical observation of air showers. The main difference comes from the need to take into account the curvature of the atmosphere and from the presence of propagation effects in addition to the Cherenkov compression effect [201]. Understanding the physics behind these effects and the development of tools for taking them into account when reconstructing air-shower

parameters are subject for future studies. However, the main complication in studying such showers is related to complexity in simulations of their radio emission.

With the transition from analog to digital electronics, new instruments for the air-shower radio observation were developed in the past two decades. Their results of operation and developed analysis methods are vitally important for current and future air-shower radio arrays, which heavily rely on previous work.

The upcoming chapter describes one of the air-shower radio arrays, AERA, operating on the site of the Pierre Auger Observatory, which has the largest cosmic-ray detector complex in the world. The level of accuracy with which we understand the mechanisms of the radio emission enables utilizing the measurements of air-shower radio emission for absolute calibration of the entire observatory. The chapter presents results of a dedicated simulation study about such calibration.

CHAPTER THREE

CROSS-CHECKING THE ABSOLUTE ENERGY SCALE WITH AERA

Determining an accurate energy scale in cosmic ray observations is one of the central problems in contemporary astroparticle physics. A natural demand of accurate measurements is supported by the success of the latest generation of observatories, which have been measuring over the last decades the properties of cosmic rays in a wide energy region with a high statistical precision and low systematic uncertainties. The Pierre Auger Observatory holds a special place among all of them since it is the world's largest detector complex providing the most precise measurements of cosmic rays of the highest energies. The large amount of collected data enables high-precision studies of the astrophysical origins of cosmic rays and properties of high energies nuclear interactions via studies of air showers. The correct interpretation of the obtained results depends among others on the accuracy of the energy scale of the entire observatory. The present chapter describes results of a recent study on obtaining the absolute energy scale for the Pierre Auger Observatory via the measurements of the radio emission.

The chapter is organized in the following way. The introductory part reviews the instrumentation of the Pierre Auger Observatory. Then the concept of the absolute energy scale is described with the focus on the observatory. The final part presents the results of a simulation study of the energy scale as provided by the Auger Engineering Radio Array (AERA).

3.1. THE PIERRE AUGER OBSERVATORY

The Pierre Auger Observatory [202] operates one of the world's leading cosmic-ray detectors located on the high plain of the Pampa Amarilla at a altitude of about 1400 m a.s.l. close to the city of Malargüe in the province of Mendoza in Argentina. The detectors of the observatory are distributed over an area of about 3000 km^2 making it the largest air-shower observatory on the globe. The observatory is designed to effectively measure parameters of cosmic-ray air showers produced by nuclei with energies above 10^{17} eV and up to the highest energies.

The observatory has two main detector systems: the Surface Detector [134] and the Fluorescence Detector [142]. The two systems exploit different principles of air-shower detection that provides complimentary, hybrid information to the analysis. In addition to the two main detector systems, the observatory runs a low-energy extension [203–205] and a radio antenna array [205, 206]. Figure 3.1 shows the general map of the observatory.

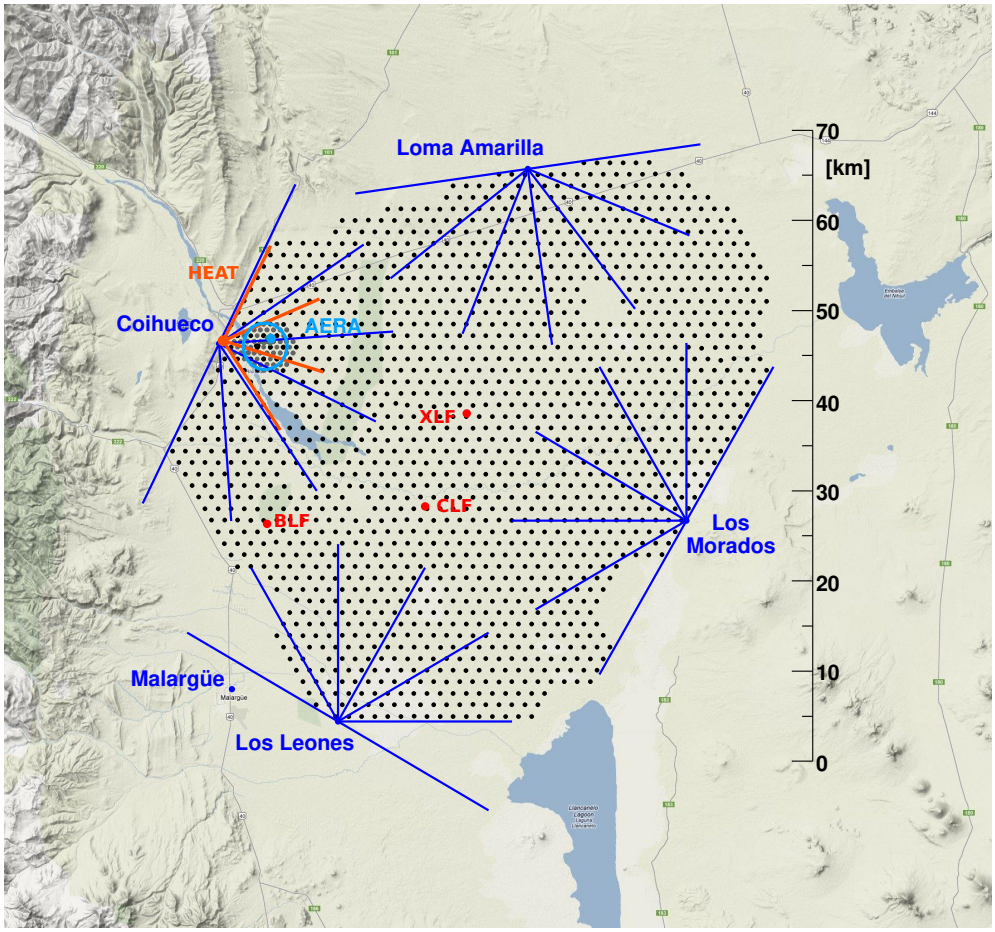

Figure 3.1: Map of the Pierre Auger Observatory and its facilities. The black dots show the location of the individual detectors of the Surface Detector array. The Fluorescence Detector overlooks the Surface Detector with the telescopes grouped in four sites: Los Morados, Loma Amarilla, Coihueco, Los Leones which are located around the array. The blue lines indicate the boarders of the fields of view of the individual telescopes at the sites. The region close to the Coihueco site hosts the low-energy extension comprised of a denser array of the Surface Detector stations with the muon detectors of AMIGA and the elevated fluorescence telescopes of HEAT (the red lines indicate the boarders of the corresponding fields of view). The same region hosts a radio extension (AERA). The red markers indicate the positions of the surface facilities of the observatory: the Central Laser Facility (CLF), the eXtreme Laser Facility (XLF), and the Balloon Launching Station (BLS). The laser facilities fire the test beams into the sky to calibrate the fluorescence telescopes. Balloons launched from BLS measure parameters of the atmosphere for calibration purposes. The entire observatory covers about 3000 km^2 and currently is the largest observatory on the globe.

Figure 3.2: Photo of a station of the Surface Detector. A communication antenna, a GPS module, and a solar panel are clearly identifiable on top of the station. One of the sites of the Fluorescence Detector is visible on the hill far away.

The following paragraphs review the components of the observatory on the level of detail relevant for the energy-scale analysis.

Surface Detector. The Surface Detector [134] is the main instrument of the observatory. The entire detector consists of about 1660 individual water-Cherenkov detector stations arranged in a triangular grid with spacing of about 1500 m covering about 3000 km^2. Each detector station is a water tank instrumented with three photomultipliers sensitive to the Cherenkov light produced by traversing charged particles. The tanks measure 3.6 m in diameter and 1.2 m in height. They are filled 1.2-m deep with purified water making 12 m^3 of sensitive volume. Figure 3.2 shows a photograph of one of the tanks. Each of the tanks is a standalone particle detecting device equipped with signal-detection and signal-processing electronics, solar power supply system, and wireless communication with the central control and data acquisition systems of the observatory. The detector design allows for 99% uptime. The detector provides mainly the estimation of the air-shower core position and incoming direction. The energy estimation is calibrated to the measurements of the Fluorescence Detector, which provides a more accurate energy estimation. The calibration reveals the energy resolution of 12% for high-energy air-showers. The resolution on the incoming direction reconstruction is 1.6° for events involving 3 stations and 0.9° for events involving more than 5 stations.

Fluorescence Detector. The volume of the atmosphere above the Surface Detector is observed by a system of 24 individual telescopes detecting the fluorescence light

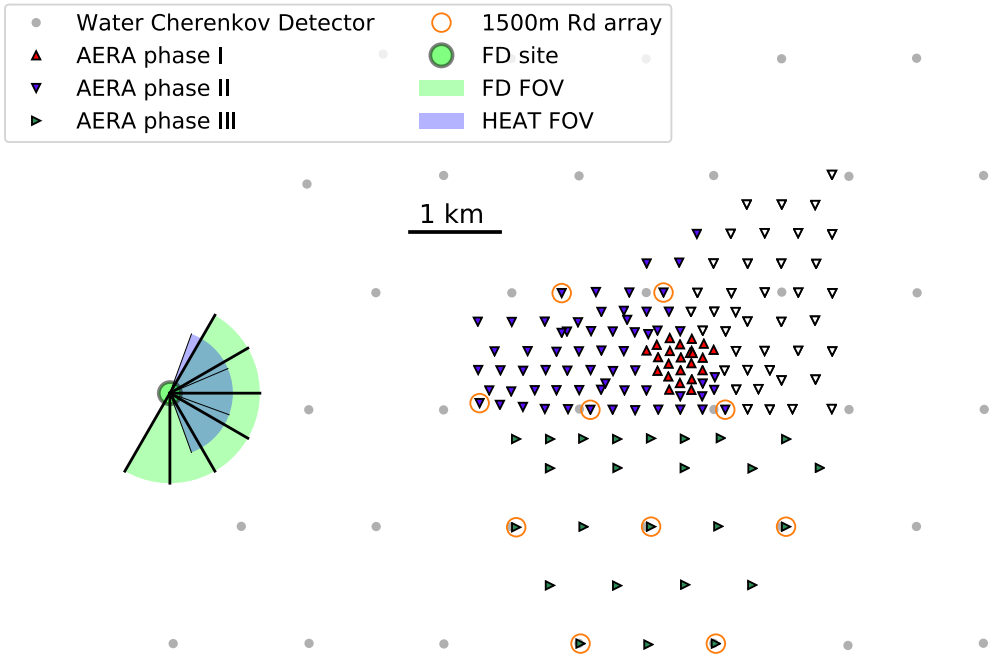

Figure 3.3: Map of AERA. The triangles with different orientation depict the layout of the three phases of the array. The empty triangles indicate the antenna stations do not receiving trigger from the Surface Detector array. The orange circles mark the AERA stations located at distances about 1500 m corresponding to the spacing of the Surface Detector array. The map is taken from [208].

appearing after a cosmic-ray air shower passed through the atmosphere exciting the atoms of nitrogen in it. This system is referred to as the Fluorescence Detector [142]. The telescopes of the system are grouped into four sites, each of which hosts six telescopes arranged side-by-side in a way that their individual fields of view of $30°\times30°$ form a larger, composite field of view ranging 180° horizontally. All the telescopes are elevated such that their fields of view are at least 1.5° above the horizon.

The optical systems of the telescopes follows the Schmidt design allowing for a wide field of view with a sufficient image quality. The basis of the optical system is a 10-m^2 tessellated spherical mirror and a corrector ring. In addition, the design is adapted for the purposes of the observatory by introducing a ultraviolet-light filter cutting out the ambient light of optical photons. Without this filtration it would be impossible to detect faint flashes of fluorescence light coming from air showers. Each telescope is equipped with a photomultiplier-based, 440-pixel camera. For the time being, the Fluorescence Detector is the main means of absolute energy calibration of the observatory. The telescopes provide an energy resolution of 7.4% for cosmic-ray air showers of 2.5×10^{18} eV and 8.6% for those of 6×10^{19} eV with accuracy of 14% [207].

Low-energy detector extensions. Two detectors the Auger Muon and Infill Ground Array (AMIGA) [203, 204] and the High Elevation Auger Telescopes (HEAT) [205]

extend the capabilities of the observatory to the region of lower energies and enables measurements of the cosmic-ray properties down to the energy region of the second knee. AMIGA is a denser instrumented region of the Surface Detector, additionally equipped with underground muon detectors. HEAT observes the atmosphere above this dense region. HEAT is a set of three fluorescence telescopes allowing for its elevation upwards up to 29°. This is crucial for observation of lower energy showers appearing higher in the atmosphere than the field of view of the regular fluorescence telescopes. Both instruments together extend the sensitivity of the Pierre Auger Observatory down to about 10^{17} eV, the region of the second knee in the cosmic-ray energy spectrum.

Radio extension. The Auger Engineering Radio Array (AERA) [205] is another extension widening the capabilities of the observatory to measurements of the radio emission accompanying air showers (Figure 3.3). The extension was developed to measure radio emission from air showers initiated by cosmic rays with energies from 10^{17}–10^{19} eV. AERA is an array consisting of 153 digital radio antennas distributed over an area of 17 km^2 making is the world's largest cosmic-ray radio instrument. Each antenna station is equipped with a solar-panel based power-supply system which enables the autonomous operation of the radio array. The AERA radio array evolved over several phases. It started in 2011 from an array of 24 log-periodic dipole array antennas distributed over the densely-instrumented region of the observatory with inter-antenna spacing of about 150 m. The next phase consisted of 100 antennas of the so-called Butterfly type. The antennas were deployed in a sparser grids: one group of 60 antennas was installed on a 250-m grid, another group of 40 antennas was installed on a 375-m grid. The last, third phase upgraded the 375-m grid with 7 additional antennas and deployed 18 antennas on a 750-m grid matching the spacing of the low-energy detector extension. The large variety of the inter-antenna distances and types of the antennas allowed for detail investigation of different trigger regimes and operation modes.

AugerPrime upgrade of the observatory. After about ten years of successful operation, the Pierre Auger Observatory is undergoing an upgrade [129]. Each of the detector stations of the Surface Detector is being upgraded with an additional scintillation detector and a radio antenna. Figure 3.4 shows the baseline design of the new detector station. Adding of the scintillation detection enables performing a better discrimination of the muon fraction in the observed air showers to improve mass-discrimination capabilities of the observatory. The radio antennas will provide reliable information about the electromagnetic component of air showers coming from the near-horizontal directions. Also, the radio antennas provide the potential to calibrate the absolute energy scale of the observatory in addition to the established fluorescence-light detection technique.

There are no doubts that the next ten years of operation of the Pierre Auger Observatory in its new upgraded configuration will bring more insights into the nature and origin of the most energetic particles in the Universe and in the details of the hadronic interactions at the highest energies. The estimation of the accurate energy scale for

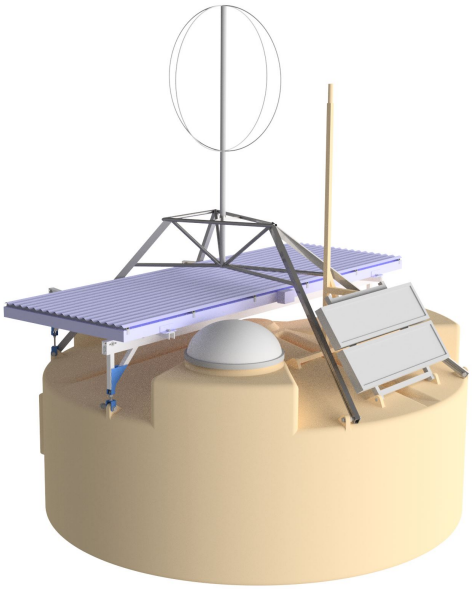

Figure 3.4: Design model of a Surface Detector station upgraded with a scintillation detector and a radio antenna. All the scintillation detectors will form the new Scintillator Surface Detector. The radio antennas which will be newly installed over the observatory will form the Radio Detector Upgrade. Both are part of the AugerPrime upgrade of the Pierre Auger Observatory. The picture is taken from [209].

the measurements is one of the central problems. Current efforts of the AERA group aim at developing methods which will allow for estimation of the absolute energy scale via the radio measurements. In the next sections we review the established technique for the energy scale calibration of the observatory and a new method which is under development by the AERA group.

3.2. ABSOLUTE ENERGY SCALE IN COSMIC-RAY OBSERVATIONS

The Pierre Auger Observatory, being the world's largest cosmic-ray detector, provides the statistically most precise measurements, which reveal subtle features of the cosmic-ray properties not visible before (see Chapter 3 in [129]). An accurate energy scale of these measurements is one of the foundations for a reliable interpretation of the data. Few methods of absolute calibration exist: measurements of the Cherenkov light, measurement of the fluorescence light [207], and measurement of the radio emission [164, 195–197]. The second method is the one established for the calibration of the absolute scale of the observatory, the later one is under development.

3.2.1. Fluorescence Light Measurements

Fluorescence light comes from the radiating nitrogen atoms excited by the fast moving particles of an air shower progressing through the atmosphere [127]. The amount of the light reflects the number of particles passing through the corresponding volume of the atmosphere. Since the main contribution to the excitation comes from the electromagnetic component, observations of excited air from a side give information about the particle density profile along the propagation of the air shower. The integration along the profile provides an estimation of the electromagnetic energy of the air shower.

Investigation of processes in the air shower accompanied with a dedicated analysis of

Table 3.1: Current systematic uncertainties of the energy scale of the Fluorescence Detector (FD). The range refers to the change from 3×10^{18} eV to the highest energies [207].

Factor	Value of uncertainty
Fluorescence yield	3.6%
Atmosphere	3.4%–6.2%
FD calibration	9.9%
FD profile reconstruction	6.5%–5.6%
Invisible energy	3%–1.5%
Energy scale stability	5%

the observations shows that it is possible to estimate the so-called invisible energy, a part of the cosmic-ray energy which goes to non-electromagnetic components of the air shower. By application of this analysis to the measurements, the fluorescence light detection become a reliable means of absolute energy calibration of the entire observatory [210].

Of course, measurements of faint fluorescence light in the absorbing atmosphere poses certain difficulties. The main of those is related to the characterization of the properties of the atmosphere with the best possible accuracy. For this purposes, the observatory uses several laser and lidar facilities monitoring the atmosphere over the entire duration of the observations and launches research balloons to measure the atmospheric profile. The current systematic uncertainties of the energy scale are summarized in Table 3.1.

Despite the great success in using the fluorescence light for the absolute energy scale calibration, this kind of measurements have obvious limitations coming from the fact that fluorescence light can be observed only during clear nights, but not all the time. Measurements of air-shower radio emission, another radiation coming from the electromagnetic component, does not have such internal limitations, and can potentially provide means of absolute energy scale calibration available almost all the time.

3.2.2. Radio Emission Measurements

The air-shower radio emission, as the fluorescence light measurements are, is mainly related to the electromagnetic component of the cascade. This electromagnetic origin combined with the transparency of the atmosphere for radio emission makes radio measurements a strong candidate to become another method for determination of the absolute energy scale of the Pierre Auger Observatory.

Early work of LOPES and Tunka-Rex. The first cosmic-ray observatories that used the radio emission to compare their energy scales were KASCADE-Grande [211] and Tunka-133 [138]. Their radio extensions, LOPES and Tunka-Rex [193] correspondingly, measured radio emission accompanying the detected cosmic-ray events. After the normalization of the recorded radio emission to the difference in altitude of the observatories and the local geomagnetic field, the amplitudes of radio signals corresponding

to cosmic-ray events with the same reconstructed energy reveals the difference in the absolute energy scale. This method applied for KASCADE-Grande and Tunka-133 gives the uncertainty of the energy scale on the level of about 10% because of the insufficient description of LOPES antenna characteristics [212].

Current efforts of the AERA group. In contrast to the comparison of the energy scales between different instruments in several locations, the AERA instrument aims at a much more challenging problem of obtaining the absolute energy scale of cosmic-ray measurements via the radio emission of air showers.

On the course towards this goal, the AERA group introduced few new ideas. The first of them is the idea to use not the amplitude of a radio pulse but its integrated power, called energy fluence. This quantity is closely related to the signal amplitude, however, it has a better connection to physics of air showers. The second idea introduced by AERA was to integrate this radio footprint for estimation of radiation energy released by air shower. Such an integration allows for exploiting the beam character of the radio emission leading to a conservation of the total energy within the beam while it propagates in the practically transparent atmosphere. This idea about exploiting the conserved air-shower radiation energy formed the foundation of the radiation energy analysis in AERA [213].

The goal of the analysis is to find the relation between the radiation energy E_{rad} released by an air shower and the electromagnetic energy E_{em} contained in it. The relation has the following form [213]

$$E_{\mathrm{rad}} = A \left(\frac{E_{\mathrm{em}}}{10^{18}\ \mathrm{eV}} \right)^{B} . \tag{3.1}$$

The letters A and B denote the calibration constants of the analysis. The constants A reflects the amount of electromagnetic energy emitted by an air shower with 10^{18} eV of the electromagnetic energy. The exponent B shows how this energy changes with the electromagnetic energy. Moreover, it holds the information about the coherent nature of the radio emission. Due to the coherent nature of the radio emission in the frequency band of 30–80 MHz, the radiation energy is expected to depend on the electromagnetic energy approximately quadratically ($B \approx 2$). However, some slight deviations are possible. Finding the proper calibration constants is the essence of the radiation energy analysis.

The simulation study performed in this work is complementary to [214], which is devoted to the study of the energy scale with the air-shower events observed by AERA. The simulations produced for the present study are based on the directional information and energy reconstructed for the observed events. Thus, the produced simulations match the observations. Moreover, the present study, for the first time, incorporates the complete model of the detector response making them the full-fledged, end-to-end simulations of the observed events. The following section summarize the details of the analysis.

3.3. ABSOLUTE ENERGY SCALE WITH SIMULATIONS

The present study is based on simulations prepared to match the events used in the previously mentioned analysis of the energy scale. The simulations were prepared to have the same geometry and energy as the corresponding reconstructed values for the observed events. Then the simulations were processed with the dedicated software incorporating the standard analysis used for the AERA data. Finally, the energy-scale calibration constants were fit to the obtained values of the radiation energy and the electromagnetic energy using several optimization procedures.

3.3.1. Summary of AERA Data Analysis

The analysis of the data observed by AERA is implemented within the `RdObserver` application of the Offline framework. The entire analysis consists of several steps each of which deals with a particular aspect of the event reconstruction. The following paragraphs briefly cover the steps relevant for the energy scale analysis.

Signal processing. This initial stage of the signal processing addresses the problems related to noise of different kinds and instrumentation effects. The initial step removes known interfering radio lines from the spectrum of the trace and limit the spectrum to the band of 30–80 MHz. Then the traces are upsampled and the antenna response is unfolded. The resulting traces are combined into one signal corresponding to the electric field measured by an individual antenna.

Signal reconstruction. The next step is to estimate the signal from an air shower in the trace. The estimation of the signal is performed in a dedicated signal-search window, a relatively narrow time interval of 100 ns width placed where the signal is expected to emerge. There are two definitions of what a signal is: the maximal amplitude of the envelope of the electric field or the time-integrated power of the electric field, or the energy fluence. AERA follows the second definition. The signal is the energy fluence of the electric field within the borders of the signal time window. The same procedure estimates the energy fluence of noise in a dedicated fixed noise time window. To suppress influence of noise to the signal, the corresponding energy fluence of the noise is subtracted from the signal.

LDF reconstruction. The signals obtained in the previous steps from all individual antennas located at various places of the shower plane sample the radio emission footprint from the air shower. Several LDFs can be fit to the samples to restore the full shape of the footprint. The current AERA analysis uses the so-called GeoCE LDF as the footprint model. The model has the same internal logic as those described in Chapter 2. The central idea behind both models is a summation of the two vector fields with polarization patterns corresponding to the geomagnetic and charge excess mechanisms. The AERA analysis estimates the total energy emitted by a shower as an integral of LDF.

3.3.2. Observation Dataset

The analysis described above was applied to a dataset of events measured by the Pierre Auger Observatory from June 2013 to December 2018. The details of the analysis of the data are described in [214]. From all the events which passed the reconstruction, the quasi-vertical events with zenith angles not exceeding 55° were selected for the present energy-scale analysis. In total, the dataset contains 856 observed events, which is the same events as used in [214].

3.3.3. Simulation Dataset

The reconstruction of the observed events mentioned above provides the input for the simulations prepared for this work. Two simulated events, hydrogen- and iron-induced are prepared corresponding to each of the measured events. Several steps are important for the present simulation set. The following paragraphs briefly summarize the necessary details. Table 3.2 gives an overview of the dataset parameters.

Table 3.2: List of the parameters used for the CORSIKA simulations.

Name of parameter	Set value
Cosmic-ray nuclei (`PRMPAR`)	H and Fe
Observation level (`OBSLEV`)	1570 m a.s.l.
High-energy hadron interaction model	QGSJetII-04
Low-energy hadron interaction model	URQMD 1.3cr
Energy cuts for hadrons, muons, electrons, and photons correspondingly (`ECUTS`)	0.3 GeV 50 MeV 250 keV 250 keV
Outer radius of NKG electron distribution (`RADNKG`)	5 km
Electron multiple scattering length factor (`STEPF`)	0.5
Using NKG and/or EGS4 (`ELMFLG`)	T T
Muon multiple scattering angle (`MUMULT`)	T
Magnetic field	according to WMM
Atmosphere model	GDAS, curved

`RdREASSimPreparatorNG` module for preparation of the CORSIKA simulation cards. Any CORSIKA simulation starts with preparation of an appropriate card. To prepare such cards, the AERA group uses a corresponding module within the Offline software. The module introduced in the observational-data analysis pipeline generates a card corresponding to the processed events with the reconstructed values of their core position, incoming direction, and estimated cosmic-ray energy. For the present study, this module was updated to allow for creating a few cards, one for each pre-selected nuclei, for each measured event.

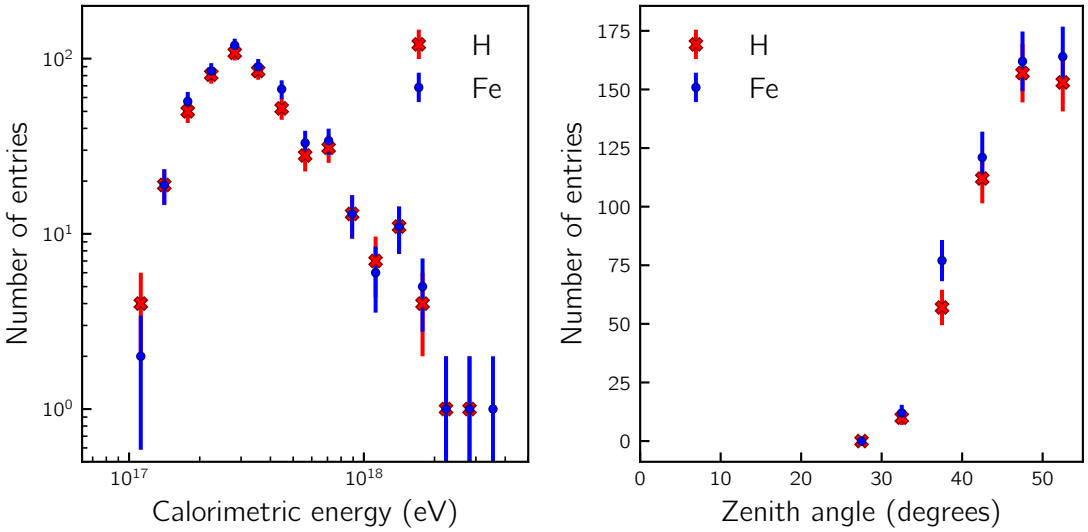

Figure 3.5: Distributions characterizing the simulation dataset. *Left*: the energy distribution. The shape of the distribution suggests that below 3×10^{17} eV AERA operates in a suppressed efficiency region. *Right*: the distribution of the zenith angles.

H- and Fe-induced showers for each event. Since the type of nucleus which initiated a given observed shower is not known, one proton- and one iron-induced shower are simulated corresponding to one observed event. Such a symmetry reduces potential biases in the reconstructed values of the calibration constants of the energy scale.

GDAS atmosphere for each event. One of the important components of the simulations is the correct model of the atmosphere. In addition to the U.S. standard and reference atmospheres, recent CORSIKA updates introduced a possibility to use the atmosphere profile based on measurements from the Global Data Assimilation System (GDAS). The system provides three-dimensional grid data based on the following types of measurements: surface observations, balloon data, wind profiler data, aircraft reports, buoy observations, radar observations, and satellite observations. A new utility program provided together with the updated CORSIKA code generates a model of the atmosphere from a set of GDAS data appropriate for a given date and location on the globe. The program fetches the data, interpolates them, and obtains coefficients for the five-layer atmosphere model used by CORSIKA. The resulted atmosphere description reflects our best possible knowledge about parameters of the atmosphere at a given place and point of time. The simulation dataset for this analysis uses this new functionality, i.e., the GDAS atmosphere of the time when AERA event was observed.

Step factor. Accounting for the multiple scattering of particles of the electromagnetic part of the air shower is important for its adequate description. CORSIKA uses the EGS4 model for the electromagnetic interactions. The model describes the multiple scattering in the framework of the Molière theory. The corresponding algorithmic implementation in EGS4 consists in adding an appropriate randomized scatter at discrete steps of particle

trajectory. The implementation allows the user to regulate the default settings for the scattering by tuning the step length with a corresponding parameter, called the step factor. The EGS4 model is tuned to the most reliable data on the electromagnetic interactions including experimental data on the multiple scattering. The default value of the step factor is 1.0, which corresponds to the best agreement with experimental data, however, the program implementation enables variation of this parameter by the end user. Tuning of this parameter regulates multiple scattering in the atmosphere effectively leading to switching it off for excessively small step lengths. A dedicated study showed that this regulation of the multiple scattering properties of the atmosphere causes changes in the yield of the radio emission from air shower [196]. The study revealed that reducing the value of the step factor at first increases the yield and then, after passing the maximum, starts to decrease it. The step factor value corresponding to the maximum is 0.05. Also, it is believed that the smaller step lengths better reproduce the actual physics of the multiple scattering in the atmosphere. Thus, based on these evidences the step factor of 0.05 was selected for the present simulation dataset.

Organization of the simulation process with SIMM. Usually, the simulation process is organized by special bash scripts and requires a mainly manual submission and control of the simulation process. Despite of the widespread use of this approach, a different approach was used for the present work. The SIMulation Manager (SIMM) software, which was initially developed for preparation of simulations for Tunka-Rex [193], was used to organize all steps required for the preparation of the simulation library: generation of the CORSIKA cards, running the programs for building the GDAS atmospheres, recording each of the simulations into a database, running the CORSIKA code with the prepared cards, and controlling its running process. To meet the requirement of the new task in AERA, which differs from the usual ones in Tunka-Rex, the code of SIMM was extended to enable for new capabilities. Using SIMM allowed preventing mistakes in multiple steps required for successful creation of a library and, in the end, simplified, and unified the simulation process.

3.3.4. Offline Reconstruction of the Simulation Dataset

To estimate the radiation energy for simulations in the same way as for the observational data, the dataset of simulations was reconstructed with the standard Offline application for analysis of simulations (`RdSimulationObserver`). The signal processing and event reconstruction steps implemented in this application are the same as in the application used for the observational data analysis described above (`RdObserver`), but with few additional preparation steps necessary to treat the simulated radio traces in the same way as the observational data.

Field to signal conversion. CoREAS simulations of the air-shower radio emission produce time series of electric field components. The initial step in the analysis of the simulations consists in bringing these to a realistic form. This means the conversion of

the incoming electric field to the signals observed by the antennas of AERA.

First, using a model of the antenna, the simulated electric fields are converted to the voltages observed with the channels of the antenna. Then, a model of the signal digitalization is used to simulate the analog-to-digital conversion of the signal. The result of the last conversion is the digitized signal trace, which mimics the data form obtained during the actual observations of air showers.

Finally, since the noise is an unavoidable factor in radio measurements, measured noise is added to the simulated traces to bring them to a realistic state. Starting from this point, the data analysis for these simulations and for the measured data are identical, i.e., end-to-end simulations are performed.

Offline processes the simulations on an event-by-event basis. After this stage, the results of the processing and reconstruction come to the next step performing statistical analysis of all events, which is implemented in a dedicated, independent piece of software.

3.3.5. Estimation of the Electromagnetic Energy

The energy scale connects an energy estimator to the energy of the cosmic ray in electronvolt. This work describes an energy scale connecting the electromagnetic energy of air shower and the energy which it radiated into the radio waves, radiation energy. As it was shown by the fluorescence-light technique for the energy scale calibration, the electromagnetic energy and the cosmic-ray energy are in close relation. Thus, hereafter the scale considered in this work is referred to as the energy scale.

Estimation of the electromagnetic and radiation energies comprises the initial stage of the whole analysis.

The electromagnetic energy in simulations can be estimated in two ways: as a sum of the histogram of the electromagnetic components in the longitudinal profile provided by CORSIKA or using the basic idea of the Auger analysis for estimation of the invisible energy in a data-driven approach [210]. The present work uses the second approach.

The central idea behind the data-driven estimation of the electromagnetic energy, E_{em}, consists in using the hadron extension of the Heitler air-shower model, the so-called Heitler-Matthews model of air shower [79]. Based on this model it is possible to reconstruct the fraction of the cosmic-ray energy, E_{CR} going to the invisible energy, E_{inv}. The relation between all these energies is formulated in the following form

$$E_{\mathrm{CR}} = E_{\mathrm{em}} + E_{\mathrm{inv}} = E_{\mathrm{em}} + \alpha_{\mathrm{inv}} \left(\frac{E_{\mathrm{em}}}{10^{18}\ \mathrm{eV}} \right)^{\beta_{\mathrm{inv}}} . \tag{3.2}$$

This relation is used in the present analysis to estimate the electromagnetic energy from the known cosmic-ray energy. The calibration constants of the relation equal $\alpha_{\mathrm{inv}} = 0.160$ EeV and $\beta_{\mathrm{inv}} = 0.952$. Since the equation is implicit for the electromagnetic energy, a residual minimization is used to find it. The residual of (3.2) is simply

$$R(E_{\mathrm{em}}|E_{\mathrm{CR}}, \alpha_{\mathrm{inv}}, \beta_{\mathrm{inv}}) = E_{\mathrm{CR}} - E_{\mathrm{em}} - \alpha_{\mathrm{inv}} \left(\frac{E_{\mathrm{em}}}{10^{18}\ \mathrm{eV}} \right)^{\beta_{\mathrm{inv}}} . \tag{3.3}$$

The value of $E_{\rm em}$ corresponding to the zero value of the residual is the result of the numerical inversion. To simplify the entire procedure, we consider squares of the residuals, but not the residuals themself. This allows for using simple function minimization algorithms since the squared residuals have a minimum at the proper value of the electromagnetic energy. Thus, formally, the inversion procedure has the following mathematical form

$$E_{\rm em} = \arg\min_{E_{\rm em}} \left(E_{\rm CR} - E_{\rm em} - \alpha_{\rm inv} \left(\frac{E_{\rm em}}{10^{18}\ {\rm eV}} \right)^{\beta_{\rm inv}} \right)^2 . \tag{3.4}$$

In contrast to the summation of histograms of the electromagnetic components of a shower, the described procedure provides an estimation that is conceptually closer to the procedures used for the observational data analysis.

3.3.6. Estimation of the Radiation Energy

The second major component of the energy scale analysis is the radiation energy, the part of the cosmic-ray energy going into the radio emission.

Let us review some details of the energy fluence measurement technique developed in [164]. The basis of the energy fluence technique lies on the vector summation of the contributions from the charge-excess emission and the geomagnetic emission received in phase at the detector level (for details about the vector summation and the physics behind see Chapter 2). The properties of the total radio emission can be described as a combination of the properties of the two individual emission mechanisms, which are both originating mainly from the electromagnetic part of the air shower.

The observed radiation energy, $E_{\rm rad}$, is connected to the energy content of the electromagnetic part of air shower via the so-called corrected radiation energy, $S_{\rm RD}$ which is estimated via the observed radiation energy

$$S_{\rm RD} = \frac{E_{\rm rad}}{a^2(\rho_{X_{\rm max}}) + (1 - a^2(\rho_{X_{\rm max}}))\sin^2\alpha}. \tag{3.5}$$

The denominator is the correction factor due to the known behavior of the emission from the two mechanisms. The radiation from the geomagnetic mechanism scales with $\sin^2\alpha$ (in power units), where α is the geomagnetic angle (see Chapter 2 for details). The function $a(\rho_{X_{\rm max}})$ is a parametrization of the charge excess fraction in the total emission depending on the atmospheric density at the $X_{\rm max}$ height.

The corrected radiation energy is linked to the air-shower electromagnetic energy, $E_{\rm em}$, via a power law

$$S_{\rm RD} = A \left(\frac{E_{\rm em}}{10^{18}\ {\rm eV}} \right)^B . \tag{3.6}$$

The second leading correction to the radiation energy are due to further effects of the air density at the position of the depth of shower maximum. With this additional factor, the corrected radiation energy has the following form

$$S^{\rho}_{\rm RD} = \frac{E_{\rm rad}}{a^2(\rho_{X_{\rm max}}) + (1 - a^2(\rho_{X_{\rm max}}))\sin^2\alpha} \frac{1}{(1 - p_0 + p_0 \exp[p_1(\rho_{X_{\rm max}} - \langle\rho\rangle)])^2}. \tag{3.7}$$

The symbol $\langle\rho\rangle$ denotes the normalization density of 0.65 kg/m^2.

Air showers of ultra-high energies are large and penetrate the atmosphere very deeply. Sometimes this causes a so called clipping effect, the situation when the cascade arrives at the instrument not fully developed and the cascade curve becomes truncated, or clipped. For radio detection this means that the emission generated by such a partial cascade will carry only partial energy fluence. To take this effect into account and correct for it, the following parametrization is used to restore the fully radiated energy, $E_{\rm rad}$, from the observed one with a given distance to the shower maximum expressed in terms of kg/cm^2, $D_{X_{\rm max}}$ [164]

$$E_{\rm rad} = \frac{E_{\rm rad}^{\rm obs}}{1 - \exp\left(a_{\rm c}\left(D_{X_{\rm max}} + b_{\rm c}\right)^{c_{\rm c}}\right)}. \tag{3.8}$$

The constants $a_{\rm c}$, $b_{\rm c}$, and $c_{\rm c}$ are obtained from the simulation study [164].

3.3.7. Estimation of Calibration Constants

The values of the electromagnetic and radiation energy estimated with the methods described above for each of the simulated hydrogen- and iron-induced showers form the dataset for the energy scale estimation, the essence of which is finding the calibration constants A and B of (3.6). Few methods have been used to estimate these constants: the least square method [215] and the negative logarithmic likelihood method [215] with the minimal gradient optimization [216] or with the Markov chain Monte Carlo sampler [217, 218]. While the least square method is straightforward, the negative logarithmic likelihood method requires some explanations.

The likelihood is based on a Gaussian distribution. Since it is likely that uncertainties of the radiation energy are not exactly known, the variance of the distribution contains a nuisance parameter to account for it. In general, under- and overestimation of the uncertainties are possible. The nuisance parameter can indicate both cases. In case of underestimation, it shows a non-zero value; in case of the overestimation, it equals zero. Introduction of a nuisance parameter is preferable due to the fact that the parameter estimation can be biased in case of wrong estimation of uncertainties. Thus, the likelihood has the following form [217, 218]

$$\ln p(S_{\rm RD}|E_{\rm em},\sigma,A,B,f) = -\frac{1}{2}\sum_n \left(\frac{\left(S_{{\rm RD}\,n} - S_{\rm RD}\left(E_{{\rm em}\ n}|A,B\right)\right)^2}{s_n^2} + \ln(2\pi s_n^2)\right). \tag{3.9}$$

The symbols $S_{{\rm RD}\,n}$ and $E_{{\rm em}\,n}$ denote the corrected radiation energy and the electromagnetic energy for each simulation. The function $S_{\rm RD}\left(E_{{\rm em}\,n}|A,B\right)$ is a particular value of the radiation energy for a given energy $E_{{\rm em}\,n}$, for the parameters A and B under evaluation. The variance s_n^2 holds information about the uncertainty of $S_{{\rm RD}\,n}$, σ_n, and the value of the nuisance parameter f in the following form

$$s_n^2 = \sigma_n^2 + f^2 S_{\rm RD}^2\left(E_{{\rm em}\ n}|A,B\right). \tag{3.10}$$

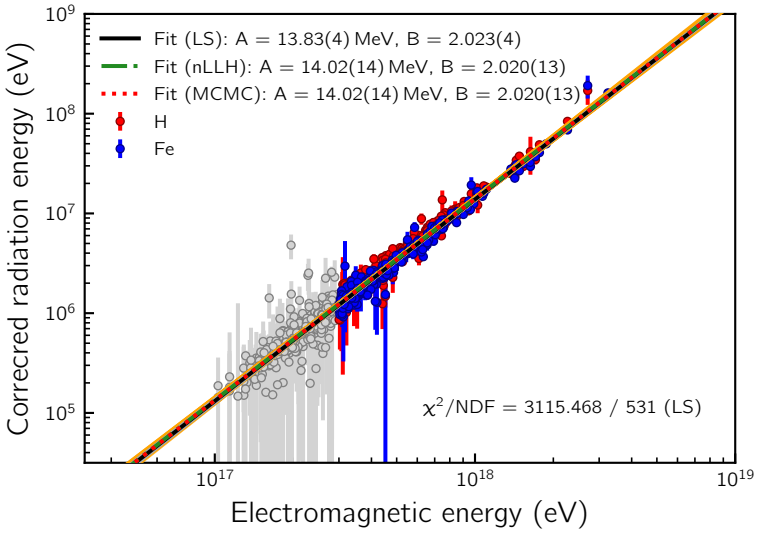

Figure 3.6: Energy calibration obtained with the simulation data. The blue and red data points are proton and iron simulations. The gray data are those which are in the non-full-efficiency region, and are not used in the evaluation. The lines of different types represent the fits done with the three different methods: the least-square method (LS), the negative logarithmic likelihood method with the minimal gradient optimization (nLLH) and with the Markov chain Monte Carlo sampling optimization (MCMC). The orange band shows the uncertainty of the model estimated with a bootstrap method.

Such parametrization implies that the additional contribution to the uncertainty scales with the value of the function, which is the standard practice [217, 218].

Figure 3.6 reveals the optimization results. To mitigate a possible bias from using the events from the non-full-efficiency region, the events below $3{\times}10^{17}$ eV are excluded from consideration. Table 3.3 summarizes the parameters obtained by all three methods.

Table 3.3: The summary of energy-scale calibration constants evaluation. The abbreviations are the same as used in the caption to Figure 3.6.

Method	A (MeV)	B	$\ln f$
LS	13.83(4)	2.022(4)	—
nLLH	14.02(14)	2.020(13)	$-2.211(43)$
MCMC	14.02(14)	2.020(13)	$-2.208^{+0.043}_{-0.042}$

The estimations obtained with the negative logarithmic likelihood method uses both methods of optimization are compatible within the uncertainties. The least-square estimation shows a slight offset, which is expected because of the possible underestimation of the data uncertainties. The nuisance parameter f indicates that indeed the underestimation of an uncertainty is present in the data.

3.4. COMPARISON WITH OTHER RESULTS

The values of the calibration constants obtained in this work and in [214] are close (see Table 3.4 for a summary). The fact that the present work uses the simulations matching the observations in [214] and an identical reconstruction procedure indicates that a preliminary comparison can be done, however, further investigations are required to draw the final conclusions.

Table 3.4: Comparison of the calibration constants for the free optimization procedure and with fixing B to the value found in the analysis of basic simulations. The values for the observations are from [214].

	A (MeV)	B
Full-fledged simulations (MCMC)	14.02(14)	2.020(13)
Full-fledged simulations (MCMC + fixed B)	13.61(8)	1.975 (fixed)
Observations	12.4(7)	1.922(42)
Observations (fixed B)	13.3(7)	1.975 (fixed)

Reference [214] also gives a value for A in case the exponent B is fixed to the value found for the basic simulations [213], $B = 1.975$. A corresponding value was found for the simulations as well (see Table 3.4). It can be easily appreciated how close the values of A for both of these cases, observations and simulations. For this particular case, the relative difference becomes smaller than 10% indicating a relatively good agreement.

Despite the fact that the calibration constants obtained with the full-fledged, end-to-end simulations are in a relatively good agreement to those obtained for the AERA observations, the work on the energy-scale analysis is ongoing and far from final conclusions. A good overview of the challenges emerging in the data analysis and signal processing related to the absolute energy scale can be found in [214, 219].

3.5. CONCLUDING REMARKS

Measurement of the radio emission constitutes a very promising technique for the calibration of the absolute energy scale in cosmic-ray observatories around the globe. The main advantages of this technique in comparison to the measurement of the Cherenkov or fluorescence light are linked to its physics and features of propagation. The radio emission originates mainly from the electromagnetic part of the air shower, which is similar to the two other techniques and allows for using already existing experience on the calibration of the absolute energy scale [210]. Also, while generated, the radio emission propagates through the atmosphere without practically relevant absorption. This absorptionless propagation enables using the full energy contained in the diverging beam of radio emission coming from an air shower as energy estimator disregarding the altitude of a particular observatory. Moreover, the detection of the air-shower radio

emission does not suffer from many limiting factors. The observations are routinely possible around the clock.

All these aspects of physics of air-shower radio emission show the importance of the ongoing work within the Pierre Auger Observatory on the absolute energy scale calibration using the radio emission. The presented analysis is relevant to a large effort on establishing the radio technique as the second method for the absolute energy scale calibration of the observatory after the measurements of the fluorescence light. The presented analysis with the full-fledged simulations reveals a good agreement between the calibration constants obtained for these simulations and for the observational data. Such agreement suggests that the work on the energy scale analysis approaches the stage when the direct comparison between the simulations and observations will be possible.

CHAPTER FOUR

TUNKA RADIO EXTENSION (TUNKA-REX)

The Tunka Radio extension (Tunka-Rex) is a digital radio antenna array designed to measure the radio emission of cosmic-ray air showers. Tunka-Rex is one of the first digital antenna arrays that demonstrated the reconstruction of the parameters of air showers, such as energy and $X_{\max}$, with such a sparse array with a precision on the level of the state-of-the-art optical measurements [220]. This chapter describes the Tunka-Rex array hardware and features of the standard Tunka-Rex data analysis.

4.1. SITE OF THE TUNKA-REX ARRAY

The Tunka-Rex array is located in the Northern hemisphere, in the Tunka Valley, close to the southern tip of Lake Baikal in East Siberia, Russia. The geographical coordinates of the site are 51° 48' 35" N, 103° 4' 2" E. The site elevation is 675 m above sea level, which corresponds to the atmospheric depth of 955 g/cm^2 (vertical depth from the top of the atmosphere to the site elevation).

One of the most important geophysical characteristics for the detection of air-shower radio emission is the strength of the geomagnetic field and its orientation. Figure 4.1 shows a global map of the geomagnetic field magnitude according to the World Magnetic Field model of 2015 [221] together with the locations of cosmic-ray radio instruments.

The strength of the geomagnetic field at the Tunka-Rex location is 60.32 µT (the horizontal component is 57.29 µT pointing towards North, the vertical component is 18.88 µT pointing downwards, the vector of the geomagnetic field points downwards at 18° from the nadir) [221] making it the air-shower radio array with the highest local geomagnetic field strength in the world to date. This means that an air shower with a given energy emits a stronger electromagnetic field than in other locations. Thus, in turn, Tunka-Rex can have a lower energy threshold for cosmic-ray air-shower detection than other instruments with similar operation frequency.

4.2. ASTROPHYSICAL INSTRUMENTATION ON THE SITE

The Tunka astrophysical site hosts many instruments observing both cosmic and gamma rays. All instruments are located at the same area (Figure 4.2) making it a unique site for ground-based astroparticle physics measurements.

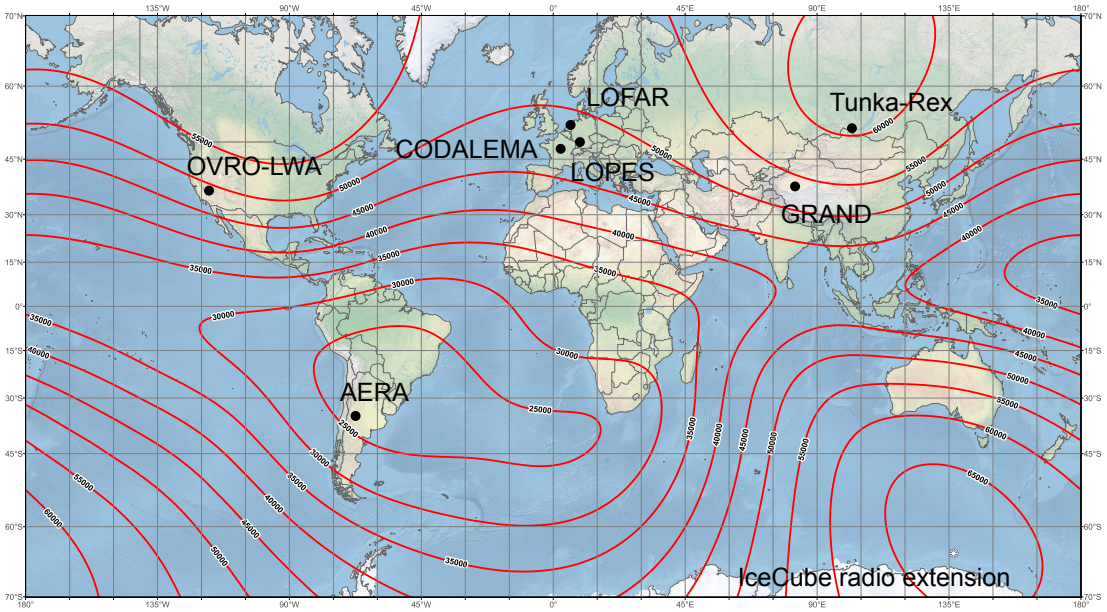

Figure 4.1: Map of the strength of the geomagnetic field according to the World Magnetic Field model for 2015 [221], a time, which is relevant for the Tunka-Rex array operation period. Additionally, the map shows the locations of Tunka-Rex and modern air-shower radio arrays: LOPES [222], AERA [205], the radio extension of the IceCube surface array [223], GRAND [224] (the final location is not determined yet), and CODALEMA [225]; and astronomical radio arrays measuring cosmic-ray radio emission: LOFAR [226] and OVRO-LWA [227].

4.2.1. Tunka-133

The oldest instrument at the site is the Tunka-133 array as successor of Tunka-25 [228, 229]. Tunka-133 is an array detecting Cherenkov light produced by the cosmic-ray air showers in the atmosphere. The array detects the spatial and temporal distribution of the light at the ground level, which makes Tunka-133 a so-called timing array [25].

Two parts comprise the general instrument layout: the denser core part and the satellite clusters. The core part consists of 133 optical detector modules giving the name to the instrument. The modules in the core part and in the satellite part are grouped in clusters of seven modules. Each of the clusters operates as an individual sub-array during the operation of the full array. If more than a given number of the optical modules have a signal, the information from the cluster is transferred to the central data-acquisition system of the instrument. Further, on the level of the post-observational analysis, data-analysis algorithms combine the information from all clusters into events, associated with showers [25, 230].

The Tunka-133 module design is shaped around the major component, a large-sized photomultiplier tube detecting the Cherenkov light coming from air showers. A flat plexiglas window covers the tube from the atmospheric precipitations and harsh

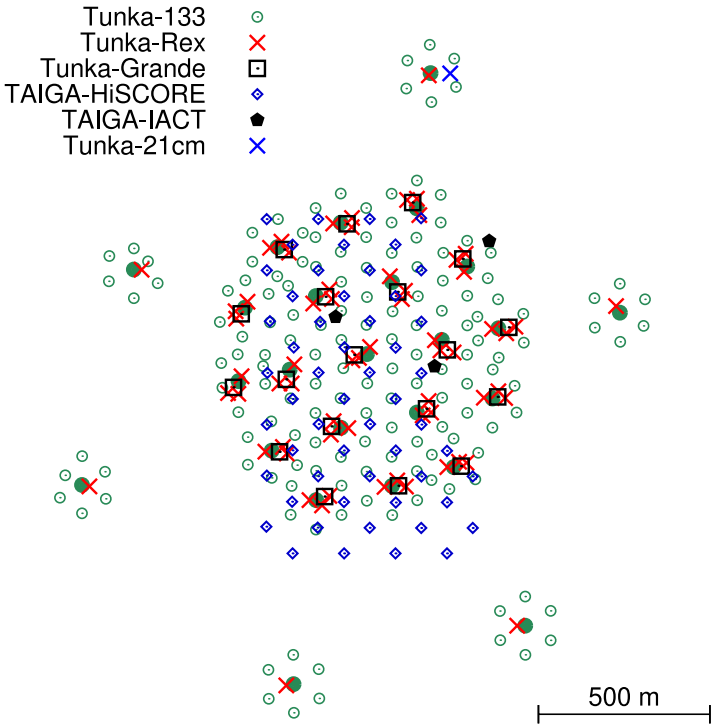

Figure 4.2: Layout of the Cherenkov-light timing array Tunka-133 and its radio extension Tunka-Rex along with other TAIGA instrumentation in 2019 (before decommission of Tunka-Rex): the scintillation detector array Tunka-Grande, the low-energy Cherenkov-light timing array TAIGA-HiSCORE, the TAIGA imaging atmospheric Cherenkov telescopes (TAIGA-IACT), and the Tunka-21cm research and development cluster for paving the path towards the detection of the 21 cm cosmological hydrogen line.

environmental conditions. To avoid freezing of the covering, it is equipped with a heating system formed of heating wires beneath the window. A cylindrical, metal case houses all components. The case has a remotely controlled lid to protect the window from a snow accumulation and avoid direct Sun light shining at the photomultiplier tube during days.

The first cluster of the future Tunka-133 array began cosmic-ray observations in 2005 [231]. In its full configuration, the array started observations in 2008. Over the years, the instrument accumulated cosmic-ray events and gradually increased the precision of the energy spectrum and the depth of shower maximum measurements in the energy range from about 10 PeV to about 1 EeV. The array keeps operating until now, however, the data analysis reaches currently only till 2017. Reference [25] summarizes the main results of the cosmic-ray observations with Tunka-133.

4.2.2. Tunka-Grande

The Tunka-Grande instrument is designed to detect air-shower particles at ground using the technique of scintillation detectors separated with an absorber layer.

The Tunka-Grande layout matches the general layout of the Tunka-133 clusters in the central, dense region. The data-acquisition systems of Tunka-133 and Tunka-Grande communicate with each other. During nights, Tunka-133 triggers Tunka-Grande. While the Tunka-133 instrument carries out observations, in case of an air-shower event the information about it reaches the Tunka-Grande data-acquisition system which, in turn, provides the information about the event observed by the Tunka-Grande detectors at the same time [232].

The individual detection station of the Tunka-Grande instrument consists of two major parts: a surface detector and an underground detector. A common building block of both detectors is a cased scintillator panel overviewed with a photomultiplier-tube photosensor. Twelve blocks form the surface detector covered with a shelter. Eight blocks form the underground detector placed in an underground concrete shelter. The total scintillator panels areas are 8 m^2 for the surface part and 5 m^2 for the underground part. The blocks are all connected to the same data-acquisition system of the station.

The surface part detects all particles, dominantly the electromagnetic component. The underground part detects mainly the muonic component of the shower since the other components lose all their energy in the layer of soil and concrete covering the underground detector. This technique of using two scintillators separated with an absorber layer has already shown its reliability in the KASCADE detector [128, 211]. Tunka-Grande reuses the scintillation materials already used in the former KASCADE-Grande detectors, which are, in turn, former EAS-TOP scintillator detectors.

Despite the high readiness of the equipment, the reconstruction procedures are still in the early development stage, however, even with this level of data analysis the instrument started to provide valuable scientific information [233].

4.2.3. TAIGA

The next generation of astrophysical instrumentation deployed at the Tunka site is joined under the name TAIGA standing for Tunka Advanced Instrument for cosmic rays and Gamma Astronomy [138]. Observation of gamma rays and their study become the main scientific goal for this generation of the instrumentation, and the cosmic-ray observation becomes a side topic.

The idea behind the new instrument is to utilize a combination of the two Cherenkov-light detection techniques: imaging and non-imaging, to compensate the drawbacks of each of those. Namely, it was proposed to build an air-Cherenkov timing array (HiSCORE) together with an array of imaging atmospheric Cherenkov telescopes for hybrid observation of gamma-ray-induced air shower. The deployment of the instrumentation and development of the data analysis is still ongoing, however, the recent results showed that the individual components of the system can already deliver scien-

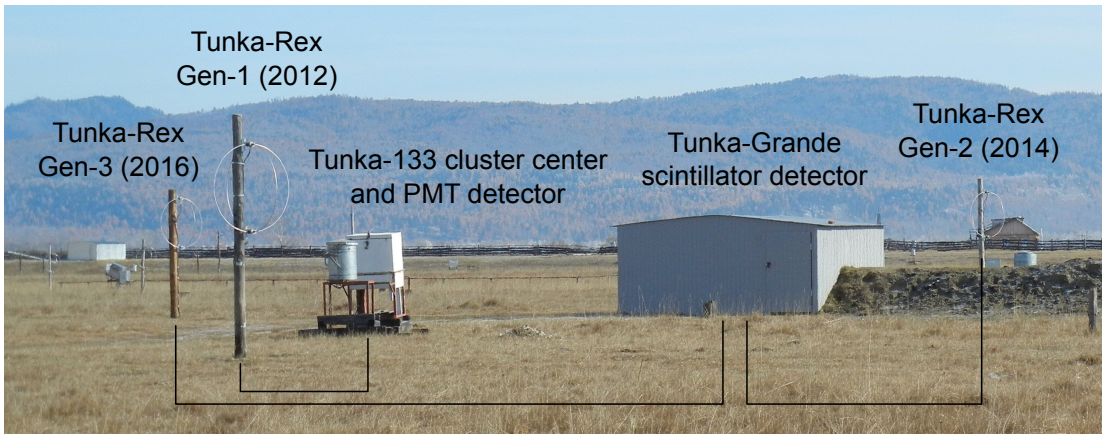

Figure 4.3: A cluster within the central, dense part of the detector site. The cluster is comprised of seven Cherenkov-light optical detectors of Tunka-133, one of which is visible on the picture, and its cluster DAQ components; the scintillation detector of Tunka-Grande with the surface and underground parts and the station DAQ components; the three SALLA-type antennas of Tunka-Rex connected to the DAQ components of the Tunka-133 and Tunka-Grande. The cluster DAQ components of Tunka-133 and Tunka-Grande are connected and are able to communicate in order to pass the trigger signal from one detector to the other.

tific results [230, 234]. Figure 4.2 shows the layout of the instrument by the end of the Tunka-Rex operation.

4.3. TUNKA-REX INSTRUMENTATION

Tunka-Rex is a digital radio-antenna array that started in 2012 as an extension of the astrophysical instrumentation located in the Tunka Valley [193]. The extension improved the scientific capabilities of the Tunka-133 instrument and used it as trigger. Also from the perspective of the data-acquisition system (DAQ), Tunka-Rex is a direct extension of the existing system capabilities with a set of radio antennas. The antennas use the formerly unused read-in channels of the Tunka-133 DAQ and channels of the Tunka-Grande DAQ. The extension went through several generations of the instrumental expansion. The number of the antennas in the field increased over time from 18 to 63. There were three stages of the expansion making four configurations of the antenna array (see Table 4.1 for details).

The Tunka-Rex instrument performed cosmic-ray observations from 2012 to 2019 during the winter seasons of the Tunka-133 and Tunka-Grande arrays. At the time of writing, the Tunka-Grande measurements have not yet been fully calibrated when operating with own trigger. Thus, the Tunka-Rex data obtained with the Tunka-Grande trigger are not used in the present work, but only the data obtained with the Tunka-133 trigger until 2017 since the Tunka-133 reconstruction of the later data was not available. In addition, the noise environment of the site becomes significantly larger due to the

Table 4.1: Generations of the Tunka-Rex radio array with corresponding years of operation and total number of the antennas within the generation. The last columns indicate the amount of available runs (nights) with each of the configurations and number of events detected using the standard analysis. Data of the season 2014/15 cannot be used due to a timing problem. The data after 2017 have not been included, because the Tunka-133 reconstruction of these events was not yet available.

Gen.	Years	# of antennas	# of runs	# of events
1a	2012/13	18	50	63
1b	2013/14	28	40	53
2	2015/16	44	83	35
3	2016/17	63	83	45

extensive deployment of new instrumentation. Thus, the usage of the data starting from 2017 was considered not feasible for the standard analysis used throughout this work.

Utilizing the Tunka-133 array as a trigger limits the observations to only clear, moonless nights. In addition to that limitation, the observations are limited to only winters since the summer time is reserved for the maintenance and calibration work on the entire system of detectors. Table 4.1 summarizes the number of Tunka-Rex observational runs with trigger from Tunka-133. Each run corresponds to a suitable observation night.

As mentioned above, the antenna configuration evolved. There were three generations of the array with, one, two, and three antennas per detector cluster of Tunka-133/Tunka-Grande. Also, not all deployed antennas operated during a given run (the duration of a run typically is one night). The actual antenna configuration changed over time. The main reason for these changes are occasional malfunctions of the antenna cabling system and low noise amplifier (LNA) due to the operation in the harsh weather conditions of the Siberian winter.

Figure 4.3 shows one of the clusters of the combined instrument. Since Tunka-Rex is an extension of the existing instrumentation, the layout of the Tunka-Rex array matches the layout of the Tunka-133 array and the Tunka-Grande array, which also was deployed later to extend the Tunka-133 capabilities. The Tunka-Rex instrument is a sparse array with approximately 200 m spacing between clusters. The sparseness of sampling of the air-shower radio-footprint increases the complexity of the data analysis and, potentially, compromises the precision of the reconstruction of air-shower parameters. The advantage of a sparse array is the larger area covered with the same number of antennas. Building on the experience and software of AERA, Tunka-Rex was one of the first radio arrays that developed a reliable data reconstruction procedure for a sparse distribution of antennas. The cluster operates in the following way. During the clear moonless nights,

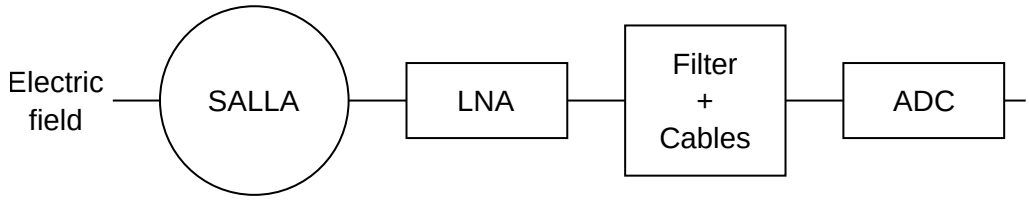

Figure 4.4: Block diagram showing the functional blocks of the Tunka-Rex analogue signal-detection channel. The radio emission from an air-shower, the electric field on the left side of the diagram, arrives at the antenna. The antenna detects the field and transforms it into an electric signal amplified by the low-noise amplifier (LNA) located inside the antenna structure. The signal propagates through the cables and is filtered before digitization with the analog-to-digital converter (ADC).

the Tunka-133 instrument is the leading instrument. Every time it detects an air shower, it triggers the Tunka-Grande stations to read out its response to the same shower. At the same time, the radio signals received by the antennas are recorded by the Tunka-133 and Tunka-Grande data-acquisition systems. Thus, for any shower the system records information about the observed Cherenkov light, radio emission, and particles at the surface.

The antennas of the array are of the short-aperiodic-loaded-loop type (SALLA) [206]. These antennas have a smooth sky coverage over the zenith and azimuthal angles and over the range of the operating frequencies. Tunka-Rex uses a traditional frequency band from 30 to 80 MHz. The antennas are active since they have LNA incorporated in the antenna structure in its upper part. The lower part hosts the loading resistors of the antenna. Each antenna has two independent, perpendicularly aligned channels measuring the incoming radiation. The LNA passes the signal to the cable which transfers it to the next analogue stage. The main filter amplifier in the Tunka-133 DAQ forms the next stage of the analogue signal-processing chain. It filters the frequency band from 30 to 80 MHz and amplifies the signal by approximately 56 dB. After this stage, Tunka-133 DAQ digitizes the signal with a 12 bit analogue-to-digital converter operating with 200 MHz sampling rate. It provides a trace of 1024 samples. Reusing the existing Tunka-133 systems is the key to the simplicity of the Tunka-Rex system and, thus, its reliability.

4.3.1. Multiplicity of Events

A radio instrument detects not only to cosmic-ray events but also to noise or background events. Finding the minimal number of antennas with signals for identification of the cosmic-ray-like events is one of the most critical procedure for an air-shower instrument and especially for a cosmic-ray radio instrument due to the high rate of the nuisance events.

For Tunka-Rex, initially, the derivation of the minimal number of antennas with

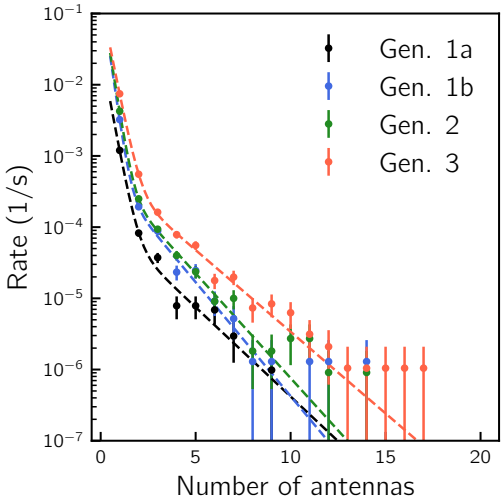

Figure 4.5: Rates of the events with a given number of signals. The lines indicate the two power laws fit to the data points. It is clearly visible that low-multiplicity and high-multiplicity data points are described by different power laws. Such a situation indicates that the low-multiplicity data, with less than three antennas per event, are dominated by noise or occasional background coincidences rather then the cosmic-ray air showers. The plot corresponds to all events with energies above 10^{16} eV and the level of the minimal signal-to-noise ratio set to suppress the noise signals with 95% efficiency.

signal in an event was selected purely from the perspective of possible reconstruction of the air-shower incoming direction with a plane front fit to the signal time stamps. Thus, only three signals are necessary to obtain a successful reconstruction of this kind. On the other hand, more reliable information about the minimal number of antennas forming actual cosmic-ray events can be obtained from the analysis of the multiplicity of events, namely, the amount of events having a certain number of signals. Because of the energy spectrum of the incoming events the functional behavior of the multiplicity should follow the Poisson point process since the multiplicity has a close relation to the cosmic-ray energy. Thus, one process corresponds to one power law in the multiplicity distribution. Adding a source of additional events adds one more power law to the distribution. In case of cosmic-ray instruments, this additional source is the nuisance events.

Figure 4.5 shows the obtained distribution of multiplicities of events observed by Tunka-Rex [235]. The picture reveals contributions of the noise and the cosmic rays to the total multiplicity distribution. It is very important to note that this picture is not generic. The shapes of the distributions correspond to the events with energies above 10^{16} eV and the minimal signal-to-noise ratio in trace such that the probability of the noise suppression is 95%. The shape of the distribution shows that the cosmic-ray-like events are dominant for the multiplicities down to three signals. Thus, this independent cross-check confirms the initial minimal number of signals in event from a different perspective.

4.4. SIGNAL PROCESSING

The Tunka-Rex data analysis can be summarized in two major stages: the signal processing aiming to restore the original electric field from the signals detected by the antenna channels, and the analysis of the radio footprint aiming to reconstruct the energy and $X_{\max}$. Each of these stages consists of several steps. The most important of those are described in the following sections[1].

The main idea behind the signal processing stage of the data analysis is to reconstruct the electric field of the air shower at each antenna position from the signals detected by the channels of individual antennas; and to prepare it to the further analysis of the footprint.

4.4.1. Reconstruction of the Electric Field

The radio antenna transforms the incoming air-shower electric field into currents on the antenna structure, which, in turn, get detected as voltages after the transformation by the electronic detection system. This transformation, or the instrument response, depends on the frequency components of the field, with unique transformation coefficients for the amplitude of the field and its phase. In addition, this transformation depends on the incoming direction, namely, on both the zenith angle and the azimuth angle.

Since the instrument response is known from careful simulations and a calibration campaign [237], it is possible to invert it and to apply it to the voltage traces measured by the individual antenna channels. The necessary information about the incoming direction of individual air showers comes from the Tunka-133 reconstruction of the Cherenkov-light measurements. When the incoming direction is known, the application of the inverted instrument response recovers the electric field strength observed by the antenna channels. Then, the recovered electric fields from the two antenna channels are combined to obtain the electric-field vector. A final step is the decomposition of the obtained vector in the geomagnetic coordinate system.

Disregard the presence of the external information about the air-shower incoming direction, a special iterative procedure finds the incoming direction of the air shower using only the timestamps of the radio signals. Thus, even in case of complete absence of the external information about the incoming direction, the radio-only reconstruction can be used for the inversion of the instrument response effects. Even though it is possible to use the radio-only information, the standard analysis uses the Tunka-133 reconstruction for the incoming direction, which is more accurate. However, in practice, the difference between the two cases is negligible.

Figure 4.6 shows the reconstructed trace of the air-shower electric field at one antenna as an example of a measured event.

[1]The Tunka-Rex data analysis is implemented within the same Offline software developed for the Pierre Auger Observatory [236]. The software contains all relevant information about the instrument response and data analysis including all functions and parameters. The software processes the data on an event-by-event basis.

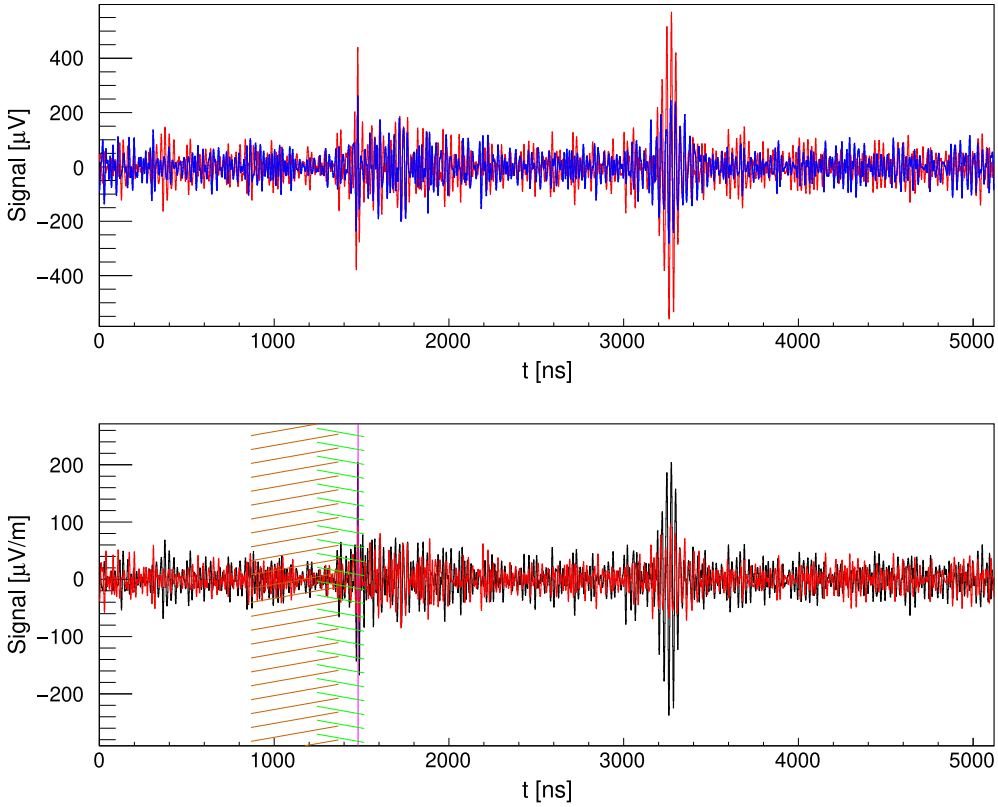

Figure 4.6: Tunka-Rex signals at one antenna of an example event. *Top*: The signals measured by a Tunka-Rex antenna. The colors indicate the two individual antenna channels. *Bottom*: The electric field reconstructed from the measured signal shown on the top panel. The colors indicate the components of the electric field vector in the geomagnetic coordinate system (black for $\boldsymbol{V} \times \boldsymbol{B}$, red for $\boldsymbol{V} \times \boldsymbol{V} \times \boldsymbol{B}$). The green-hatched area shows the position of the signal window. The brown-hatched area shows the position of the noise window found by sliding over the whole trace and finding the minimal noise level. The magenta line indicates the position on the found signal. The slight overlap of the signal-search and noise windows does not pose an issue since the signal is avoided anyway by the noise window because it would give a large contribution to the noise estimation. Another important aspect of the radio measurements clearly revealed on this picture is the presence of RFI in traces. In the given trace, a powerful RFI pulse is clearly distinguishable as an additional short signal located about the 3000 ns mark. Such powerful RFI pulse appearing in random positions along the trace is the main reason for introducing a sliding time window for the noise estimation.

4.4.2. Pulse Finding

The air-shower radio pulses are very narrow. It is challenging to find such pulses on the background of the ambient galactic radio noise, the thermal noise of the detection system, and the occasional radio-frequency interference (RFI) coming from the surroundings. The pulse finding procedure uses the envelopes of the reconstructed electric field traces to look for the air-shower radio pulses within pre-defined time windows. The envelope is defined as the instantaneous amplitude of the so-called analytic signal $u(t)$, which is a complex function defined as

$$u(t) = s(t) + i\mathcal{H}[s(t)], \tag{4.1}$$

where the symbol $s(t)$ denotes the initial trace. The letter $\mathcal{H}$ denotes the Hilbert transform, which is defined as the principal value of the following convolution integral

$$\mathcal{H} = \frac{1}{\pi}\ \text{p.v.} \int_{-\infty}^{+\infty} \frac{u(\tau)}{t-\tau}\, d\tau. \tag{4.2}$$

The instantaneous amplitude of the analytic signal $u(t)$ is simply its magnitude $|u(t)|$. The peak of the envelope within the signal time window is the reconstructed peak of the electric field of the air-shower radio emission.

Due to the constant presence of the noise in the trace, it is important to estimate the signal-no-noise ratio (SNR) for individual signals. Different definitions exist for SNR; for Tunka-Rex the squared ratio of the signal peak value S to the noise root-mean square N is used

$$\text{SNR} = \frac{S^2}{N^2}. \tag{4.3}$$

Since the trace contains sporadic noise, RFI, in addition to the steady state noise, which is the galactic and thermal noise, the position of the time window for noise estimation becomes crucial. The Tunka-Rex signal processing uses a sliding position of the noise-estimation window to avoid contamination by RFI components. The window scans the signal trace till it finds the position where the root-mean square is minimal. The noise in this window is treated as a pure noise signal without RFI.

The noise in the trace interferes with the signal and significantly changes the air-shower signal peak value. This change can be parameterized as a function of SNR for simulated signals and corrected for the measured signals. This correction provides the final estimation of the air-shower electric field strength [238].

4.4.3. Quality Cuts on Pulse Selection

One of the most important steps on the course of data analysis consists of separation of wide-band RFI pulses appearing within the signal window of the trace or indication of situations when the trace does not contain a signal within the corresponding time window. Few quality cuts are used to identify these two situations and filter out such signals from the further analysis.

SNR greater-than 16. One of the classical methods to suppress misidentification of upward fluctuations of noise as a signal is comparing the signal with a reference value. When the signal is higher than the value, it is recognized as a signal. The air-shower radio measurements use this concept by expressing the signal in terms of SNR of a given trace. Among all signal candidates, only those are recognized as signals which have SNR higher than a pre-defined value (SNR cut). The Tunka-Rex signal identification procedure starts with this classical SNR cut. The threshold value sets a given probability of misidentification of noise as a signal. In the Tunka-Rex this value is selected such that this probability is 5% for an individual antenna channel. Further steps in the signal identification procedure improve this value.

Peak width greater-than 50 ns. The air-shower radio signals are very wide-band with high synchronization between the harmonics. Thus, these signals appear as very short pulses in the time domain. The pulses are so narrow that it becomes their distinctive feature. The signal identification procedure uses this feature to separate false signals from the analysis. The procedure selects only those signals which have width of the envelope narrower than 50 ns.

Local SNR greater-than 10. Another parameter used in the signal identification is the so-called "local SNR". The approach to estimate this value is the same as for the usual SNR (see (4.3)), however, the time window for noise estimation differs to reflect the idea to estimate SNR not for the entire trace but for the close area near the signal. Thus, the noise for the local SNR is estimated withing the two windows spanning over 100 ns to the left and to the right from the signal starting from its boarders marked by its width around the peak value. Signals with local SNR value above the reference value 10 are used for further analysis.

All signals that passed the three mentioned selection criteria are considered as real air-shower radio signals and are used in the further analysis step reconstructing the shower parameters from the sets of measured signals.

4.5. RECONSTRUCTION OF SHOWER PARAMETERS

The reconstructed signals at the antennas contributing to individual events are the foundation for the further reconstruction. The main idea behind the Tunka-Rex event reconstruction consists in compensating the radio footprint asymmetry and reconstructing the air-shower parameters with a one dimensional lateral distribution function (LDF). After the procedure of the radio-footprint shower asymmetry compensation, an additional selection procedure takes place to separate out those events which do not have enough signals for sufficient reconstruction, or show a nonphysical behavior in the lateral distribution of the signals.

4.5.1. Correction of the Asymmetry

The interference of the electric fields coming from the two radio-emission mechanisms leads to the asymmetric shape of the radio footprint both in the shower plane and on the ground. This happens due to the fact that the polarization patterns of the two electric fields are different. One is linearly polarized, the other one is radially polarized with the field lines pointing from the shower axis. The summation of the electric fields with these polarizations leads to a constructive interference on the one side of footprint and a destructive interference on the other side. In contrast to other radio arrays, which try to accommodate the structural complexity coming from the two emission mechanisms into one asymmetric description of the radio footprint, the studies in Tunka-Rex showed that it is simpler and sufficient to compensate the asymmetry and describe the footprint with a one-dimensional lateral-distribution function.

The operator used in the Tunka-Rex data analysis for the radio-footprint asymmetry compensation has the following form

$$\hat{\mathsf{K}} = \frac{1}{\sqrt{\zeta^2 + 2\zeta \cos\phi_\mathrm{g} \sin\alpha_\mathrm{g} + \sin^2\alpha_\mathrm{g}}}. \tag{4.4}$$

The letter ζ denotes a function describing the strength of the asymmetry; the angles ϕ_g and α_g are the geomagnetic azimuth and the geomagnetic angle defined in the geomagnetic coordinate system (see 2.2.1 for details). For the Tunka-Rex analysis, ζ is selected to be a constant equal to 0.085. This operator acts on the asymmetric footprint $\mathscr{E}$ and leads to its symmetrization around the shower axis with r the distance from the shower axis

$$\hat{\mathsf{K}}\mathscr{E}\,(r, \phi_\mathrm{g}) = \mathscr{E}_\mathrm{sym}\,(r)\,. \tag{4.5}$$

The LDF in its symmetrized form is the basis for the reconstruction of shower parameters. The symmetrization of the complex, asymmetric footprint of the air-shower radio emission converts it into a one-dimensional function of the lateral distance. Such a conversion implies usage of one-dimensional functions for the reconstruction, which is a more robust approach than trying to fit a two-dimensional function to the observed signals, especially for the case of a sparse air-shower radio array such as Tunka-Rex.

4.5.2. Quality Cuts on Event Selection

Several criteria select events with sufficiently high quality to lead to a reasonably stable reconstruction of the air-shower parameters. The basis of these criteria is the basic knowledge about the LDF behavior and an understanding of the main factors influencing the fitting procedure.

Checking for unexpectedly large signals. The expected behavior of the symmetrized LDF further away than the Cherenkov-like peak is a decreasing amplitude with rising lateral distance. Thus, if the LDF contains some unexpectedly large signals, outliers, at a given distance, it means that such signals are most probably caused by

noise and should be filtered out from the events. The criterion for this filtration is such that the signal S_{i+1}, which is the signal at the nearest, more distant antenna, should be smaller than the following threshold, $S_{\rm up}$, derived from the signal amplitude, S_i, and its uncertainty, σ_S, at a given distance

$$S_{\rm up} = 1.2S_i + 3\sigma_S. \tag{4.6}$$

If the amplitude of the further signal, S_{i+1}, exceeds this threshold, the filtration procedure removes the signal from the analysis.

Direction reconstruction match within 0.5°. When an event has at least three antennas, it is possible to reconstruct its incoming direction. The reconstructed direction is compared to that reconstructed by Tunka-133, and if the angular difference between them is smaller than 0.5°, the event passes for further reconstruction. The intrinsic accuracy of Tunka-133 is on the level of 0.1° for air showers with energies above 10 PeV.

4.5.3. Lateral Distribution Function

The parameters of the symmetrized radio footprint carry information about the macroscopic parameters of the air shower such as the cosmic-ray energy and the depth of the shower maximum. The selection of the proper lateral distribution function is critical for the observational data analysis. An incorrect selection reduces the accuracy of the reconstruction and can lead to a dramatic drop of the reconstruction efficiency. Additional complexity comes from the fact that the Tunka-Rex instrument is a sparse array. This means that the number of measurement points for a given shower is very limited. Thus, using a many-parameter function will lead to frequent misreconstructions of air-shower parameters.

LDF used in the Tunka-Rex data analysis has a modest number of parameters. In combination with the geometry of air showers accurately obtained from the Tunka-133 instrument, this allows for reconstructing air-shower events with three signals only. The symmetrized lateral distribution has the Gaussian form

$$\mathscr{E}_{\rm sym} = \mathscr{E}_0 \exp\left(-\frac{1}{2}\frac{(r-\mu)^2}{\sigma^2}\right). \tag{4.7}$$

The position of the peak and width of the distribution have the following functional dependence

$$\mu = r_0 - \frac{b}{2a}, \tag{4.8}$$

$$\sigma = \frac{1}{2\sqrt{a}}, \tag{4.9}$$

motivated by their change with the depth of the air shower maximum [171]. The parameters $\mathscr{E}_0$, a and b hold the information about the air-shower energy and the depth of its maximum. Finding the connection between the parameters of the LDF and the air-shower parameters is the essence of their reconstruction.

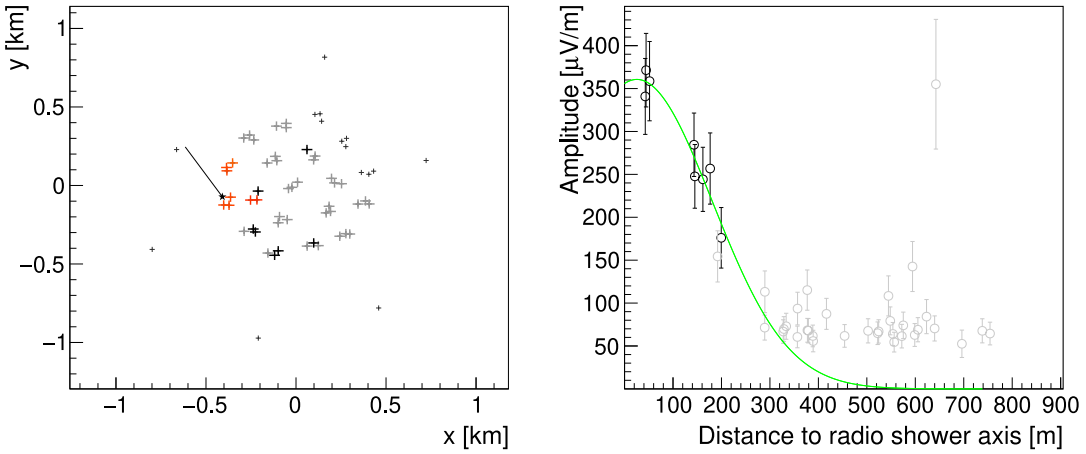

Figure 4.7: An example of Tunka-Rex event (event #1123 observed on December 28th, 2016). *Left*: map showing the distribution of the detected signals across the Tunka-Rex array. The crosses mark the positions of the antennas. The red crosses mark the antennas with signals. The black star with the line indicates the location of the shower core and the projection of the shower axis to the detector plane. *Right*: the symmetrized LDF. The black circles indicate the signals used for the LDF fit. The gray circles show the noise signals and RFI. The green line shows the LDF fit to the signals. The reconstructed energy is 0.211(11) EeV; the reconstructed $X_{\max}$ equals 632(47) g/cm^2.

The reconstruction procedure uses the lateral distribution parameters on a given distance for estimation of the shower energy and the depth of the maximum. To simplify the calculations for the reconstruction, the lateral distribution is written in the following form

$$\mathscr{E}_{\text{sym}} = \mathscr{E}'_0 \exp\left(a\,(r-r_0)^2 + b\,(r-r_0)\right), \tag{4.10}$$

which is equivalent to (4.7).

4.5.4. Estimation of Shower Parameters

The parameters of the symmetrized lateral distribution which are sensitive to the shower macro-parameters are the function value and the slope at specific reference distances.

The function value at a given reference distance r_e is related to the shower energy with the power equation

$$E_{\text{CR}} = \kappa \left(\frac{\mathscr{E}_{\text{sym}}\,(r_e)}{1\text{V/m}}\right)^{\lambda}, \tag{4.11}$$

where letter κ denotes the energy-calibration constant, letter λ denotes the energy-calibration power constant, which equals to unity for the present work as expected for coherent radio emission. The slope η of the lateral distribution is defined as a logarithmic derivation

$$\eta = \frac{\mathrm{d}}{\mathrm{d}r} \ln \mathscr{E}_{\text{sym}}\,(r) = \frac{1}{\mathscr{E}_{\text{sym}}} \frac{d}{dr} \mathscr{E}_{\text{sym}}\,(r) = 2a\,(r-r_0) + b, \tag{4.12}$$

and is sensitive to the depth of shower maximum. Taking the slope parameter η on its reference distance r_{x}, while performing the fit with $r_0 = r_{\mathrm{x}}$, makes it equal to b. The estimation of the shower maximum depth is done with the following relation

$$X_{\max} = X_{\mathrm{det}}/\cos\theta - \left(A + B\ln\left(b - \bar{b}\right)\right). \tag{4.13}$$

The first term is the full slant depth of the atmosphere along the line with the zenith angle θ, given that the vertical atmospheric depth of the detector is X_{det}. The second term is the parametrization of the distance to $X_{\max}$ as function of the LDF parameter b, the other letters (A, B, $\bar{b}$) are free parameters fixed during the calibration against the CoREAS Monte-Carlo simulations.

In order to make the fitting procedure more stable, the parameter a of the lateral distribution function has a fixed value according to the parametrization

$$a = (A_{200} + A_{201}E_{\mathrm{pr}}) + (A_{210} + A_{211}E_{\mathrm{pr}})\cos\theta, \tag{4.14}$$

where the letter E_{pr} denotes the preliminary estimated energy with a pre-fit procedure. This procedure fits parameters of a simpler lateral distribution function, an exponential distribution, to the data and uses the value of the function at a given distance as a preliminary energy estimator [171]. The parameters A_i do not hold any specific meaning and are defined during the calibration against the Monte-Carlo simulations.

4.5.5. Improvements of the Reconstruction

In the present work, several aspects of the data analysis were improved. This section briefly summarizes them.

Update of the antenna pattern. During the present work it was found that the antenna pattern used initially was not symmetrical. To correct this, a new symmetric and finer resolution approximation of the antenna was used to calculate new pattern, which was incorporated into the data reconstruction software. The cross-checks showed that the results of the earlier data reconstruction are not affected. The changes are beyond the sensitivity of the array.

Signal correction for the noise level. To achieve a better signal reconstruction accuracy, the Tunka-Rex data analysis corrects the reconstructed signals for the presence of noise. The function for this correction was updated during the present work. Now a new parametrization function is used for this quantity. The function for this correction term has a form of a sum

$$f_{\mathrm{c}}(\mathrm{SNR}) = L_1^{f_{\mathrm{c}}}(\mathrm{SNR}) + L_2^{f_{\mathrm{c}}}(\mathrm{SNR}), \tag{4.15}$$

where both functions of the sum have the form of Lorentzian-like functions of the signal-to-noise ratio, SNR

$$L_{1,2}^{f_{\mathrm{c}}}(\mathrm{SNR}) = \frac{a_{1,2}^{f_{\mathrm{c}}} \cdot \mathrm{SNR}}{\left(\mathrm{SNR} - b_{1,2}^{f_{\mathrm{c}}}\right)^2 + c_{1,2}^{f_{\mathrm{c}}}}. \tag{4.16}$$

The coefficients $a_{1,2}^{f_c}$, $b_{1,2}^{f_c}$, and $c_{1,2}^{f_c}$ are obtained from the simulations after adding the measured noise samples from the Tunka-Rex noise library [238].

Signal uncertainty estimation. The signal uncertainty is one of the crucial components in the procedure of fitting the LDF parameters to the observed distribution of signals since wrong uncertainties bias the estimation of the LDF and, in turn, air-shower parameters. During the present work, the function estimating the uncertainties with respect to the signal strength was updated. Now a new parametrization function is used for this quantity. The functional form for the signal uncertainty, σ, is chosen the same as for the signal correction factor described in the previous paragraph

$$\sigma(\mathrm{SNR}) = L_1^{\sigma}(\mathrm{SNR}) + L_2^{\sigma}(\mathrm{SNR}), \tag{4.17}$$

where both functions of the sum have the form of Lorentzian-like functions

$$L_{1,2}^{\sigma}(\mathrm{SNR}) = \frac{a_{1,2}^{\sigma} \cdot \mathrm{SNR}}{\left(\mathrm{SNR} - b_{1,2}^{\sigma}\right)^2 + c_{1,2}^{\sigma}}. \tag{4.18}$$

The coefficients $a_{1,2}^{\sigma}$, $b_{1,2}^{\sigma}$, and $c_{1,2}^{\sigma}$ are obtained in from the simulations after adding the measured noise samples from the Tunka-Rex noise library [238].

Increasing the dataset size. The air-shower observation datasets were updated for this work. In addition to the previously used data, they include data from the last observational season 2016/2017. The data from more recent observations are not yet analyzed by the Tunka-133 group and, thus, are not used in the present work.

4.5.6. Summary Information about the Air-Shower Dataset

The air-shower data used in this work are measurements of the radio traces by the Tunka-Rex array triggered with the Tunka-133 Cherenkov-light timing array. The data triggered with Tunka-Grande are not used in this work since the Tunka-Grande scintillation array was not yet calibrated during the work. This section summarizes the main features of the collected data.

As already mentioned above, Tunka-Rex operated from 2012 through 2019. Table 4.1 shows the complete set of the operating seasons, which are considered in this work, together with the antenna configuration and the number of runs (nights). The season of 2014/15 is excluded due to an unresolved problem with the timing information in the Tunka-133 DAQ system. The total operation time of the Tunka-Rex array is $4.2387(86) \times 10^6$ s. On the course of this time, the Tunka-Rex array observed 196 events passing the selection criteria built into the data analysis. During the further analysis all events are combined into one dataset.

Tunka-133 measures cosmic-ray induced air showers coming from all directions up to the zenith angle of 50°, due to the limitations of the optical system of the modules. Because of this, the field of view of the Tunka-Rex array is also limited to the same range of zenith angles. The distribution of the core locations and the air-shower incoming

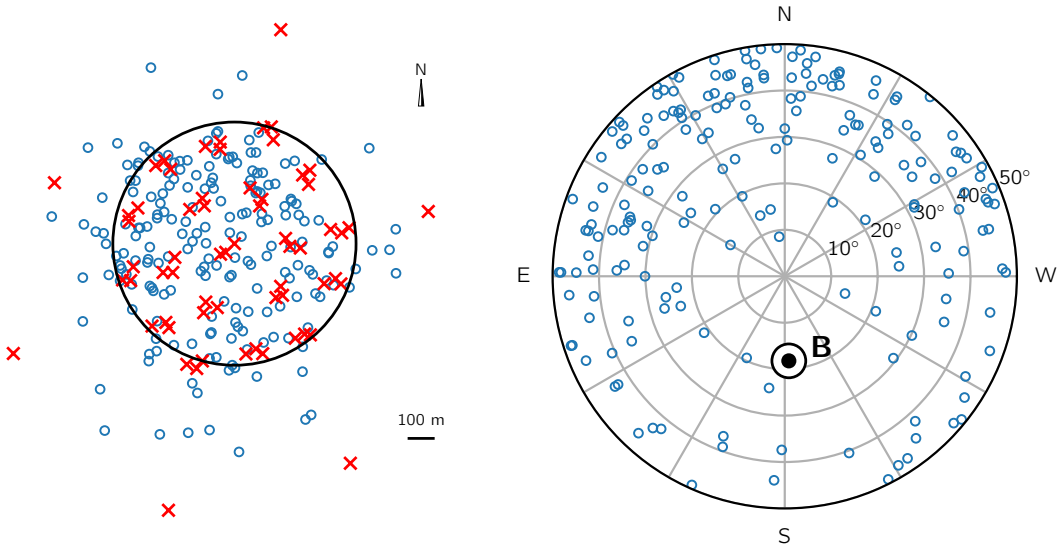

Figure 4.8: Summary plots on all events observed by the Tunka-Rex array (196 events collected over 1068.4667(83) hours, all four seasons). *Left*: The distribution of the shower cores for all events. The circles indicate the location of the shower cores of the events, the crosses show the layout of the Tunka-Rex antennas. The black circle of radius of 450 m shows the size the fiducial area of the array. *Right*: The distribution of the incoming directions on the sky. The maximal zenith angle of 50° comes from the limited acceptance angle of the Tunka-133 optical detector module. The circles indicate the shower incoming directions of the events.

directions are shown in Figure 4.8. The core distribution reveals an approximately uniform random distribution over the instrument area. The distribution of the incoming directions, however, looks very non-uniform, which reflects the physics of the radio emission and, particularly, the dominance of the geomagnetic mechanism in the radio emission production.

Figure 4.9 (left) shows the distribution of the reconstructed cosmic ray energies of the observed events. As it can be clearly seen on this plot, the energy region below the 10^{17} eV has a suppressed efficiency. In addition to the energies reconstructed by Tunka-Rex, the energies reconstructed by Tunka-133 are shown for a comparison.

Figure 4.9 (right) shows the distribution of the reconstructed $X_{\max}$ of the observed air-shower events. The $X_{\max}$ reconstructed by Tunka-133 for the same events is shown as well for a comparison.

4.5.7. Cross-Check of the Tunka-Rex Reconstruction

The Tunka-Rex array is a unique instrument since it is triggered by the Tunka-133 Cherenkov-light timing array, which features a lower energy threshold and well developed air-shower reconstruction procedures. The unique configuration of both instruments enables us to cross check the reconstructed energy and $X_{\max}$ between the two instruments.

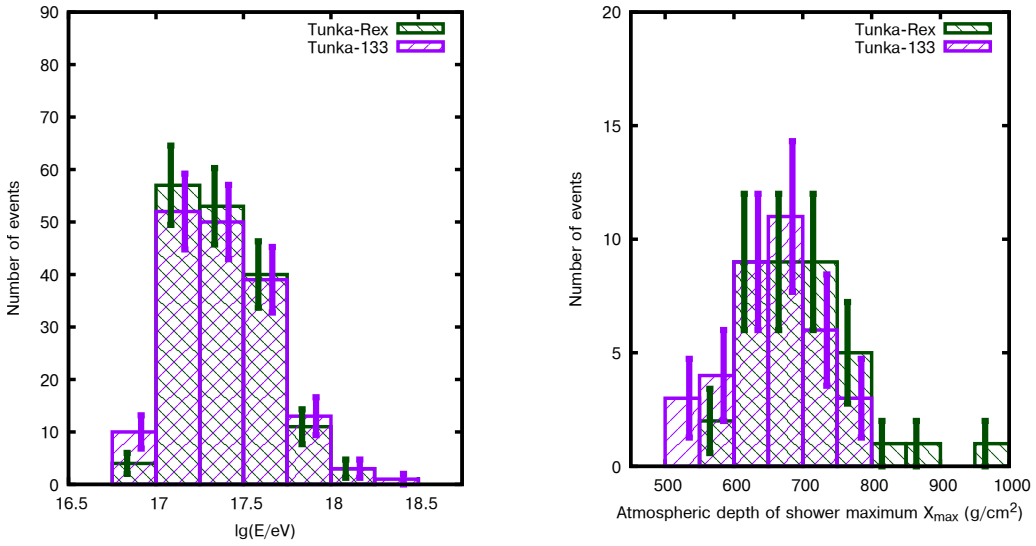

Figure 4.9: Summary plots on all Tunka-133 triggered events observed by the Tunka-Rex array and passing the quality cuts built into the data analysis (196 events collected over 1068.4667(83) hours, all four seasons). *Left*: Distribution of the shower energy reconstructed by Tunka-Rex. *Right*: Distribution of the $X_{\max}$ parameter reconstructed by Tunka-Rex.

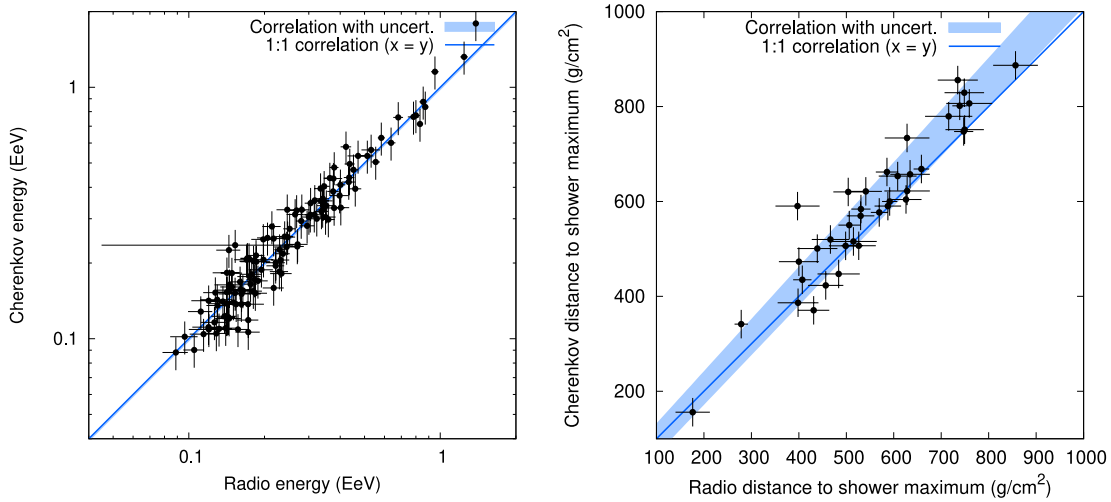

Figure 4.10: Comparison of the Tunka-Rex reconstruction of energy (on the left) and $X_{\max}$ (on the right) against the Tunka-133 reconstruction.

Figure 4.10 presents the results of the cross-check. The comparison of the energy uses the whole combined dataset of the reconstructed events. The overall shape of the distribution reveals a good agreement between both reconstructions without a noticeable energy dependent systematic offset, which confirms earlier results.

The comparison of the $X_{\max}$ reconstruction is performed on a subset of events selected with additional cuts. The selected events have accurate reconstruction (statistical reconstruction uncertainty less than 50 g/cm^2); have the core within 500 m radius of the array (used only for this particular cross-check); and have at least one antenna with signal further than 200 m from the shower axis for improving the sensitivity of the reconstruction procedure.

4.6. CONCLUDING REMARKS

The fully developed and reliable procedures for the reconstruction of air-shower parameters opens a way towards the measurement of the cosmic-ray characteristics as astrophysics phenomena, particularly, the energy spectrum and the average $X_{\max}$ as function of the cosmic-ray energy. However, it is not a straightforward problem to estimate these characteristics from radio measurements since the instrument efficiency estimation for cosmic-ray radio arrays remained a challenging problem before the present work. The main difficulty comes from the physics of the radio emission leading to an efficiency suppression close to the direction of the geomagnetic field, which complicates the selection of a full efficiency sky region. In turn, the proper selection of this region is crucial for a reliable cosmic-ray characterization, in particular, to avoid biases such as on the mass of the cosmic-ray nuclei.

The central topics of the next chapter are a new semi-analytical approach for the efficiency estimation and a specific model built according to this approach. The approach and the model have a generic nature, however, for the present work, the Tunka-Rex radio array is used as a particular example of their application.

CHAPTER FIVE

EFFICIENCY OF A RADIO ARRAY FOR COSMIC RAYS

The efficiency of a cosmic-ray instrument is one of the key characteristics in the transition from studying individual air-shower events to studying properties of the cosmic-ray flux like the energy spectrum, chemical composition, and incoming directions. The chief purpose of this chapter is to introduce in detail a phenomenological model for the estimation of the efficiency of a cosmic-ray radio array. The model was developed for the Tunka-Rex array, however, it can be applied to any other radio array after appropriate adaptations.

The usual approach to the efficiency estimation consists of processing Monte-Carlo events with an instrument response and an analysis procedure. These steps result in a quantitative estimation of the instrument efficiency for air showers with given parameters. The core component in this approach is a library of Monte Carlo events. Preparation of such library is computationally demanding and time consuming especially in cases when an efficiency study requires a fine coverage of incoming directions and the instrument fiducial area. The situation becomes even more problematic in case of radio-emission simulations because of the high complexity of the computation process in comparison to the particle only simulations.

The main idea behind the efficiency model developed for Tunka-Rex[1] consists of using explicit probabilistic properties of both, the air showers detected by the array and their detection process. A set of probability density functions parameterize these properties in a specific mathematical form.

The organization of the chapter is as follows. The first section introduces the details of a model for the radio-footprint spatial distribution and its uncertainties. The following sections describe a probabilistic approach to the procedure of the signal detection by individual antenna and then by the entire antenna array. The results of a validation of the developed model complete the chapter.

5.1. SPATIAL DISTRIBUTION OF RADIO SIGNALS

The spatial distribution of the radio signals coming from the air shower is the starting point for modeling the detection efficiency. The probability density of appearing an electric field with a given strength describes the radio footprint in the framework of the model. The Tunka-Rex lateral distribution function is the foundation to this probability

[1] An early version of the model discussed in this chapter was published in [235]. The present, more advanced version was published in [239].

density. Using the same radio footprint in the aperture estimation as in the reconstruction procedure enables introducing the instrumental effects without additional functions.

5.1.1. Lateral Distribution Function

The foundation of the probability density to observe an electric field with a given strength is the Tunka-Rex asymmetric lateral distribution function, which parametrizes the shape of the radio footprint as function of the cosmic-ray energy and the depth of the shower maximum. The main idea behind this is to use the lateral distribution for predicting the signals rather than inferring the cosmic-ray and shower parameters. This prediction provides the mean value of the probability density. Its variation will be obtained below from the comparison of the predicted values against Monte-Carlo simulations.

Let us begin the derivation of the probability density with the Tunka-Rex symmetrized lateral distribution function, which is used for the depth of the shower maximum estimation. The functional form of this function repeats (4.10) with the reference distance $r_0 = r_\mathrm{x}$ used for the depth-of-shower-maximum estimation in the event reconstruction procedure

$$\mathscr{E}(r)_\mathrm{sym} = \mathscr{E}_0 \exp\left[a\,(r - r_\mathrm{x})^2 + b\,(r - r_\mathrm{x})\right]. \tag{5.1}$$

The normalization $\mathscr{E}_0$ of the function is related to the estimation of the shower energy E. To find this normalization, we take the the value of this function in (5.1) at the distance r_e, the reference distance for the shower-energy estimation in the reconstruction procedure

$$\mathscr{E}_\mathrm{sym}\,(r_\mathrm{e}) = \mathscr{E}_0 \exp\left[a\,(r_\mathrm{e} - r_\mathrm{x})^2 + b\,(r_\mathrm{e} - r_\mathrm{x})\right] = \frac{E}{\kappa} \tag{5.2}$$

where κ denotes the energy calibration coefficient used in the reconstruction. Equating the last two expressions gives the equation for $\mathscr{E}_0$ connecting it to the reference distances and the shower energy via the corresponding calibration constant

$$\mathscr{E}_0 = \frac{E}{\kappa} \exp\left[-a\,(r_\mathrm{e} - r_\mathrm{x})^2 - b\,(r_\mathrm{e} - r_\mathrm{x})\right]. \tag{5.3}$$

The next step is to find expressions for the parameters a and b of the lateral distribution. The first parameter is already used in the reconstruction in form of a certain parametrization (see (4.14)). We reuse it here in the same form with the only change that the energy in the equation is the shower energy[2]

$$a = (A_{200} + A_{201}E) + (A_{210} + A_{211}E)\cos\theta.$$

The parameter b connects the slope of the lateral distribution at the reference distance r_x with the depth of shower maximum. The connection is given in (4.13), however, for completeness we repeat it here

$$X_\mathrm{max} = \frac{X_\mathrm{det}}{\cos\theta} - \left(A + B\ln\left(b - \bar{b}\right)\right).$$

[2]All repeated formulas are given without additional numeration.

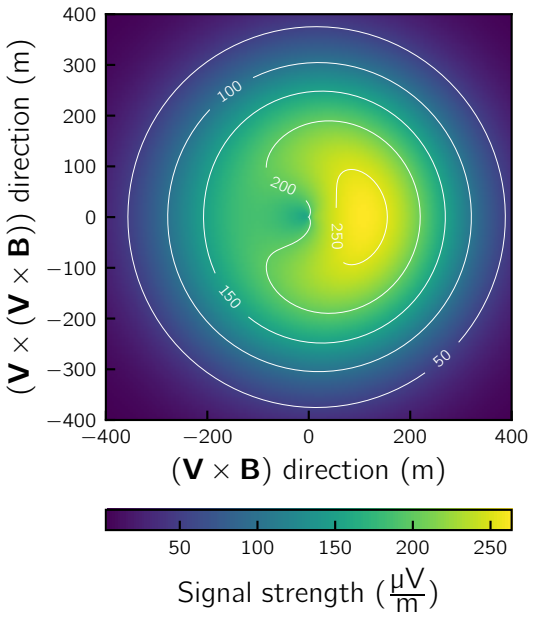

Figure 5.1: Spatial distribution of the most probable values of the electric field coming from an air shower with the following parameters: $\lg(E/1\text{ eV}) = 17.5$, $X_{\max} = 400$ g/cm^2, $\theta = 40°$, $\alpha_g = 30°$. The shown distribution is the Tunka-Rex asymmetric lateral distribution function. The plot shows the distribution in the geomagnetic coordinate system, which is built from the vectors of the shower propagation direction $\boldsymbol{V}$ and the local geomagnetic field direction $\boldsymbol{B}$. To obtain the distribution on the array, the shown distribution is projected geometrically to the array plane.

From this equation we find the expression for the parameter b connecting it to the depth of shower maximum and to the parameters of the reconstruction

$$b = \bar{b} - \exp\left[\frac{1}{B}\left(\frac{X_{\text{det}}}{\cos\theta} - X_{\max} - A\right)\right]. \tag{5.4}$$

The symmetrized lateral distribution (5.1) with the parameters a, b, and $\mathscr{E}_0$ (given by (4.14), (5.4), and (5.3) correspondingly) gives the mean value of the probability density function of appearing a given signal strength at a certain lateral distance from the shower axis. Another aspect is the asymmetry of the electric field distribution over the footprint. As it was mentioned above in Section 4.5.1, an operator (4.4) contains the asymmetry effects over the footprint. To restore the initial asymmetric shape of the radio footprint, we apply an inverted version of asymmetry compensation operator (4.4)

$$\mathscr{E} = \hat{\mathsf{K}}^{-1}\,\mathscr{E}_{\text{sym}}. \tag{5.5}$$

The form of the inverse operator can be obtained explicitly as

$$\hat{\mathsf{K}}^{-1} = \sqrt{\zeta^2 + 2\zeta\cos\phi_{\text{g}}\sin\alpha_{\text{g}} + \sin^2\alpha_{\text{g}}}. \tag{5.6}$$

Figure 5.1 shows the exemplary spatial distribution of air-shower radio signals over the shower plane.

The spatial distribution of the signals over the antenna array has a probabilistic nature which can be described with a probability density. The formulas presented above describe only the mean value of the probability density. The next step is to estimate the variance of this value.

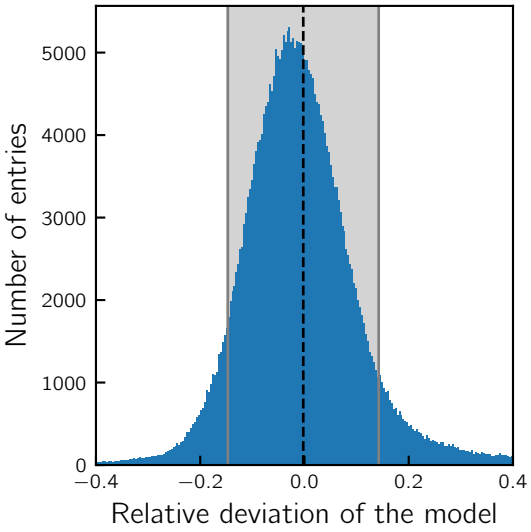

Figure 5.2: Unnormalized histogrammed residuals between the symmetrized lateral distribution function and the symmetrized Monte-Carlo radio signals divided by the model value. The vertical black dashed line indicates the location of the mean value of $-0.0023(3)$. The gray area indicates the width of two standard deviations. The obtained value of the standard deviation is 0.1447.

5.1.2. Uncertainty of the Lateral Distribution Function

The uncertainties of signal prediction by the lateral distribution characterize both the probabilistic nature of the signal strength and the accuracy of the model description. The better the lateral distribution model is, the smaller the uncertainties for the signal prediction it should provide. However, some level of uncertainty is always present due to the shower-to-shower fluctuations and presence of air-shower features not explicitly treated by the macroscopic parameters.

To estimate the uncertainty of the lateral distribution used in the present work, we make a straightforward comparison of its predictions to the CoREAS Monte-Carlo signals. The model contains the asymmetry operator which is a linear operator. It does not introduce any new functional dependence to the signal on a given location but only rescales it. Thus, we exclude this operator from the comparison procedure and symmetrize the Monte-Carlo signals instead. Figure 5.2 shows the histogrammed residuals between the symmetric part of the lateral distribution function and symmetrized Monte-Carlo radio signals.

The mean value, described in Section 5.1.1, and the variance, obtained in this section, are the first two statistics of the probability density function for the distribution of the electric field over the radio footprint of a shower. In principle, there exist higher-order statistics but they are out of the scope of this work. To combine the obtained statistics, we use a Gaussian distribution as an approximation of the signal strength distribution at a given spatial point. The mean of this distribution is the signal strength predicted by the radio footprint model; the variance of this distribution is simply the square of the found standard deviation of signals from the mean value. The Gaussian distribution constitutes a natural tool for modeling a distribution when only a mean value and a variance are known.

The next step in modeling the array efficiency is to understand how the predicted signals will be detected by the individual antennas.

5.2. SIGNAL DETECTION WITH ANTENNA

The main device of detection of a cosmic-ray radio-detection instrument is an antenna. The perception process of air-shower radio signals has a probabilistic nature due to the fact that together with the signal the antenna detects the electric fields from other sources like the Galaxy and the antenna surroundings. All these electric fields that are not related to the air-shower, form the noise which has a sporadic behavior with occasional sudden bursts of the amplitude.

The manifestation of the probabilistic phenomenon of the signal detection is in the fact that a signal of the same strength can be either detected by an antenna or not, depending on the instant noise level seen by this antenna. Thus, since the stochastic nature of the noise is out of control during the observations, this effect is described in form of a probability of the signal detection.

5.2.1. Detection Probability of Individual Signals

Building the probability density of the signal detection by an antenna begins with a multiple processing of air-shower signals through the signal processing pipeline of the Tunka-Rex reconstruction procedure. The multiple processing is carried out in presence of noise in such a way that each time the noise sample is unique. To have a better coverage of the stronger signals, the analysis is based on the processing of Monte Carlo air-showers generated by cosmic rays with an energy of 10^{18} eV. The signals from each of the events were processed 30 times with different noise samples. Depending on the noise condition, the procedure cannot always recognize the signal in the background noise. The estimation of the individual-signal detection probability is the binomial proportion of the number of times the signal was recognized to the total number of trials.

5.2.2. Parametrization of Detection Probability

Most Probable Value. The probability density of the signal detection by the individual antenna is parameterized for further use. The parametrization is based on a hyperbolic tangent function with the location term $S_{1/2}$ defining the position of the half probability, the scaling factor S_0, and the adjustment of the function value to the $[0, 1]$ range

$$\frac{1}{2} + \frac{1}{2} \tanh \frac{S - S_{1/2}}{S_0}. \tag{5.7}$$

The variable S of the function is the signal strength. This function has a general symmetric shape. An asymmetric behavior, is introduced by a linear dependence of the scaling parameter

$$S_0 = S_0' + S_0'' S. \tag{5.8}$$

Thus, by inserting this equation into (5.7) the functional form for the parametrization takes the form

$$p_0(S) = \frac{1}{2} + \frac{1}{2} \tanh \frac{S - S_{1/2}}{S_0' + S_0'' S}. \tag{5.9}$$

The data does not appear to have a significant zenith dependence. Thus, this was not included into the parametrization.

Transition to Probability Density. The generalization used in this work consists in considering the probability to detect a signal with an antenna not as a constant but as a random variable with a certain probability density distribution. The parametrization (5.9) provides only the most probable value of the probability density. The description of the full probability density demands some functional form. Estimation of the detection probability with the binomial proportion suggests using the binomial distribution as the probability density. However, for generalization, we can extend the probability density to the continuous domain with the beta distribution

$$P = \frac{p^{\alpha-1}\,(1-p)^{\beta-1}}{\mathrm{B}(\alpha,\beta)}, \tag{5.10}$$

where parameters α and β of the beta function hold the dependence on the most probable value

$$\alpha = np_0 + 1, \tag{5.11}$$

$$\beta = n - np_0 + 1, \tag{5.12}$$

with n denoting the number of trials in the binomial procedure of the individual-signal detection probabilities. For the present analysis $n = 30$. The symbol $\mathrm{B}(\alpha,\beta)$ denotes the beta function defined as

$$\mathrm{B}(\alpha,\beta) = \frac{\Gamma(\alpha)\Gamma(\beta)}{\Gamma(\alpha,\beta)}. \tag{5.13}$$

The similarity between the beta distribution and the binomial distribution can be seen directly. Replacing the distribution parameters in (5.10) with their definitions and using the definition of the beta function gives

$$P = \frac{\Gamma(n+2)}{\Gamma(k+1)\Gamma(n-k+1)}\,p^k\,(1-p)^{n-k}\,. \tag{5.14}$$

The letter k denotes the combination np_0, which holds a meaning like number of successes, but for the continuous case. The functional form of (5.14) repeats the form of the binomial distribution with only a slight difference in the normalization. The straightforward conversion of the normalization of the binomial distribution, the binomial coefficient, to the continuous domain using the known relation between gamma function and factorial $\Gamma(n+1) = n!$ gives

$$\binom{n}{k} \stackrel{\mathrm{def}}{=} \frac{n!}{k!(n-k)!} = \frac{\Gamma(n+1)}{\Gamma(k+1)\Gamma(n-k+1)}, \tag{5.15}$$

which only slightly differs from the normalization of the distribution (5.14). Some difference, however, is expected due to the extension from the discrete domain to the continuous domain.

The parameters of the probability density (5.10) are obtained with an optimization procedure involving a negative logarithmic-likelihood function. The basis for this

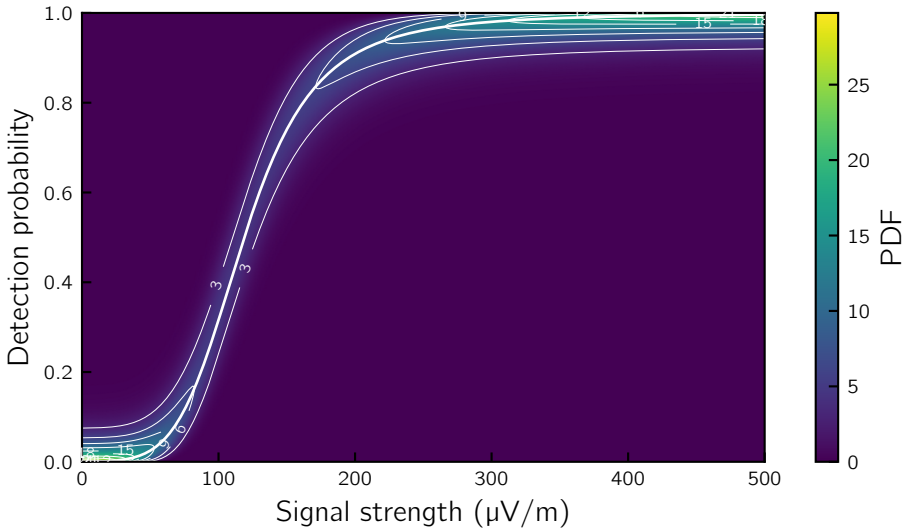

Figure 5.3: The probability density function (PDF) of the signal detection on the individual antenna level. The thick line shows the dependence of the most probable value of the probability to detect a signal of a given strength.

function, along with the functional form of the probability density, is the data on the detection probabilities of the signals of various strengths. As mentioned above, these data are the result of the multiple processing of the Monte-Carlo signals. The logarithmic likelihood function has the following form

$$\mathcal{L} = \sum_i (\alpha_i - 1) \ln p_0(S_i) + (\beta_i - 1) \ln(1 - p_0(S_i)) - \ln \mathrm{B}(\alpha_i, \beta_i) \tag{5.16}$$

with summation running through the whole dataset. The parameters α_i and β_i hold information about the probabilities for the individual signals obtained via the multiprocessing procedure

$$\alpha_i = k_i + 1, \tag{5.17}$$

$$\beta_i = N_i - k_i + 1. \tag{5.18}$$

The letter k_i denotes the number of successful detections of a given signal. The letter N_i denotes the total number of trials.

The optimization procedure was performed with the MINUIT software [240] wrapped in a modern Python interface [216]. This piece of software minimizes a given function. Thus, to find the most probable, maximal, logarithmic likelihood value with a minimization procedure, (5.16) is taken with the opposite sign, which gives a negative log-likelihood function.

The initial values for the minimization are

$$S_{1/2} = 130, \qquad S_0' = 50, \qquad S_0'' = 0.1. \tag{5.19}$$

During the procedure the values vary within the limited ranges

$$S_{1/2} \in [50, 200], \qquad S_0' \in [1, 100], \qquad S_0'' \in [0, 50]. \tag{5.20}$$

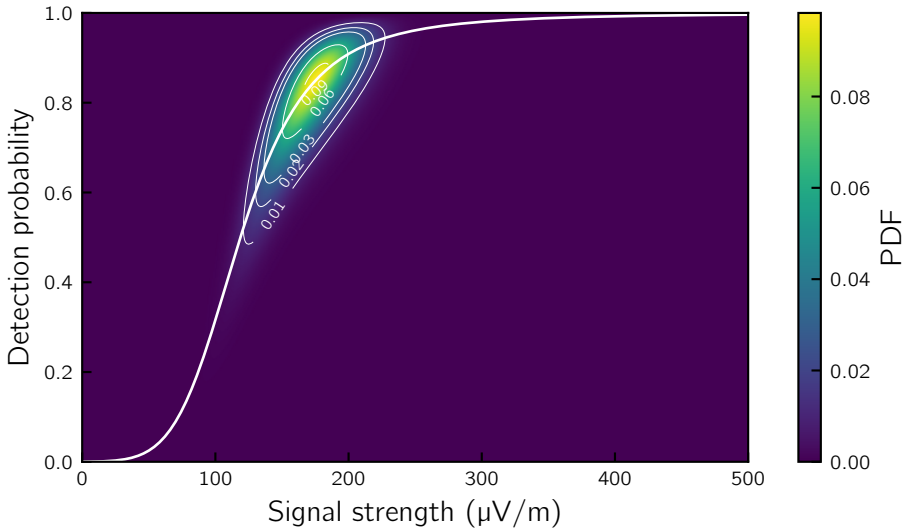

Figure 5.4: The probability density to detect a signal at the antenna location when the LDF model predicts a particular strength of that signal (170 μV/m in this case). The signal strength shown on the plot reflects the range of the strengths which the signal can actually have at the antenna location or, in other words, uncertainty of the description of the radio footprint by the particular LDF model.

The initial uncertainties of all parameters are set to the value 0.01. The final uncertainties of the parameters are found with the intersection of the likelihood function and hyperplane passing 1.0 above the minimum.

Figure 5.3 shows the probability density of the probability to detect a signal. After the extension of the signal detection, its value becomes the mode of the distribution for a given signal strength. The shape of the distribution allows for estimation of uncertainties of the probability to detect a signal with a given strength.

The developed approach provides one more advantage within the framework of the present probabilistic model of the signal detection process. The previous section shows that the spatial distribution of the signals over the instrument has the probabilistic behavior reflected in the uncertainty of the signal strength at a given lateral distance from the shower core. Namely, the strength of the signal at a given distance is a random value with the mean value provided by the lateral distribution function and standard deviations provided by the lateral distribution uncertainties. The distribution of the signals follows the normal law. A combination of the probability density of the signal strength with the probability density of the signal detection probability provide a natural way for uncertainty estimation of the signal detection probability of a shower with a given energy and a depth of shower maximum.

5.2.3. Influence of LDF Uncertainty

As it was shown above in Section 5.1.2 on the spatial distribution of the signals, the lateral distribution function describing the observed signals contains an uncertainty.

Namely, the observed amplitude of the signal can fluctuate around the value predicted by the model. In the statistical language this means that there is a certain probability distribution to observe a signal with a given probability at a given lateral distance from the shower axis. In the framework of the described model, this probability distribution is the normal distribution with the electric-field level predicted by the lateral distribution model as the mean value and 0.1447 of the mean value as the standard deviation (0.1447 is the result of the study presented in Section 5.1.2). Thus, the lateral distribution of the electric field over the antenna array becomes a probability density distribution of the observation of a certain value of the electric field from a shower with a given energy and depth of its maximum. To estimate the probability to detect a signal from such a shower at a given lateral distance from its axis, the probability to observe a certain electric field is merged with the probability to detect a signal of a given strength by an individual antenna. In the mathematical language, this looks as follows. The obtained probability density of detection of a signal with a given strength (5.10) and the probability density of observation of the electric-field value at a given distance from the shower axis $G(S_0, \sigma_S^2)$ are combined as simultaneous events

$$P_t = N \frac{p^{\alpha-1}\,(1-p)^{\beta-1}}{\mathrm{B}(\alpha,\beta)}\, G(S_0, \sigma_S^2). \tag{5.21}$$

The letter N denotes the normalization of the function to the unit probability. This probability density is a two dimensional function of the signal strength and the probability to detect a signal with a given strength. The meaning of this construction is the probability to detect a signal predicted by the LDF model while taking into account the uncertainty of the LDF model prediction of the electric field observed by an individual antenna (see Figure 5.4 for a particular example). The range of the visible signals follows the probability distribution of the signals that can be detected by an antenna in the case of the prediction of a signal coming from the lateral distribution function, in the particularly shown case the signal strength is 170 µV/m. The probability density to obtain that range overlaps with the probability density of the probability to detect a signal with a given strength. The combined probability density function represents the probability density to detect a signal with a given strength for all signals, which can be possibly observed.

The final probability density to detect a signal predicted by the LDF model is represented by an integral over all possible signals within the uncertainties. This integration is accounting for the fact that all the signals within the distribution are possible to observe while the lateral distribution function predicts a given electric field strength for a shower with a certain energy, depth of maximum, and incoming geometry. In the statistical language, such a distribution is a convoluted probability density of the distribution (5.21)

$$P'_t = \int_0^\infty N \frac{p^{\alpha-1}\,(1-p)^{\beta-1}}{\mathrm{B}(\alpha,\beta)}\, G(S_0, \sigma_S)\,\mathrm{d}S. \tag{5.22}$$

Figure 5.5 shows the shape of this distribution for an example signal with a strength of 170 µV/m. Such distributions were obtained for a grid of signal values from 10 µV/m to

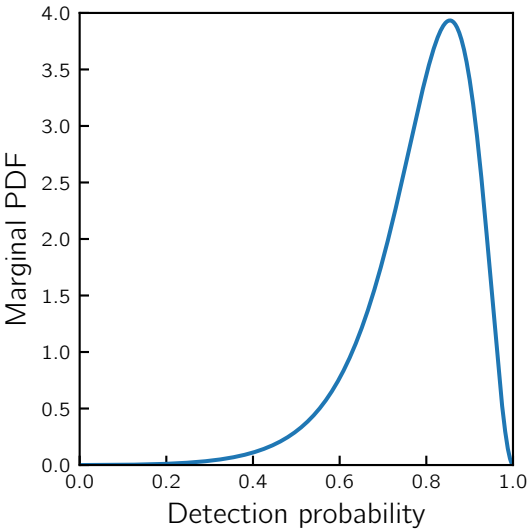

Figure 5.5: Convoluted distribution of the probability density of the probability to detect a signal with a strength of 170 µV/m. The convolution is performed over the signal strength, namely, the plot is an integral over the signal strength of the probability density shown in Figure 5.4. This distribution is a cross-section of the two-dimensional distribution shown in Figure 5.6.

500 µV/m with 10 µV/m step size. A bivariate spline-interpolation of third order over the obtained values is the function used for the further instrument efficiency estimation. To extend the coverage of the interpolation to the zero value of the signal, the corresponding values of the detection probability were zeroed. The interpolation provides a smooth coverage of all possible signals that the LDF model can predict for a shower with given macroscopic parameters. Figure 5.6 shows the overall shape of the interpolation of the calculated values of the convoluted distribution in the discrete values of the signal strength.

The obtained extension of the signal detection probability on the level of a single antenna to the continuous domain and the probability density allow for estimation of not only the probability to detect a given shower based on the predicted signals but also provide the uncertainties of such prediction.

5.3. DETECTION PROBABILITY OF AN ANTENNA ARRAY

The previous level of the model provides a set of probability densities for the probabilities to detect a signal by individual antennas according to the signal strength predicted by the lateral distribution function. The procedure of the detection of air-shower events by an array of antennas is treated probabilistically, in the same way as other components of the developing model.

The idea behind the trigger estimation procedure is to find the probability of the situation when the required trigger condition is fulfilled. What is the trigger condition in the case of the Tunka-Rex as well as many other cosmic-ray radio arrays? It is the number of antennas that detected any signal. Thus, the probability to have at least a certain number of signals in an event becomes the detection probability. There are two approaches to estimate this quantity. The first one is the direct probabilistic calculation of the probability to trigger. Another way of the estimation is using Monte-Carlo experiments with certain realizations of the detection probability.

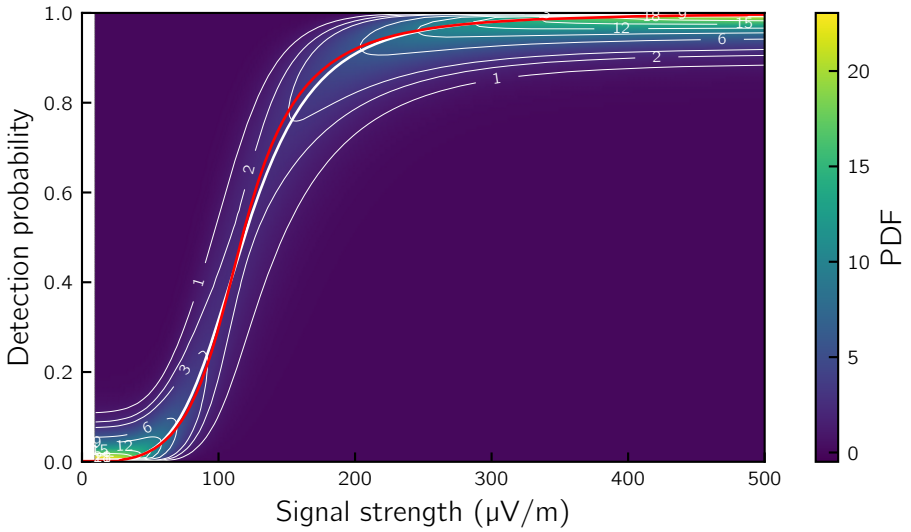

Figure 5.6: The bivariate spline-interpolation of the convoluted probability density of the signal detection estimated for a grid of signals ranging from 0 μV/m to 500 μV/m with a 10 μV/m step. The thick white line shows the most probable value of the convoluted probability density. The red line indicates the position of the most probable value before performing the convolution (the red line on this plot corresponds to the thick white line of the plot on Figure 5.3).

5.3.1. Inference With Probabilistic Calculation

The probability to observe n signals within the array can be estimated as a combination of statistically independent events such as the joint appearance of signals at n antennas of the array and the appearance of no-signals on the remaining antennas. Since it is possible to observe a signal on any of the antennas, we should consider all possible combinations of n antennas out of all N antennas of the array, and sum them up to estimate the probability to observe n signal anywhere in the array. The schematic diagram of this estimation looks as the one in Figure 5.7. Each of the lines shows a possible combination leading to n signals in total. The filled circles represent the antennas with signals. The non-filled circles represent the antennas without signals. The symbols above the circles show the corresponding antenna number. The total number of such combinations is equal to the value of corresponding binomial coefficient $\binom{N}{n}$. The probability to observe a certain combination comes as an estimation of joint probability of independent events which are appearances of signal or non-signal at a given antenna in the combination. The joint probability for a combination depicted as the first (top) line in the diagram is

$$p_1\, p_2\, p_3 \cdots p_{n-1}\, p_n\, \bar{p}_{n+1} \cdots \bar{p}_{N-n}\, \bar{p}_{N-n+1}\, \bar{p}_{N-n+2} \cdots \bar{p}_{N-2}\, \bar{p}_{N-1}\, \bar{p}_N. \tag{5.23}$$

The letters p denote probabilities of observation of a signal. The letters $\bar{p}$ denote the probability of a non-signal, which equals according to the complement rule of the probability axioms to $1 - p$. The indices denote the particular antenna identity number.

Since each of the possible combination is statistically independent and only one of

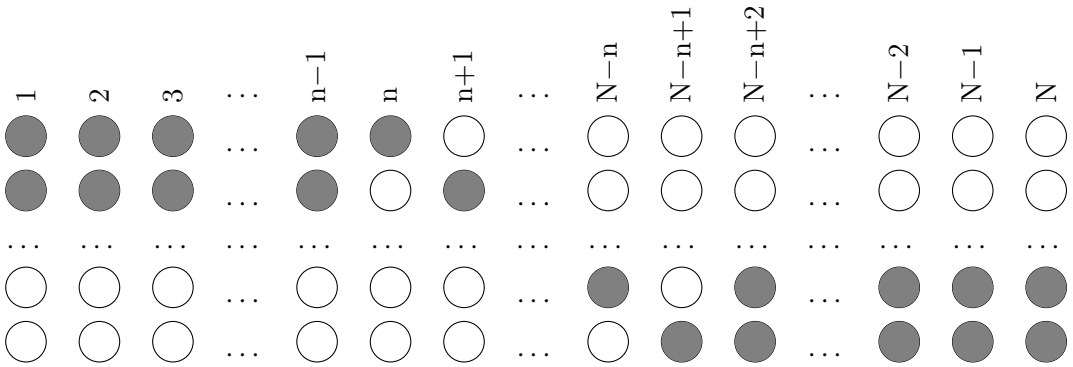

Figure 5.7: Diagram of the possible combinations of appearing signals and non-signals at N antennas while n signals are observed in total at all antennas. Each line of the circles corresponds to a certain configuration. The filled and non-filled circles correspond to the detection of a signal at a given antenna or the non-detection respectively.

those can be an outcome, to estimate the probability to observe n signals at the array, we should consider a sum [3] of the probabilities of all the possible combinations

$$\begin{aligned} p^{(n)} = {} & \bar{p}_1\bar{p}_2\bar{p}_3\cdots\bar{p}_{n-1}\bar{p}_n p_{n+1}\cdots p_{N-n}p_{N-n+1}p_{N-n+2}\cdots p_{N-2}p_{N-1}p_N + \\ & \bar{p}_1\bar{p}_2\bar{p}_3\cdots\bar{p}_{n-1}p_n\bar{p}_{n+1}\cdots p_{N-n}p_{N-n+1}p_{N-n+2}\cdots p_{N-2}p_{N-1}p_N + \\ & \qquad\qquad\qquad\qquad\qquad\qquad\qquad\qquad\qquad\qquad\qquad\qquad\qquad\qquad \cdots \quad , \\ & p_1p_2p_3\cdots p_{n-1}p_np_{n+1}\cdots\bar{p}_{N-n}p_{N-n+1}\bar{p}_{N-n+2}\cdots\bar{p}_{N-2}\bar{p}_{N-1}\bar{p}_N + \\ & p_1p_2p_3\cdots p_{n-1}p_np_{n+1}\cdots p_{N-n}\bar{p}_{N-n+1}\bar{p}_{N-n+2}\cdots\bar{p}_{N-2}\bar{p}_{N-1}\bar{p}_N \end{aligned} \tag{5.24}$$

or shortly

$$p^{(n)} = \sum_{i=1}^{\binom{N}{n}} p_i^{(n)}. \tag{5.25}$$

The combined probability of all possible situations leading to observation of number of signals greater than the required number forms the probability of appearance of the trigger. If we assume that m is the minimum number of antennas required as a trigger condition, the trigger probability in this case equals to

$$P = \sum_{i=1}^{\binom{N}{m}} p_i^{(m)} + \sum_{i=1}^{\binom{N}{m+1}} p_i^{(m+1)} + \cdots + \sum_{i=1}^{\binom{N}{N-1}} p_i^{(N-1)} + \sum_{i=1}^{\binom{N}{N}} p_i^{(N)}. \tag{5.26}$$

This equation is correct but not practical. The issue with this approach is that the number of algebraic operations is unacceptably large. For instance, if we calculate the number of all possible combinations of the antennas with- and without signals for the

[3] The probability sum rule reads $P(A+B) = P(A) + P(B) - P(A \cap B)$ [241]. However, since the considered subsets are complement, we can neglect the last term without changing the results of the calculation, as the probability to observe some combinations where an antenna detected and not-detected a signal at the same time is zero.

case of Tunka-Rex, with 63 antennas in total, and Tunka-Rex trigger condition of at least three antennas with signals, we obtain 9,223,372,036,854,773,791 possible combinations. After observing this number it is clear that we should use another way to calculate the probability.

Another way for estimation of the trigger probability is to compute all the cases not leading to generating the trigger and then use the complement rule. It is clear that number of combinations is much more modest in this case. For the case of Tunka-Rex, 63 antennas and at least three antennas with signals as a trigger condition, we obtain 2017 possible combinations to work with.

Thus, the more computationally efficient variant of the estimation the trigger probability looks as following

$$P = 1 - \left(\sum_{i=1}^{\binom{N}{0}} p_i^{(0)} + \sum_{i=1}^{\binom{N}{1}} p_i^{(1)} + \sum_{i=1}^{\binom{N}{2}} p_i^{(2)} + \cdots + \sum_{i=1}^{\binom{N}{m-1}} p_i^{(m-1)} \right). \tag{5.27}$$

A pivoting point in the trigger probability estimation comes from the fact that the probabilities to detect a given signal by an antenna, which were in all formulas above, are not numbers but probability density functions. The main consequence of this is that the algebraic operations, i.e., summation, multiplication, differ from those for real numbers.

For completeness of the picture, let us revise the formulas for the algebraic operations with random variables [241, 242]. If there are two random variables ξ_1 and ξ_2 described with corresponding probability densities f_{ξ_1} and f_{ξ_2}, the sum of the two variables $\xi_1 + \xi_2$ has the probability density

$$f_{\xi_1+\xi_2}(x) = \int_{-\infty}^{+\infty} f_{\xi_1}(x-y) f_{\xi_2}(y)\,\mathrm{d}y, \tag{5.28}$$

which matches up with the convolution of these two probability densities.

To obtain the probability density of the product $\xi_1\xi_2$, the formula is

$$f_{\xi_1\xi_2}(x) = \int_a^b f_{\xi_1}(t) f_{\xi_2}\left(\frac{x}{t}\right) \frac{\mathrm{d}t}{|t|}. \tag{5.29}$$

The limits a and b need to be chosen according to the domain of specific functions. A detailed discussion on the choosing of appropriate integration limits is given in [242]. For the present study the limits are $a = x$ and $b = 1$.

An additional component required for the estimation of the instrumental efficiency is the way to estimate the probability of the random variable $(1 - p)$, which is in fact itself a function of a random variable. To obtain the formula for this case, we consider a procedure of variable substitution of the random variable in the probability density function. If a random variable ξ has the probability density function $f_\xi(x)$, a function $y = g(x)$ of the random variable has the following probability density

$$f_Y(y) = \frac{f_X\left(g^{-1}(y)\right)}{\left|\frac{\mathrm{d}}{\mathrm{d}y} g^{-1}(y)\right|}, \tag{5.30}$$

where g^{-1} denotes the inverse function of g. For the particular case of this study this looks as follows. The probability p corresponds to x, and the new variable p' corresponds to y. The new variable is introduced with the equation $p' = 1 - p$, which corresponds to the function g in the generic form described above. After all transformations the probability density distribution for the variable p' becomes

$$\tilde{P}'_t = P'_t(1 - p), \tag{5.31}$$

which means that we use the same function but only change the variable p to $1 - p$.

For the purposes of the present study, using formulas (5.28) and (5.29) directly possible, but only for very small number of the antennas required for the detection condition, which makes it unfeasible for large-scale cases.

Instead, we use the method of sampling of the individual probability densities. The samples are certain realizations from the range of possible values of the signal detection probability on the level of the individual antennas. After taking one sample value from all of the probability densities, we use the equations (5.24), (5.25), and (5.27) as for real numbers leading to a certain realization of the probability to fulfill the trigger condition. The repetition of the procedure by continuing to sample the probability densities maps the density of trigger probability. The left plot in Figure 5.8 shows the probability density of trigger realizations as a histogram. For this method the size of the sample is 10^3. This number can be increased leading to a better mapping of the functions, however, it was observed that an increase for an order of magnitude or even more does not bring significant changes to the final results.

The final part in the estimation of the probability density of fulfilling the trigger conditions is to infer the shape of the density function from the obtained sample. The underlying distribution is of unknown type. Thus, to avoid introducing additional uncertainties, we use a non-parametric method to infer the shape of the probability density, namely, kernel density estimation with a Gaussian kernel. The method of the kernel density estimation uses the following formula as the density estimator [243]

$$\hat{f}(x) = \frac{1}{n} \sum_{i=1}^{n} K_h(x - x_i). \tag{5.32}$$

The letter K_h denotes the kernel with the bandwidth h, the letter x_i denotes a certain point from the sample, and the letter n denotes the size of the sample. The kernel in the present work is the Gaussian kernel, i.e., the normalized Gaussian distribution with the standard deviation equal to the bandwidth. The selection of the bandwidth is the crucial part for the density estimation procedure. For this procedure we use the classical choice of the bandwidth based on the sample estimation of the standard deviation $\hat{\sigma}$ multiplied with the so-called Scott's factor, which is for a one dimensional case equal to

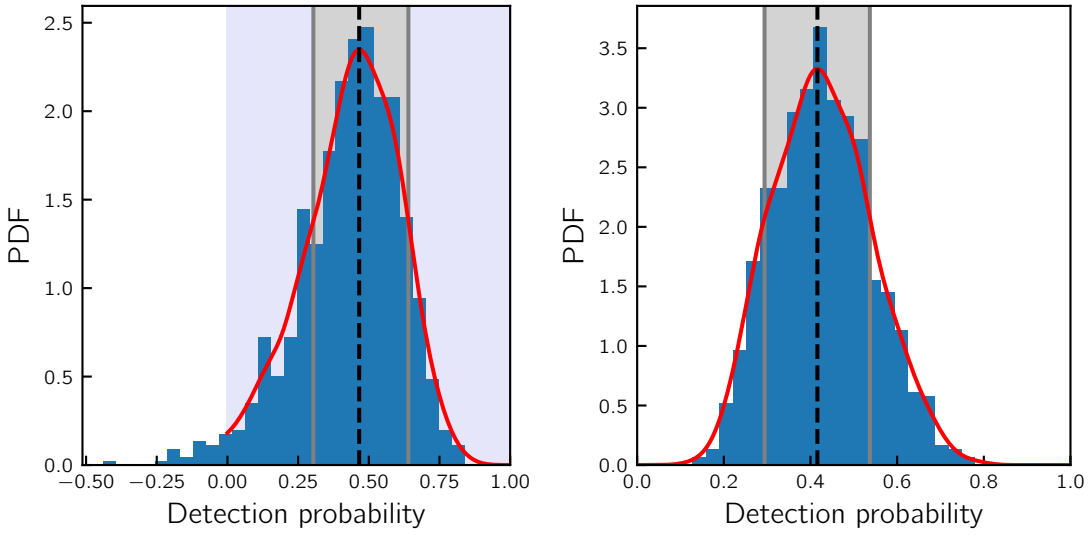

Figure 5.8: Estimation of the probability density function (PDF) for a particular shower taken as example. The data are presented in the two forms: histogram and kernel density estimator. The histogram is normalized to the total number of entries; its binning is obtained with the Freedman Diaconis Estimator. The red curve represents the results of the Gaussian kernel density estimation with the bandwidth of $1.06\,\hat{\sigma}\,n^{1/5}$. The shower core is in the origin of the coordinates, the other shower parameters are $\theta = 30°$, $\phi = 270°$, $\log_{10}(E/1\text{eV})$=17.3, $X_{\max} = 658$ g/cm^2. The vertical dashed black line shows the detection probability, which is the mode of the probability density estimated with the Gaussian kernel; the gray band shows the uncertainty of detection probability and encloses 0.68 of the total region under the probability density. The trigger condition used for this case is having at least three antennas with signals over the 63 Tunka-Rex antennas. *Left*: the estimation obtained with the probabilistic calculations, $0.466^{+0.174}_{-0.162}$; the lavender color marks the physical region of the function domain. *Right*: the estimation obtained with the Monte-Carlo experiments, $0.416^{+0.121}_{-0.122}$ (see Section 5.3.2 for details).

$1.06\,n^{-1/5}$. Thus, the kernel density estimator used in this work has the following form [4]

$$\hat{f}(x) = \frac{1}{n}\sum_{i=1}^{n} G(x - x_i, 1.06\,\hat{\sigma}\,n^{1/5}). \tag{5.33}$$

The density obtained by this method is the estimator for the probability density function of the trigger fulfillment for a given shower. The mode of this function is the estimator for the detection probability. The uncertainty of the detection probability is defined as the width of the region of the function containing 68% of the whole function. The region is selected such that the ordinates of the borders are equal.

The method developed above already comprises an important tool for estimating the detection efficiency of the Tunka-Rex instrument, however, the internal design of the

[4]The notation $G(\mu, \sigma)$ refers to a normalized Gaussian distribution with the mean μ and the standard deviation σ and is used here for conciseness.

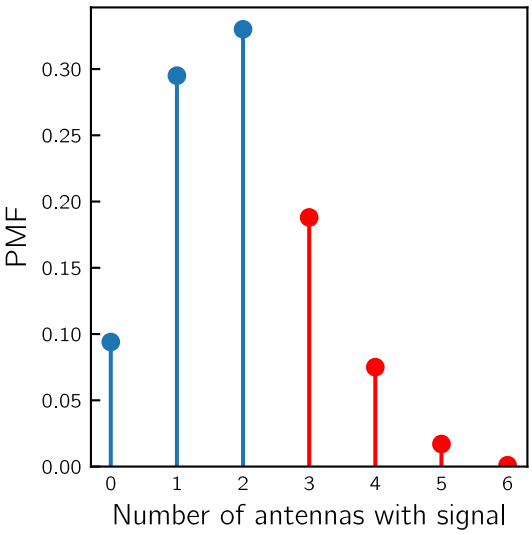

Figure 5.9: Estimation of the probability mass function (PMF) for a single event for a single realization of the signal-detection probabilities on the level of individual antennas. The values marked in red are summed up to obtain an estimation of the trigger fulfillment probability. For this particular case the trigger condition is having at least three antennas with signals over the entire antenna array. The macroparameters of the shower are the same as for Figure 5.8.

method does not allow for scaling it up to the level of a realistic number of antennas in the event. The number of antenna combinations required for estimation rapidly increases with increasing amount of antennas required to have a signal to fulfill the trigger condition. This is reflected in a rapid increase of the computation time making the computation not feasible for certain trigger configurations. The method described in the following section was developed to overcome this issue.

5.3.2. Inference With Monte-Carlo Experiments

Another method for the estimation of the trigger fulfillment probability can be established in addition to those described above. The idea of the method is an extension of the existing method of the Monte-Carlo experiments for assessment of the trigger probability from the known signal detection probabilities for individual detectors of an array [244]. The original idea is as follows. Some procedure defines probabilities to detect signals with individual detectors of an array. Then a series of Monte-Carlo experiments is carried out. Each of the experiment runs a single Bernoulli trial on every of the detectors, and assesses whether the trigger condition is fulfilled. As a result, the fraction of the experiments which fulfilled the trigger condition determines the probability to detect the given shower. This idea is extended in the present study.

The original method assumes that the probability to detect signal with the individual detector is a real number. The present work treats these probabilities as probabilistic quantities characterized with probability density functions. The extension of the original idea consists in performing series of Monte-Carlo experiments for a sample of possible realizations of the signal-detection probabilities drawn from the corresponding probability density functions.

The organization of the estimation procedure is the following. First, we draw a single sample value from each of the probability density functions. This set of single values, one for each antenna over the field, is used in Monte-Carlo experiments. Each

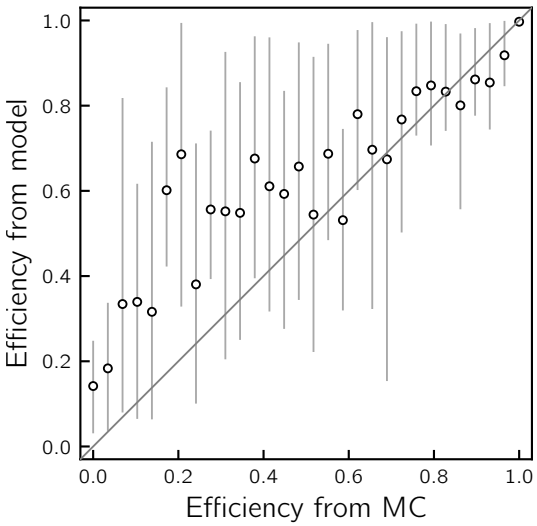

Figure 5.10: The comparison of the detection probability estimated with the model against the detection probability estimated with the multiple processing of the Monte-Carlo signals with different noise samples.

experiment consists of a single Bernoulli trial for each of the antennas. The result of each of the experiments is the amount of antennas with signals. The set of the Monte-Carlo experiments estimates the probability mass function of the amount of the antennas with signal. Figure 5.9 shows an example of such a function. Summing all of the values of this function satisfying a trigger condition provides an estimation to the probability of the trigger fulfillment. Then the next sample from the probability density function is drawn, and the procedure repeats.

The obtained samples are the entry data for estimation of the probability density function of the trigger fulfillment. For this purpose, the same procedure of the kernel density estimation is used described in the previous section. The mode of the obtained density function is the final estimation of the trigger probability. The right plot on Figure 5.8 shows the result of the estimation.

5.4. VALIDATION OF EFFICIENCY MODEL

The key to understanding the correctness of the built efficiency model is its validation both against Monte-Carlo simulations and the observational data. The last is possible only because of the unique configuration of the Tunka-Rex instrument. The instrument providing the trigger is a highly accurate Cherenkov instrument, Tunka-133, with the energy threshold orders of magnitude lower than those of Tunka-Rex. This configuration allows for a direct comparison of the events in both instruments.

5.4.1. Validation against Monte-Carlo simulations

The comparison of the model prediction against the Monte-Carlo simulation is relatively straightforward. To perform this comparison, the simulated events were analyzed multiple times with different noise samples. The fraction of events which fulfilled the trigger condition is the Monte-Carlo estimation for the detection probability. This estimation is discrete since the events were analyzed a finite number of times, 30 in this work,

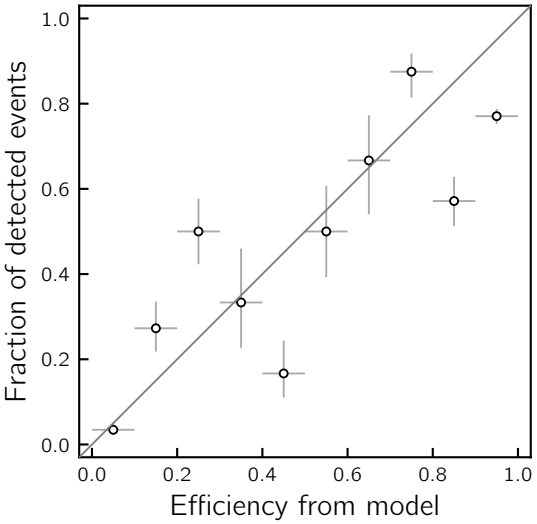

Figure 5.11: Comparison of the detection probability estimated with the model against the fraction of the events seen by the Tunka-Rex array. The fraction of the detected events can be treated as the estimation of the detection probability with the observational data.

which gives 30 possible values of the probability. The events with the same value of the detection probability were grouped for further analysis of the model prediction of the detection probability within each of the groups. For each of the events within each of the groups the detection efficiency was estimated with the developed efficiency model. Figure 5.10 shows the mean values and the uncertainty band for the events with the same Monte-Carlo detection probability. The uncertainties are the range between the 16% and 84% percentiles. The trigger condition used in this comparison is fulfilled when there are at least three antennas which detected signals over the array.

The comparison of the two estimations of the air-shower detection efficiency reveals few important aspects of the developed efficiency model. The first one is the presence of the overall linear behavior. The second one is the significant uncertainties for the middle range of probabilities. Such wide uncertainties reflect the large influence of noise in this region. The last aspect is important for the practical application of the model. Despite the presence of the wide uncertainties in the middle range, the model describes well the regions with high and low detection probability. This means that even though the model does not describe fine details of the detection transition region from unity to zero, the model provides the correct estimation of the full-efficiency region. The particular value of probability defining the full efficiency can vary. However, it is clear that all values above 0.8 provide an accurate description.

5.4.2. Validation against the Tunka-133 measurements

Another method of validation of the developed model is the comparison of its predictions against the measurements performed with Tunka-133. Since Tunka-133, which triggers the Tunka-Rex array, has its own air-shower reconstruction procedure and features a low energy threshold in comparison to Tunka-Rex, the Tunka-133 measurements can be used for in-situ validation of the efficiency model.

To validate the model against the Tunka-133 observational data, the prediction of the

model was compared to the observed probability of detection. To estimate the observed probability, all the events seen by Tunka-133 were grouped according to the model predicted probability to detect them with the Tunka-Rex array. Within each group, the fraction of the events which fulfilled the trigger condition was treated as the observed detection efficiency. The condition used here was to have at least three antennas with signals over the antenna array.

The Tunka-Rex measured events were prepared in a specific way for this comparison. Namely, the data processing was done only up to the end of the signal processing procedure. Thus, not including any lateral distribution symmetrization or fitting, and further steps. This procedure naturally excludes the influence of the reconstruction efficiency from the comparison.

Figure 5.11 shows the result of the comparison. The data for this comparison were limited to the energies above $10^{17.3}$ eV of the cosmic-ray energy. The result reveals that the overall prediction of the model matches the observed detection probability.

5.5. CONCLUDING REMARKS

The model developed in this chapter exploits an explicit probabilistic approach to the problem of the efficiency estimation of a radio array. As it was seen throughout the chapter, such an approach allows for a physically transparent modeling in which the relationships between its various parts are clearly visible, as well as their influence on the final result. Moreover, this approach enables the transparent estimation of the uncertainties of the final result.

The present work develops this model for Tunka-Rex as example. It is clear that the model itself has a generic nature and can be used for any other radio array or even non-radio instruments.

The next chapter presents a particular application of the developed efficiency model to an unbiased reconstruction of the cosmic-ray energy spectrum with the Tunka-Rex air-shower data.

CHAPTER SIX

APPLICATION OF THE EFFICIENCY MODEL

The efficiency model developed in the previous chapter has a generic nature and potentially can be used for a wide range of air-shower radio arrays to predict their performance for the detection of cosmic rays with specific macroparameters like energy and $X_{\max}$. This chapter presents a particular application of the developed model to a reconstruction of the cosmic-ray energy spectrum with the Tunka-Rex data. The reconstruction provides a so-called raw spectrum, the spectrum without unfolding the effects of the instrument resolution on the measurements.

The chapter is organized in the following way. The first section describes necessary mathematical details on the number of the observed events and its connection to the cosmic-ray energy spectrum via the aperture of the instrument and observation time. The following sections describe the details of estimation of the aperture and observation time. All the components are merged together in the last section devoted to estimation of the raw spectrum of cosmic rays with the Tunka-Rex data.

6.1. DEFINITION OF APERTURE

The estimation of the energy spectrum of cosmic rays is closely related to the concept of aperture, which is an integral representation of the array efficiency of the cosmic-ray detection. Let us consider the mathematical details of the aperture related to the estimation of the cosmic-ray energy spectrum with a flat instrument as Tunka-Rex.

In a general case, the event rate $\mathrm{d}N/\mathrm{d}E$ observed by a cosmic-ray instrument is proportional to the cosmic-ray flux J via the factor ϵ denoting the "exposure" of the measurement

$$\frac{\mathrm{d}N}{\mathrm{d}E} = \epsilon\, J. \tag{6.1}$$

Exposure quantitatively expresses the instrument ability to detect cosmic rays with certain properties, e.g., energy, depth of the shower maximum, incoming direction, etc. For the sake of completeness, let us consider a derivation of this equation.

Cosmic rays come to the Earth nearly isotropically. The instant number of events seen by a generic volumetric instrument from a given direction on the sky $\boldsymbol{m}$ passing an infinitesimal oriented area on the surface surrounding the instrument $d\boldsymbol{s}$ is the projection of this area to the direction $\boldsymbol{m}$ multiplied to the cosmic-ray flux

$$\frac{\mathrm{d}N}{\mathrm{d}E\mathrm{d}t\,\mathrm{d}o} = \xi J\, \boldsymbol{m} \cdot \mathrm{d}\boldsymbol{s}. \tag{6.2}$$

The projection represents the area visible from the incoming direction of the cosmic rays. The letter ξ denotes the instrumental efficiency, a quantitative expression of the ability of the instrument to observe the cosmic rays with certain properties. The differential $d\boldsymbol{o} = \boldsymbol{m}\, do$ is the infinitesimal solid angle of the sky corresponding to the considered direction. The bold symbol of the infinitesimal instrument area means that it contains the normal to the surface $d\boldsymbol{s} = \boldsymbol{n}\, ds$. The normal points outwards from the instrument.

The event rate is an integral of the instant event number over the total convex area of the instrument, S, the whole area of the sky, Ω, and the observation duration, T:

$$\frac{\mathrm{d}N}{\mathrm{d}E} = J \int_T \int_\Omega \int_S \xi \, \mathrm{d}\boldsymbol{o} \cdot \mathrm{d}\boldsymbol{s} \, \mathrm{d}t. \tag{6.3}$$

The integral on the right hand side of (6.3) is a generic form of the instrumental exposure

$$\epsilon = \int_T \int_\Omega \int_S \xi \, \mathrm{d}\boldsymbol{o} \cdot \mathrm{d}\boldsymbol{s} \, \mathrm{d}t. \tag{6.4}$$

To take into account the fact that the instrument counts only events coming from outside, we require an additional constrain

$$\xi = \begin{cases} \xi, & \text{if } \mathrm{d}\boldsymbol{o} \cdot \mathrm{d}\boldsymbol{s} \geq 0 \\ 0, & \text{otherwise} \end{cases} \tag{6.5}$$

In case of a flat instrument, the generic form of the exposure (6.4) can be simplified to

$$\epsilon = \int_T \int_\Omega \int_S \xi \ \cos\theta \, \mathrm{d}s \, \mathrm{d}o \, \mathrm{d}t. \tag{6.6}$$

The letter θ denotes the zenith angle of air-shower incoming direction. The cosine factor appears from the explicit expression of the dot product.

The efficiency is a multi-variable function depending on spatial and angular coordinates, cosmic-ray energy, and shower macro-parameters, e.g., $X_{\max}$. If due to some reason the configuration of the instrument changes with time, the efficiency becomes a function of time as well.

The definition of the exposure in (6.4) contains the essence of this quantity. Some Monte Carlo procedures use this equation as a foundation (Reference [245] presents a specific example of such approach). However, in the framework of this work, we split this equation into smaller components with defined meanings.

Following the general practice [245], we refer to the integral of the efficiency in (6.4) over the spatial and angular coordinates as "aperture"

$$A = \int_\Omega \int_S \xi \ \cos\theta \, \mathrm{d}s \, \mathrm{d}o. \tag{6.7}$$

This quantity reflects the ability of the instrument to detect cosmic-ray air showers with certain properties.

The efficiency of the instrument depends on multiple factors. However, the main factors that directly affect the instrument detection efficiency are the operation stability of its individual components and their up-time during the observations. Unstable

instrument operation leads to additional complexities in the aperture and exposure estimation, which affect the accuracy of the final measurements. In such a case of unstable instrument operation, the aperture becomes a function of time $A = A(t)$. It is possible to overcome this time-varying aperture issue by splitting the full operation time into smaller periods within which the instrumental configuration, meaning efficiency, does not change. This splitting allows for a factorization of the exposure within each of the periods into an aperture and an observation time

$$\epsilon = \int_T \int_\Omega \int_S \xi \ \cos\theta \, \mathrm{d}s \, \mathrm{d}o \, \mathrm{d}t = \int_T A \, \mathrm{d}t = A\,T. \tag{6.8}$$

The exposure over the full observation time becomes a sum of the estimations for the selected time periods

$$\epsilon = \sum_i A_i \, T_i. \tag{6.9}$$

This sum is essentially a result of an integration of the piece-wise constant efficiency.

The usually used methods of the air-shower parameter reconstruction implies a certain spatial and angular fiducial selection of events. Utilization of this approach transforms the integral limits in (6.7) to those corresponding to the fiducial selection in the data analysis

$$\int_\Omega \int_S \xi \ \cos\theta \, \mathrm{d}s \, \mathrm{d}o \to \int_{\Omega_\mathrm{f}} \int_{S_\mathrm{f}} \xi \ \cos\theta \, \mathrm{d}s \, \mathrm{d}o. \tag{6.10}$$

The index "f" stands here for "fiducial". The approach of fiducial selection allows for additional simplification of the formulas. We can factorize out a constant area of the spatial fiducial selection from the integral.

$$\begin{aligned} \int_{\Omega_\mathrm{f}} \int_{S_\mathrm{f}} \xi \ \cos\theta \, \mathrm{d}s \, \mathrm{d}o = S_\mathrm{f} \int_{\Omega_\mathrm{f}} \int_{S_\mathrm{f}} \frac{\xi}{S_\mathrm{f}} \ \cos\theta \, \mathrm{d}s \, \mathrm{d}o = \\ S_\mathrm{f} \int_{\Omega_\mathrm{f}} \left(\frac{1}{S_\mathrm{f}} \int_{S_\mathrm{f}} \xi \, \mathrm{d}s \right) \ \cos\theta \, \mathrm{d}o = S_\mathrm{f} \int_{\Omega_\mathrm{f}} \langle \xi \rangle_s \ \cos\theta \, \mathrm{d}o. \end{aligned} \tag{6.11}$$

The symbol $\langle \xi \rangle_s$ denotes the averaged efficiency over the fiducial area. The last integral we will refer to as "angular aperture"[1]

$$A_\Omega = \int_{\Omega_\mathrm{f}} \langle \xi \rangle_s \ \cos\theta \, \mathrm{d}o. \tag{6.12}$$

[1]In the same fashion we could factorize aperture into solid angle of the fiducial angular selection and averaged efficiency over this angle

$$\begin{aligned} \int_{\Omega_\mathrm{f}} \int_{S_\mathrm{f}} \xi \ \cos\theta \, \mathrm{d}s \, \mathrm{d}o = \Omega_\mathrm{f} \int_{\Omega_\mathrm{f}} \int_{S_\mathrm{f}} \frac{\xi}{\Omega_\mathrm{f}} \ \cos\theta \, \mathrm{d}s \, \mathrm{d}o = \\ \Omega_\mathrm{f} \int_{S_\mathrm{f}} \left(\frac{1}{\Omega_\mathrm{f}} \int_{\Omega_\mathrm{f}} \xi \ \cos\theta \, \mathrm{d}o \right) \mathrm{d}s = \Omega_\mathrm{f} \int_{S_\mathrm{f}} \langle \xi \rangle_\Omega \, \mathrm{d}s. \end{aligned}$$

Even though this approach can have advantages in some cosmic-ray analyses since it preserves the angular coverage of the instrument in case of the selection of full-efficiency regions, it is out of the scope of the present work.

Thus, collecting together the introduced quantities gives a factorized mathematical form for estimating the cosmic-ray instrument exposure

$$\epsilon = S_{\mathrm{f}}\, A_{\Omega}\, T, \tag{6.13}$$

which leads to the final form of the event rate observed by a flat cosmic-ray instrument as Tunka-Rex

$$\frac{\mathrm{d}N}{\mathrm{d}E} = S_{\mathrm{f}}\, A_{\Omega}\, T\, J. \tag{6.14}$$

The last step is to estimate the event rate since it is not a direct observable for an instrument. Because of the counting character of the cosmic ray observations the event rate can be approximated by a ratio of the events observed in i-th energy bin, N_i, over the width of this bin ΔE_i. With this approximation and after rearranging the equation, the estimation of the differential flux at the energy E_i can be done as follows

$$J(E_i) = \frac{1}{S_{\mathrm{f}}\, A_{\Omega}(E_i)\, T} \frac{N_i}{\Delta E_i}. \tag{6.15}$$

As it can be seen from this formula, the only relevant dependence on energy comes from the angular aperture reflecting the energy-dependent efficiency suppressed region in the sky.

6.2. ESTIMATION OF APERTURE

This section describes how from the level of the efficiency model we, first, estimate a sky region corresponding to the full efficiency regime, and, then, compute the aperture for it in a semi-analytical manner.

6.2.1. Sky Map of Averaged Efficiency

According to the formalism of the present work, the detection efficiency averaged over the instrument fiducial area is the main component of the aperture integral (see (6.12)). The averaged efficiency is obtained by averaging the probability densities of the showers with different core positions distributed over the fiducial area of the array. For the present work the simple square grid was used to locate the cores within the fiducial area. The method for averaging is the same as used above for the inference of the trigger probability since the estimation for any core position results in a certain probability density function (Section 5.3). Running the calculations for a range of azimuthal and zenith angles provide the estimation of the average efficiency as a function of the incoming direction. Figure 6.1 shows the results of the calculations for a given shower while varying its core position and the averaged efficiency for a shower with given energy and depth of the shower maximum. The varying of the core position reveals that the detection efficiency does not drop homogeneously over the entire array. Even for not optimal incoming directions there exists regions of the core positions with quite high detection efficiency.

The averaged detection efficiency behavior reveals the known effect of the efficiency suppression towards the local geomagnetic field direction. It is noticeable that the shape

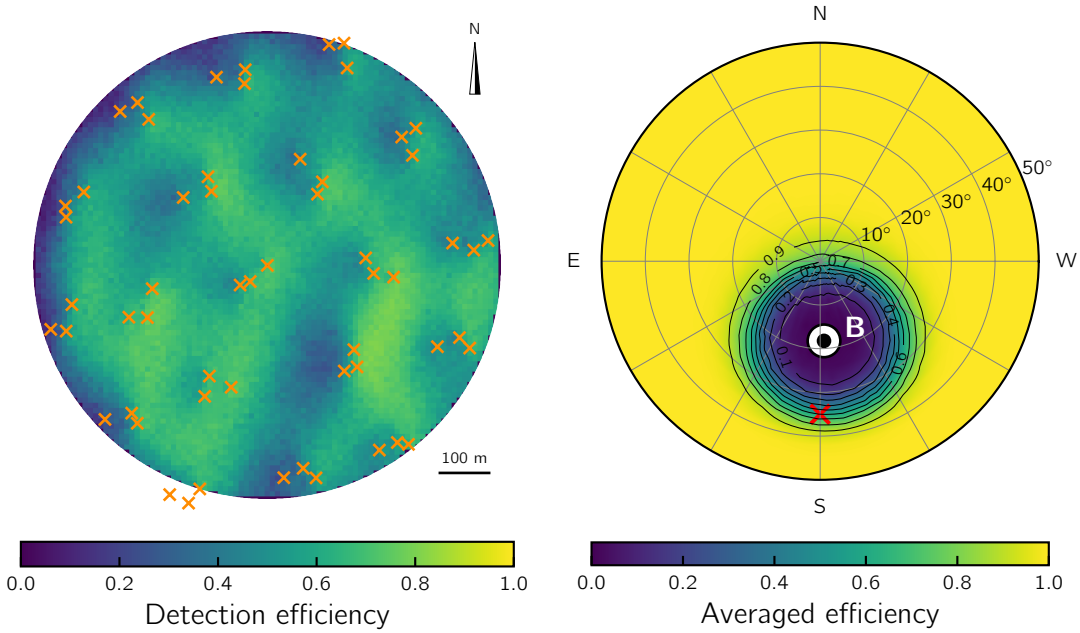

Figure 6.1: The efficiency of Tunka-Rex according to the model developed in this work (for details see Chapter 5). *Left*: the detection efficiency as function of the core position. The shower has a given energy, depth of the shower maximum, and incoming direction ($10^{17.3}$ eV, 650 g/cm^2, θ=35°, ϕ=270°). The arrow in the upper right corner points towards the geographic north. The circular area is the fiducial area of the Tunka-Rex instrument; crosses indicate antenna positions. It is centered at the first antenna position and has a fixed radius of 450 m. *Right*: the detection efficiency averaged over the fiducial area as a function of the incoming direction for $E = 10^{17.3}$ eV and $X_{\max} =$ 650 g/cm^2. The averaging is done over the fiducial area of the Tunka-Rex instrument. The black-and-white circle shows the position of the local geomagnetic field. The red cross marker shows the incoming direction corresponding to the efficiency function on the left plot.

of the suppressed region is approximately circular, which is surprising taking into account the complexity of the shower footprint geometry and complexity of the detection process.

To produce the sky map of the averaged efficiency, the Gaussian grid over azimuthal and zenith angle provides the directions for the calculations. The interpolation between the sample points is done with linear splines.

6.2.2. Selection of The Full-Efficiency Region

To avoid a bias in the cosmic-ray observations, it is of crucial importance to select the region of the incoming directions where the instrument is fully efficient. This selection eliminates possible biases in the resulting measurements of the energy spectrum and mass composition due to not efficient detection of showers with some energies or depth of the shower maximum coming from certain directions.

The visual investigation of the averaged efficiency over a range of incoming directions reveals (Figure 6.1) the circular shape of the efficiency suppression region around the local geomagnetic field direction. Thus, this region is approximated with a circle for further exclusion from the aperture estimation.

A circle on the surface of a unit sphere centered at the zenith angle θ_0 and with the radius of ρ has the following parametric form

$$\cos\rho = \cos\theta\cos\theta_0 + \sin\theta\sin\theta_0\cos\phi. \tag{6.16}$$

θ and ϕ have the usual meaning of the zenith and azimuth. The circle center lies on the zero azimuth. If some rotation is necessary, it can be done with a simple linear shift of the azimuthal coordinate.

The circular region approximates the position of the efficiency suppressed region. To achieve this, the center lies on the azimuth running through the local geomagnetic field direction, the line going from the zenith through the local geomagnetic field direction down to the horizon. This selection of the center location is driven by the phenomenology of the radio emission. Namely, due to the fact that the main contribution to the radiation, in the frequency band used by Tunka-Rex, comes from the geomagnetic deflection of charges by the Lorentz force.

The center and radius of the circular region is found in a nested minimization procedure. The goal of the optimization is to find the position of the circle for which the radius is minimal. The radius is set in a way that the minimal value of the efficiency around the circle equals to a given value of the detection probability. This definition of the radius of the circle encloses the region with efficiency lower than the given value. Thus, the procedure has the following structure. The internal optimization finds the radius for a fixed center. The external procedure looks for the optimal center location corresponding to the minimal radius. Figure 6.2 shows the result of the minimization. The circular region with the minimal radius encloses the region with the averaged efficiency lower than 98%, which is the selected boarder of the full efficiency region.

It is clear from the phenomenology of the radio emission that the size of the full efficiency region changes with energy and depth of the shower maximum. This variation was estimated in the framework of the developed model of the detection efficiency.

The variation of the suppressed efficiency region size and its position was first checked for various depth of shower maximum while keeping the energy unchanged. Figure 6.2 reveals the obtained values. One can appreciate how little the change of the full-efficiency region is over the almost full range of $X_{\max}$ corresponding to the presented energy. The range covers about 98% of the possible values. This finding provides a possibility to evaluate the efficiency suppressed region using a single reference value of the shower maximum depth. Further studies can refine this approach, however, for the present work it seems optimal.

An additional aspect pronounced on the right plot in Figure 6.2 is the difference between behavior of the full-efficiency region, 98% efficiency, and the regions approxi-

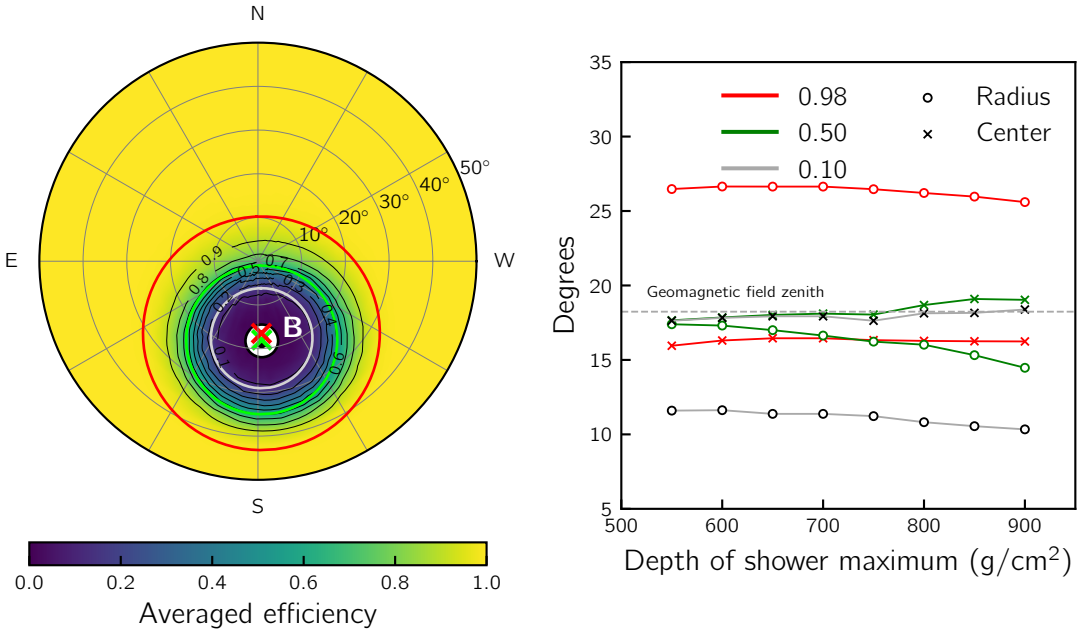

Figure 6.2: Angular behavior of the averaged efficiency for air showers with the depth of maximum of 650 g/cm^2 and produced by $10^{17.3}$ eV cosmic rays. *Left*: the distribution of the averaged efficiency over the sky. The red, green, and gray circles correspond to the 0.98, 0.5, and 0.1 maximal efficiency regions. *Right*: the evolution of the radii and center positions of the circles corresponding to the 0.98, 0.50, and 0.1 maximal efficiency regions. The size of the 0.98 efficiency circle is almost independent of $X_{\max}$.

mating half-efficient and low-efficiency regions, 50% and 10% correspondingly. The low-efficiency region remains almost unchanged similar to the full-efficiency region but the half-efficiency region significantly shrinks while the shower maximum depth approaches the observer. While the reason for the unchanging sizes of the full- and low-efficiency regions remains unclear, the shrinking of the half-efficient region can be understood from a simple phenomenological picture. While approaching the observer, the shower appears brighter, which makes it easier to detect. However, the detailed investigation of the region of transition from high to low efficiency is the subject for further studies.

6.2.3. Evaluation of Aperture Integral

After building the detection efficiency model and finding a reasonable way to select the region of the full efficiency, the remaining component to the estimation of the aperture is the evaluation of the aperture integral shown in (6.12). This integral is a two dimensional integral over a function on the surface of the unit sphere. The numerical solution of such integrals remain fairly complicated due to the fact that this integration is connected to the unsolved pure mathematical problem of a homogeneous distribution of point over the surface of the unit sphere. Thus, it was found that a more reasonable approach is to find a semi-analytical solution.

The semi-analytical solution found in this work splits the solution into two components. The first one is the solution of the integral over the entire sky up to a certain zenith angle. The second one is the solution of the integral over the circular approximation of the efficiency suppressed region. The subtraction of the second component from the first one provides the final solution, which is the estimation of the aperture for the full efficiency region. As it will be seen below, the solution is a combination of a constant and a one-dimensional integral. This dimensional reduction allows for using one-dimensional numerical-integration methods, which are highly accurate.

Let us begin with writing the aperture integral (6.12) explicitly in the spherical coordinate system

$$A_\Omega = \int_{\Omega_\mathrm{f}} \langle\xi\rangle_s \, \cos\theta \, \mathrm{d}o = \int_0^{2\pi} \int_0^{\theta_\mathrm{max}} \langle\xi\rangle_s \, \cos\theta \, \sin\theta \, \mathrm{d}\theta \, \mathrm{d}\phi. \tag{6.17}$$

The integration should be performed only over the region of the full efficiency. Thus, we make a transformation of this integral. First, the averaged efficiency becomes equal to unity ($\langle\xi\rangle_s = 1$). Second, the integration limits should be transformed to follow the found approximation of the full efficiency region. To solve the integral, we split it into two parts

$$A_\Omega = \int_0^{2\pi} \int_0^{\theta_\mathrm{max}} \cos\theta \, \sin\theta \, \mathrm{d}\theta \, \mathrm{d}\phi - \int_0^{\theta_\mathrm{max}} \int_{\phi_1(\theta)}^{\phi_2(\theta)} \cos\theta \, \sin\theta \, \mathrm{d}\phi \, \mathrm{d}\theta. \tag{6.18}$$

The order of integration is swapped in the second integral because of the appearing dependence of the azimuthal angle from the zenith angle.

The first integral in (6.18) is known. It is the aperture for the case when the full-efficiency region fills the whole sky up to a maximal zenith angle, θ_max demarcating the edge of the fiducial angular selection

$$\int_0^{2\pi} \int_0^{\theta_\mathrm{max}} \cos\theta \, \sin\theta \, \mathrm{d}\theta \, \mathrm{d}\phi = \pi \, [1 - \cos^2\theta_\mathrm{max}]. \tag{6.19}$$

To solve the second integral we use the parametrization of a circle on the unit sphere given in (6.16) to express the azimuthal angle of the edge of the area as a function of zenith angle

$$\phi = \pm \arccos \frac{\cos\rho - \cos\theta\cos\theta_0}{\sin\theta\sin\theta_0}. \tag{6.20}$$

The functions $\phi_1(\theta)$ and $\phi_2(\theta)$ becomes

$$\begin{aligned} \phi_1(\theta) &= 0, \\ \phi_2(\theta) &= \arccos \frac{\cos\rho - \cos\theta\cos\theta_0}{\sin\theta\sin\theta_0}. \end{aligned} \tag{6.21}$$

The plus-minus sign turns into a factor two in front of the integral due to the symmetry of the integration area.

The substitution of the corresponding functions and taking into account the factor due to the symmetry of the integration area gives

$$\int_0^{\theta_{\max}} \int_{\phi_1(\theta)}^{\phi_2(\theta)} \cos\theta \, \sin\theta \, \mathrm{d}\phi \, \mathrm{d}\theta = 2 \int_0^{\theta_{\max}} \int_0^{\arccos \frac{\cos\rho - \cos\theta \cos\theta_0}{\sin\theta \sin\theta_0}} \cos\theta \, \sin\theta \, \mathrm{d}\phi \, \mathrm{d}\theta = 2 \int_0^{\theta_{\max}} \arccos \frac{\cos\rho - \cos\theta \cos\theta_0}{\sin\theta \sin\theta_0} \cos\theta \, \sin\theta \, \mathrm{d}\theta. \quad (6.22)$$

The finite domain of the arccosine function provides the natural limit to the integral depending on the size of the efficiency suppressed area and its location. Due to this fact the limits of the last integral remain unchanged.

The combination of the obtained solutions (6.19) and (6.22) provides the value for the aperture integral [246]:

$$A_\Omega = \pi \left[1 - \cos^2\theta_{\max}\right] - 2 \int_0^{\theta_{\max}} \arccos \frac{\cos\rho - \cos\theta \cos\theta_0}{\sin\theta \sin\theta_0} \cos\theta \, \sin\theta \, \mathrm{d}\theta. \quad (6.23)$$

The value of the remaining integral can be found numerically with a high precision.

It is worthwhile to analyze the achieved result. First of all, the problem of numerical integration over a sphere is one of unsolved problems in modern mathematics [247, 248]. There are various approaches to this problems, however, they all involve specially designed grids of sample points over the sphere to achieve an accurate result. The present case of integration of the efficiency over the unit sphere is also a problem of the same type. Thus, the fact that it was possible to transform the problem from a two-dimensional integral to a one-dimensional, completely changes the situation. The resulting integral can be accurately solved with any of the developed algorithms for numerical integration since its integrand is a smooth, non-oscillating function. Thus, the uncertainties of the numerical integration become negligible for the considered problem of the aperture evaluation.

6.2.4. The Aperture in the Full-Efficiency Sky Regions

The developed method for estimation of the sky region corresponding to the full-efficiency regime and a semi-analytical method to compute the aperture for this region is applied to the particular case of the estimation of the energy spectrum of cosmic rays. This is the subject of this section.

In this work, the cosmic-ray energy spectrum is estimated within the logarithmic energy bins centered at $10^{17.3}$, $10^{17.5}$, $10^{17.7}$, $10^{18.0}$ eV and with the logarithmic bin width of $\Delta \lg E_i = 0.2$ for the first three and $\Delta \lg E_i = 0.4$ for the last bin of the highest energy. Such a selection is motivated by the previous work [249]. The aperture is evaluated for the energies corresponding to the bin centers for all four configurations of the antenna array listed in Table 4.1. The reference value of $X_{\max}$ used for the estimation was selected to be equal to 650 g/cm^{-1} since it roughly corresponds to the mean value in the considered

energy region (see Figure 1.5). Using a single fixed value does not significantly influence the aperture estimation because of the weak dependence of the size of the sky region of the full efficiency on the $X_{\max}$ values (see Figure 6.2). All these computations follow the ideas described in [238].

The estimated locations of the sky regions of suppressed efficiency (their centers and the angular radii) and the specific values of the aperture for the full-efficiency regions are given in Appendix D for the considered set of energies.

6.3. OBSERVATION TIME

The observation time is another crucial factor for the reconstruction of the cosmic-ray energy spectrum, which can be clearly seen from (6.25). Estimation of the actual value of this time for a real detector can be challenging because of the multiple instrumentation and environmental factors relevant for the operation of the detector. In case of the Tunka-133 instrument triggering the Tunka-Rex array, these factors are related to the cloud coverage appearing above the array and disturbing the Cherenkov light propagation from the shower to the instrument. These periods are excluded from the data during the initial steps of the processing by the Tunka-133 group. Thus, even one operation run can contain several gaps in the data taking.

To estimate the observation time, it is reasonable to see cosmic rays as a statistical process, namely, utilize the fact that they come from any direction on the sky randomly as a Poisson point process. It is known that in the time domain the events of this process appear in a certain manner. The time intervals between two consecutive events, τ, are distributed according to the exponential distribution with the probability density function

$$f(\tau; \langle\tau\rangle) = \frac{1}{\langle\tau\rangle} e^{-\tau/\langle\tau\rangle}. \tag{6.24}$$

The symbol $\langle\tau\rangle$ denotes the mean time between consecutive events. The product of this mean time with the total number of events estimates the total operation time.

Since the energy threshold of the Tunka-Rex array is high, the number of events per observation run and season are limited. Thus, instead of Tunka-Rex events, the timestamps of the cosmic-ray events observed by Tunka-133 are used for estimation of the observation time. The dataset used for this estimation is a subset of events with energies above 10^{16} eV according to the Tunka-133 reconstruction. The data used in this analysis are shared in the framework of the internal cooperation between the groups.

Plots in Figure 6.3 show results of the fit $\langle\tau\rangle$ to the data from all the observation seasons and to all the data together. Table 6.1 summarizes the results of the estimation of the observation time. The mean time between the consecutive events significantly varies from season to season. This variation comes from the variation of the energy threshold of Tunka-133, which, in turn, is connected with the occasional tuning of the detection thresholds of the light detectors due to variations in the light environment during the observations.

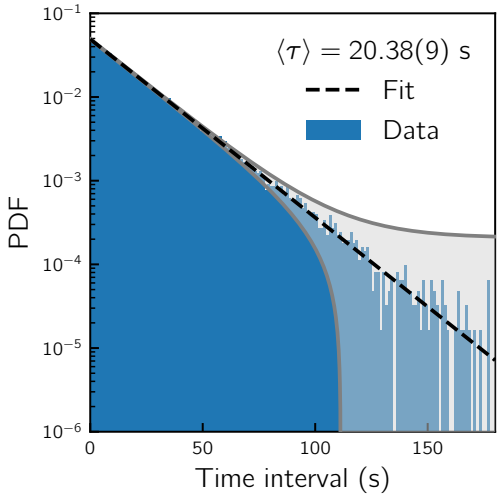

(a) Generation 1a (2012/13)

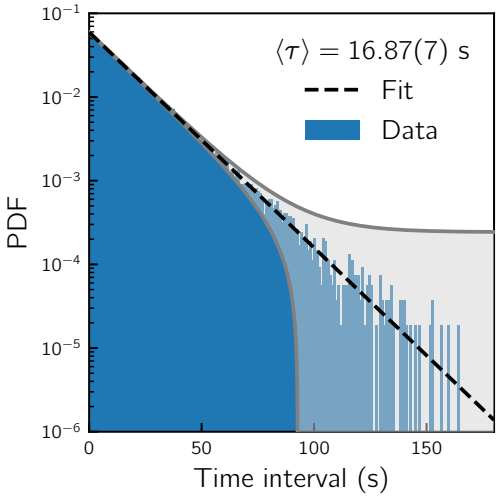

(b) Generation 1b (2013/14)

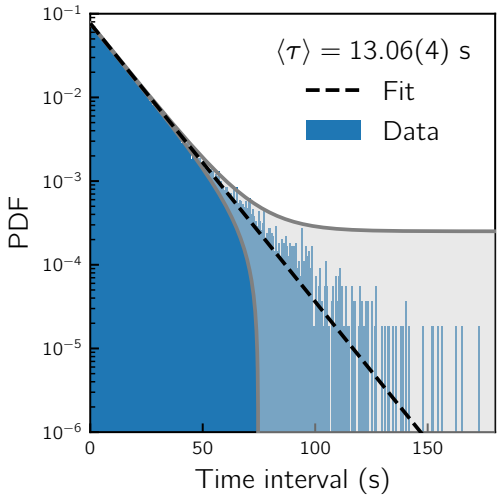

(c) Generation 2 (2015/16)

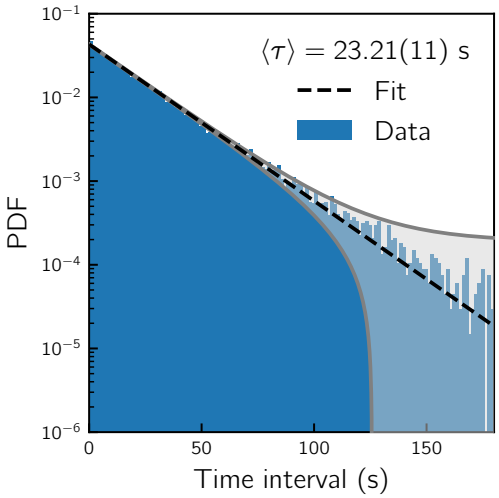

(d) Generation 3 (2016/17)

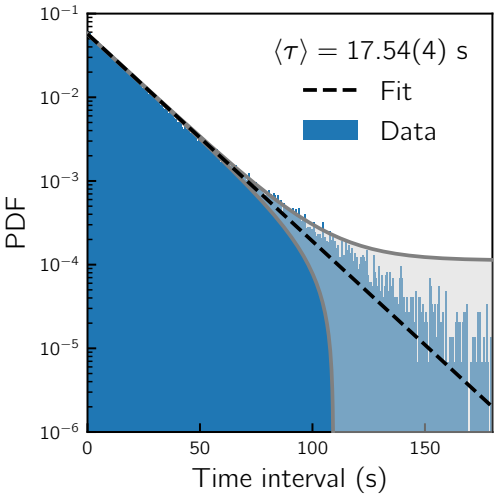

(e) All seasons

Figure 6.3: Estimation of the mean time interval between the consecutive Tunka-133 cosmic-ray events with energies above 10^{16} eV for the individual seasons with a given antenna configurations (denoted as generations); and for all seasons together. The plots show the histogrammed time intervals into the bins obtain with the Freedman Diaconis estimator overlaid with the fit probability density function of exponential distributions. The gray band shows the uncertainty.

Table 6.1: Summary of the observation time estimation with the exponential distribution method applied for the trigger events. The table shows the fit $\langle\tau\rangle$, number of the cosmic-ray events used in the analysis (cosmic-ray events with energies above 10^{16} eV detected and reconstructed by Tunka-133), and the resulting observation time for individual seasons corresponding to a given antenna configuration denoted as generation.

Gen.	$\langle\tau\rangle$ (s)	# of events	Time (s)
1a	20.38(9)	52527	$1.0702(47) \times 10^6$
1b	16.87(7)	55583	$0.9378(40) \times 10^6$
2	13.06(4)	85528	$1.1170(38) \times 10^6$
3	23.21(11)	47988	$1.1139(51) \times 10^6$
Sum			$4.2389(89) \times 10^6$
Total	17.54(4)	241626	$4.2387(86) \times 10^6$

The uncertainties shown in the tables come from the minimal gradient estimation. The uncertainties for the plots are obtained with parametric bootstrapping. The estimation was done with the MINUIT library wrapped in a modern Python interface [216]. The code provides build-in capabilities for building an unbinned negative likelihood model for consecutive minimization to find the parameters of interest. These capabilities provided the present estimation. It is clear that the unreasonably large time intervals between some events coming from the time gaps disturb the fit. To avoid such influence all intervals above 180 s were excluded.

It is important to note that the uncertainties of the time estimation are small. The relative values are on the level of fractions of a percent, which is smaller than the pure statistical uncertainties. Due to this fact these uncertainties are not considered in the further steps of reconstructing the spectrum.

6.4. RAW ENERGY SPECTRUM

The raw spectrum[2] is reconstructed by counting the air-shower events observed from the sky regions of full efficiency, and dividing them by the Tunka-Rex fiducial area, the estimated aperture, and the operation time (see Sections 6.2 and 6.3 correspondingly). The sky regions of the full efficiency used for counting events are the same as the ones used for the aperture estimation.

The data used for the energy-spectrum reconstruction are the Tunka-Rex air-shower measurements from all seasons reconstructed with the standard analysis described in Section 4.5.4 with the corresponding updates described in Section 4.5.5.

[2]A preliminary cosmic-ray energy spectrum reconstructed with an early version of the efficiency model [235] and for events reconstructed with the template analysis procedure [238] was published in [249] and is available in the KCDC database [37].

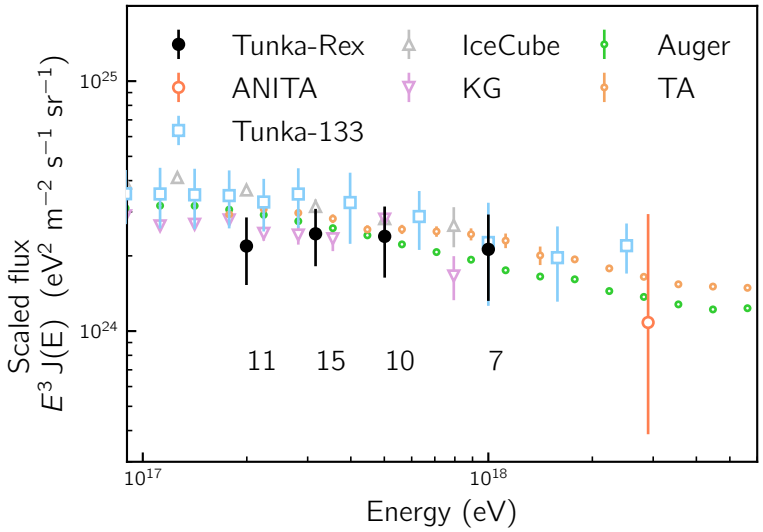

Figure 6.4: Cosmic-ray energy spectrum reconstructed with the full Tunka-Rex dataset and the developed aperture model. The error bars show statistical uncertainties. The numbers below the data indicate the number of events in each of the logarithmic bins. For a better visibility, all the data are scaled by the cube of the energy. Measurements of other modern cosmic-ray observatories are shown for reference (the data used for this plot are the same as used for Figure 1.1). In addition, a measurement of the cosmic-ray flux made by ANITA, a balloon-borne air-shower radio detector, is shown as a measurement performed by other radio instrument [250]).

In this work we estimate the cosmic-ray energy spectrum within the logarithmic energy bins centered at $10^{17.3}$, $10^{17.5}$, $10^{17.7}$, $10^{18.0}$ eV and with the logarithmic bin width of $\Delta \lg E_i = 0.2$ for the first three and $\Delta \lg E_i = 0.4$ for the last bin of the highest energy. Such a selection is motivated by the previous work [249]. The air-shower events are counted within these bins for each of the observational seasons since the antenna layout was different in each season because of the active development of the array instrumentation. To take into account these dependence of the aperture not only from the cosmic-ray energy but also from the array layout, (6.25) is transformed correspondingly. Essentially, contributions from the individual observation seasons are summed up using the additive character of the aperture quantity

$$J(E_i) = \frac{1}{S_\mathrm{f}} \sum_{\mathrm{gen}=\{1a,1b,2,3\}} \frac{N_i^{\mathrm{gen}}}{A_\Omega^{\mathrm{gen}}(E_i)\, T^{\mathrm{gen}}\, \Delta E_i}. \tag{6.25}$$

The particular numbers of events within each of the energy bins per season are presented in Appendix D in the same table as all full-efficiency cuts used for the present spectrum reconstruction.

Figure 6.4 shows the reconstructed energy spectrum and the measurements performed by other modern cosmic-ray observatories provided for reference. The error bars show the statistical uncertainty. The number of the air-shower events in each of the logarithmic

bins is also indicated. In addition, a measurement of the cosmic-ray flux from another radio instrument is shown. The flux (y-axis) is scaled by the cube of the energy for better visibility.

The resulting cosmic-ray energy spectrum is a so-called raw spectrum obtained directly from air-shower data and with knowledge of the instrument aperture and observation time. To estimate the actual energy spectrum of cosmic rays, additional transformations should be applied to the raw spectrum. This procedures include, but are not limited to, the unfolding of the instrument response and a constant intensity cut. Moreover, unaccounted uncertainties could be hidden in the estimation of the operation time and the reconstruction of the energy. However, since the main purpose of this energy spectrum reconstruction is to demonstrate the application of the developed efficiency model to a specific radio array, the detailed study of the listed transformations and sources of uncertainties are beyond the scope of the present work.

6.5. CONCLUDING REMARKS

This chapter demonstrated an application of the developed efficiency model presented in the previous chapter to a specific problem of the reconstruction of the cosmic-ray energy spectrum from the Tunka-Rex observations of air showers. This chapter revealed the complexity of the efficiency of a radio array, with Tunka-Rex as example, which is expected from the physics of the air-shower radio emission. On the way from sky maps of the efficiency to the aperture within only the fully efficient regions in the sky, a new semi-analytical method of the aperture estimation was developed. In contrast to a straightforward estimation of the aperture as a two-dimensional integral, it allows for converting it into a one-dimensional integral, which can be easily computed without sophisticated numerical procedures. The developed methods allowed for an unbiased estimation of the cosmic-ray flux with the enlarged sample of air-shower data and with energy reconstruction method updated during this work. Despite some obvious statistical limitations of the obtained result, this real-life problem demonstrates that the explicit probabilistic approach chosen for developing a model of such a complex object as the efficiency of a radio array provides valuable results.

CONCLUSION

The method of radio detection of cosmic-ray air showers is in the second decade after upcoming digital technologies renewed the interest towards it. The previous decade was devoted mainly to the development of the instrumentation for detection of the air-shower radio emission, detailed understanding of the emission mechanisms, and the development of reconstruction methods able to reconstruct parameters of air showers from the radio measurements. In the present decade, the radio technique faces new challenges related to enhancing the accuracy of reconstruction methods of the air-shower parameters and using it for measurements of cosmic-ray characteristics as an astrophysical phenomenon. The present work addresses both.

Accurate methods for reconstruction of the air-shower parameters, along with a proper understanding of the radio emission mechanisms and used instrumentation, are key elements in providing the absolute energy scale for a cosmic-ray instrument. An accurate scale is crucial for an adequate astrophysical interpretation of any cosmic-ray measurements. The Auger Engineering Radio Array (AERA) is performing an extensive work on providing a calibration of the absolute scale that can be used for cross-checking the energy scale of the Pierre Auger Observatory, the world's largest cosmic-ray detector complex. A part of this work is an end-to-end, full-fledged simulation study. The processing of the simulation includes the complete detector response and the complete reconstruction procedure matching those used for observed events. The energy scale obtained with these simulations shows a good agreement with the one obtained for the observations. This result indicates that despite unavoidable differences inherent in the analysis of simulations and observations, such direct comparisons are possible. The future research will improve our understanding of the data analysis methods and their influence to the final result of the absolute energy scale calibration.

The central part of this work is devoted to a novel approach to a previously unsolved problem of the efficiency and aperture estimation of a cosmic-ray radio array. The efficiency and its integral, the aperture, are few of the crucial components for reconstructing unbiased characteristics of cosmic rays as an astrophysical phenomenon. The usual approach of processing many Monte-Carlo simulations of air showers for estimation of the instrument efficiency is challenging in case of radio arrays. The corresponding simulations of air-shower radio emission are computationally complex and require large computing time for each air shower and, consequently, for the entire simulation library. In contrast to this usual practice, the approach to the efficiency estimation developed in this work uses an explicit probabilistic treatment of the radio emission footprint on the ground and the process of its detection. This approach is implemented in a corresponding model for the estimation of the efficiency of the Tunka Radio extension, Tunka-Rex. The model enables an accurate estimation of the efficiency of the radio instrument in its full complex behavior as function of the air-shower incoming direction, the depth of shower

maximum, and the cosmic-ray energy. The semi-analytic form of the model is beneficial since it provides a transparent connection between the different components of the model and a transparent estimation of the uncertainty of the final result. Tunka-Rex is a unique instrument for this efficiency modeling. The array is located on the site of the Tunka-133 Cherenkov timing array and is triggered by it. Since the energy threshold of Tunka-133 is about two orders of magnitude lower than that of Tunka-Rex with the standard analysis, Tunka-133 works in the full efficiency regime over the entire Tunka-Rex energy range. This unique combination of instruments allowed for a validation of the developed model not only against Monte-Carlo simulations, but also against the observations. Both types of validation indicate that the model is capable to reliably identify the full efficiency regions of a radio instrument and, in particular, of Tunka-Rex. The developed model has a generic nature and with an appropriate adaptation of certain components can be applied to any cosmic-ray radio array.

The developed model of the Tunka-Rex efficiency was used to estimate energy-dependent full-efficiency sky regions. This formed the foundation for the reconstruction of the energy spectrum based on the Tunka-Rex data. This measurement of the energy spectrum with a radio instrument is the first observation of this kind. The resulted spectrum, despite obvious statistical limitations, agrees well with other measurements of the cosmic-ray energy spectrum. Such an agreement indicates that, first, the Tunka-Rex energy-reconstruction methods, which are calibrated against end-to-end, full-fledged CoREAS simulations, provide accurate results, and, second, the developed efficiency model accurately reflects the full-efficiency regions of the instrument.

The future prospects of the radio technique are bright. The world's largest cosmic-ray detector, the Pierre Auger Observatory, is undergoing the AugerPrime upgrade, which includes radio antennas as a part of the baseline design. After this upgrade, the observatory will operate the world's largest cosmic-ray radio array. Analysis of the observations from this array will unavoidably use all advances of the radio technique achieved to date. The energy scale analysis and the approach to the efficiency estimation will contribute to these advances.

The generic nature of the approach to the efficiency estimation developed in this work will also be useful for other upcoming instrumentation since the question of the efficiency and aperture estimation is crucial for cosmic ray measurements, such as energy spectrum, mass composition, and anisotropies of the incoming directions, performed by any radio instrument on the globe.

APPENDIX A

LDF PARAMETERS

During the Tunka-Rex analysis development, some details of the signal processing and the reconstruction were changed (see Chapter 4 for details). To take them all into account into the current analysis, the parameters of the LDF model were updated to reflect these changes.

The parameters were fit to the CoREAS Monte-Carlo simulations consisting of hydrogen-induced and iron-induced showers in equal amount. The energy distribution of the showers is discrete ($E = 10^{17.0}$, $10^{17.3}$, $10^{17.5}$, $10^{17.7}$, $10^{18.0}$, $10^{18.3}$, $10^{18.5}$ eV). This set covers the energy region of the Tunka-Rex instrument with low efficiency at the lower edge and almost full efficiency at the higher one.

The fitting procedure is organized as follows. First, the results of the simulations are symmetrized with the operator (4.4). Then, the free parameters of the Gaussian function in the form (4.10) are fit to match the symmetrized lateral distributions. As a final step, the distributions of the found parameters of a, b, and κ are parametrized with (4.14) and (5.4). Thus, the Tunka-Rex reconstruction procedure becomes calibrated to the absolute energy scale provided by the CoREAS Monte-Carlo simulations passed through the end-to-end, full-fledged detector simulation of the Tunka-Rex instrument. Table A.1 summarizes the obtained values.

Table A.1: Values of the LDF parameters obtained by the fitting procedure.

Parameter	Value
κ	705.37
A	-1994.80
B	-572.77
$\bar{B}$	3.871×10^{-3}
A_{200}	2.205×10^{-5}
A_{201}	4.810×10^{-6}
A_{210}	-2.010×10^{-6}
A_{211}	-5.370×10^{-6}

APPENDIX B

ACCURACY OF AVERAGE EFFICIENCY ESTIMATION

The application of the efficiency model developed in this work (see Chapter 5) involves estimation of the averaged efficiencies over the fiducial area of a cosmic-ray radio array (see Chapter 6). These estimations are performed with individual air showers distributed over a square grid on the fiducial area of the instrument. The step size of the grid can vary, changing the final accuracy of the estimation and the computation time. This appendix presents the results of studying the accuracy of the efficiency estimation and the computing time for a range of the step sizes of the square grid.

Figure B.1 shows the model performance for a test case when the averaged efficiency is close to 0.5 for four grid step sizes (100, 50, 25, and 10 m). One important property of the model clearly visible in this plot is that the model uncertainties cover the correct value of the averaged efficiency, in this case the 10-m grid value depicted with the gray line, even with the coarsest grid. Figure B.2 shows the accuracy for the cases when the averaged efficiency is close to zero or unity, respectively. The low-efficiency case features a similar behavior to the one of the half-efficiency for all four step sizes. For the high-efficiency case, the situation becomes worse for the 100-m grid. The estimation significantly deviates from the correct value and the uncertainties do not cover it.

Based on the results presented in this appendix, the step size of 50 m was chosen for the estimation of the averaged efficiencies used in the application of the model (see Chapter 6). This step size ensures an accuracy on the one-percent level over the entire range of the averaged efficiencies.

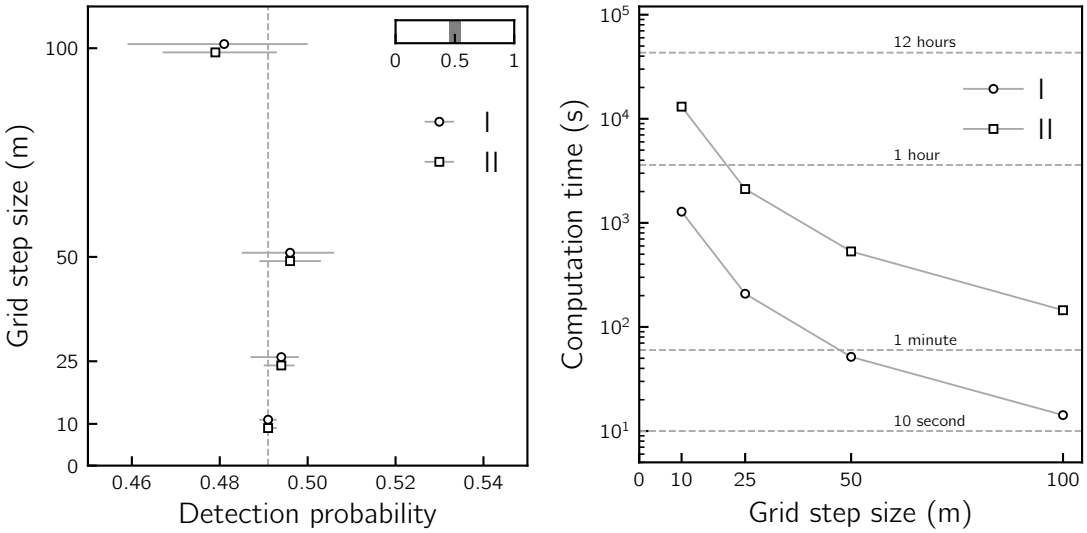

Figure B.1: Measurements of the model performance in the middle of region of the averaged detection efficiency over the Tunka-Rex fiducial area (at $\theta = 35°$, $\phi = 270°$, $E = 10^{17.3}$ eV, $X_{\max} = 658$ g/cm^2). The two types of markers depict information related to methods of the trigger probability estimation: I — method of inference with probabilistic calculation, II — method of inference with Monte-Carlo experiments. The detection condition used for this estimation is at least three antennas with signal. *Left*: accuracy of the model prediction with different grid step sizes; the gray band in the inset shows the region of the whole probability range of the main plot (for presentation purposes the data points corresponding to the two methods are placed slightly apart in the vertical direction from their actual positions, which are marked with the ticks on the vertical axis). The vertical dashed line is provided for the eye-guiding purposes. It depicts the value of the averaged efficiency computed with the probabilistic calculation on the 10-m grid. *Right*: computation time of the average efficiency over the Tunka-Rex fiducial area; the lines connecting the data points are for eye-guiding purposes.

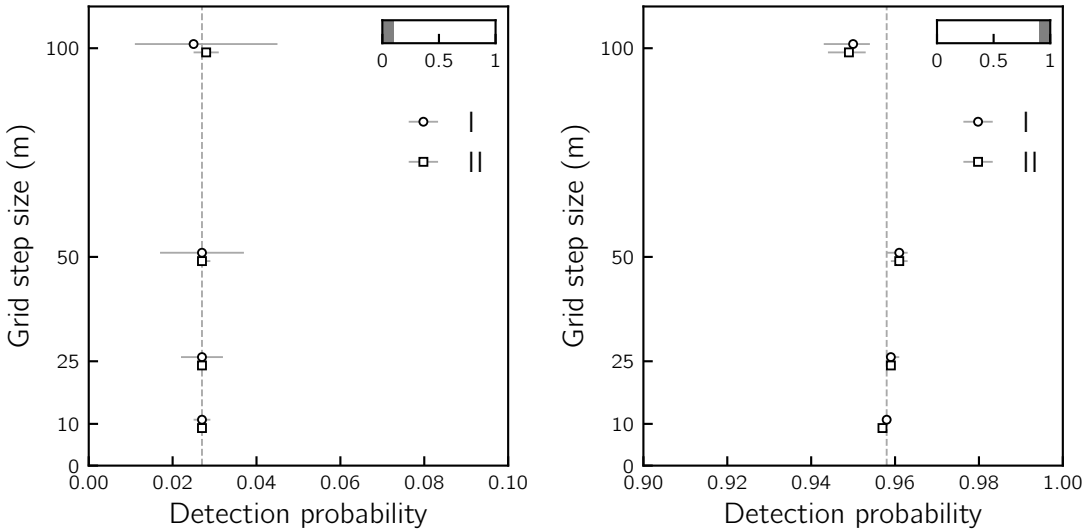

Figure B.2: Additional measurements of the model performance. The two types of markers depict information related to methods of the detection probability estimation: I — method of inference with probabilistic calculation, II — method of inference with Monte-Carlo experiments. The gray band in the inset shows the region of the whole probability range of the main plot. The trigger condition used for this estimation is at least three antennas with signal. The vertical dashed lines are provided for the eye-guiding purposes. They depict the values of the averaged efficiency computed with the probabilistic calculation on the 10-m grid. For presentation purposes the data points corresponding to the two methods are placed slightly apart in the vertical direction from their actual positions, which are marked with the ticks on the vertical axis. *Left*: accuracy of the model in the region of low averaged detection efficiency over the Tunka-Rex fiducial area ($\theta = 25°$, $\phi = 270°$, $E = 10^{17.3}$ eV, $X_{\max} = 658$ g/cm^2). *Right*: accuracy of the model in the region of high averaged detection efficiency over the Tunka-Rex fiducial area ($\theta = 43°$, $\phi = 270°$, $E = 10^{17.3}$ eV, $X_{\max} = 658$ g/cm^2).

APPENDIX C

COMPUTING TIME

Chapter 5 presents two methods for the estimation of the trigger probability of a cosmic-ray radio array: inference with probabilistic calculations and inference with Monte-Carlo experiments (see Sections 5.3.1 and 5.3.2). The second one is developed to mitigate the computational complexity which increases with number of antennas required for the triggering of a cosmic-ray radio array. Figure C.1 shows the computation time as function of the number of the antennas for a given test case. It is clear, that the method of the probabilistic calculations features a rapid increase of computational complexity and computing time when the more antennas with signal are required, while the method of the Monte-Carlo experiments show an almost unchanged computational complexity. On the other hand, for detection conditions featuring small antenna numbers (3 or 4), using the method of the probabilistic calculation is beneficial since it provides a computing time almost an order of magnitude smaller in comparison to the method of the Monte-Carlo experiments.

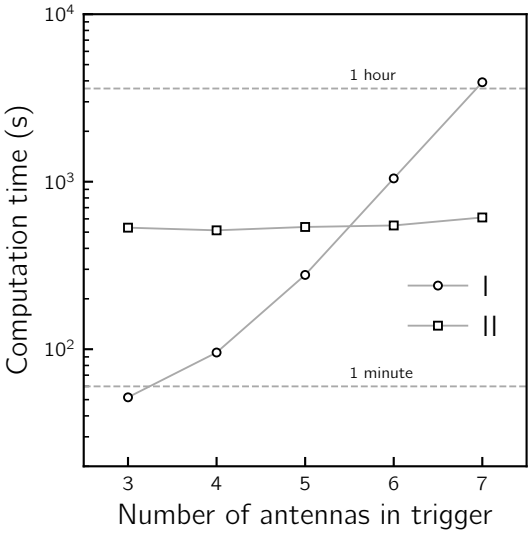

Figure C.1: Comparison of the computation time for various number of antennas in the trigger condition (I — method of inference with probabilistic calculations, II — method of inference with Monte-Carlo experiments). The test case is computing the averaged efficiency over the Tunka-Rex fiducial area for an event with the following parameters: $\theta = 35°$, $\phi = 270°$, $E = 10^{17.3}$ eV, $X_{\max} = 658$ g/cm^2, grid step size is 50 m.

APPENDIX D

FULL-EFFICIENCY REGIONS

The application of the developed efficiency model to a particular example (see Chapter 6) uses the full-efficiency regions in the sky for the event selection and the computation of the aperture. Table D.1 summarizes information on these regions. The center and radius show the zenith location of the circular region of the suppressed efficiency and the angular radius of this region. The sky area over the range of the zenith angles from 0° to 50° (see Chapter 4) without the suppressed efficiency region forms the sky region of the full efficiency. The fifth column shows the angular aperture, A_Ω, computed for the sky regions of the full efficiency (following (6.23)). The last column gives the number of the events from the standard Tunka-Rex reconstruction (see Chapter 4) selected with the full-efficiency regions for the reconstruction of the cosmic-ray energy spectrum (see Section 6.4).

The following minimal antenna numbers were used for computing the full-efficiency regions: 4 antennas for generations 1a and 1b, 9 antennas for generation 2, 13 antennas for generation 3. It should be noted that the detection conditions were motivated by the previous work [238]. That selection provides a stable air-shower reconstruction procedure. In future studies considering the individual uptime of the antennas, these criteria can be optimized, which likely can increase the number of events for consecutive analyses.

Table D.1: Parameters of the full-efficiency regions in the sky used in the application of the efficiency model for the four generations of the antenna configurations of Tunka-Rex.

Gen.	$\lg E_i$	Center (°)	Radius (°)	A_Ω (sr)	# of events
1a	17.3	4.59	47.45	0.17	3
	17.5	5.94	40.83	0.51	6
	17.7	7.09	34.09	0.86	3
	18.0	9.57	24.34	1.32	2
1b	17.3	4.58	47.40	0.17	4
	17.5	5.95	40.81	0.51	5
	17.7	7.07	34.07	0.87	1
	18.0	9.56	24.32	1.32	4
2	17.3	4.01	48.19	0.13	2
	17.5	5.38	42.14	0.44	1
	17.7	6.20	35.76	0.78	2
	18.0	8.46	26.96	1.21	1
3	17.3	4.75	47.20	0.18	2
	17.5	5.79	40.85	0.51	3
	17.7	6.98	34.37	0.85	4
	18.0	9.53	24.94	1.29	0

BIBLIOGRAPHY

[1] P. Zyla et al., "Review of Particle Physics", PTEP **2020**, 083C01 (2020).

[2] T. K. Gaisser, R. Engel, and E. Resconi, *Cosmic Rays and Particle Physics* (2016).

[3] Y. Sekido and H. Elliot, *Early history of cosmic ray studies*, Vol. 118 (1985).

[4] R. A. Millikan, "High Frequency Rays of Cosmic Origin", Nature **116**, 823–825 (1925).

[5] A. C. Cummings et al., "Galactic Cosmic Rays in the Local Interstellar Medium: Voyager 1 Observations and Model Results", ApJ **831**, 18, 18 (2016).

[6] R. Beck et al., "Synthesizing observations and theory to understand galactic magnetic fields: progress and challenges", Galaxies **8**, 4 (2019).

[7] T. Dunham, "The material of interstellar space", Proceedings of the American Philosophical Society **81**, 277–293 (1939).

[8] M. Ahlers and F. Halzen, "Opening a new window onto the universe with IceCube", Progress in Particle and Nuclear Physics **102**, 73–88 (2018).

[9] Y. Revaz et al., *Star Formation in Galaxy Evolution: Connecting Numerical Models to Reality*, Saas-Fee Advanced Course, Jan. 2016.

[10] P. F. Hopkins et al., "Effects of different cosmic ray transport models on galaxy formation", MNRAS **501**, 3663–3669 (2021).

[11] R. Aloisio, E. Coccia, and F. Vissani, *Multiple Messengers and Challenges in Astroparticle Physics* (2018).

[12] A. M. W. Mitchell, "Status of Ground-based and Galactic Gamma-ray Astronomy", arXiv e-prints, arXiv:2109.13753, arXiv:2109.13753 (2021).

[13] M. Kachelriess, "Extragalactic cosmic rays", arXiv e-prints, arXiv:2201.04535, arXiv:2201.04535 (2022).

[14] L. A. Anchordoqui, "Ultra-high-energy cosmic rays", Phys. Rep. **801**, 1–93 (2019).

[15] M. Aguilar et al., "Precision Measurement of the Proton Flux in Primary Cosmic Rays from Rigidity 1 GV to 1.8 TV with the Alpha Magnetic Spectrometer on the International Space Station", Phys. Rev. Lett. **114**, 171103, 171103 (2015).

[16] Y. S. Yoon et al., "Proton and Helium Spectra from the CREAM-III Flight", ApJ **839**, 5, 5 (2017).

[17] E. C. Stone et al., "Cosmic ray measurements from Voyager 2 as it crossed into interstellar space", Nature Astronomy **3**, 1013–1018 (2019).

[18] M. Aguilar et al., "Observation of the Identical Rigidity Dependence of He, C, and O Cosmic Rays at High Rigidities by the Alpha Magnetic Spectrometer on the International Space Station", Phys. Rev. Lett. **119**, 251101, 251101 (2017).

[19] H. S. Ahn et al., "Energy Spectra of Cosmic-ray Nuclei at High Energies", ApJ **707**, 593–603 (2009).

[20] J. J. Engelmann et al., "Charge composition and energy spectra of cosmic-ray nuclei for elements from Be to Ni - Results from HEAO-3-C2.", A&A **233**, 96–111 (1990).

[21] M. Amenomori et al., "The All-Particle Spectrum of Primary Cosmic Rays in the Wide Energy Range from 10^{14} to 10^{17} eV Observed with the Tibet-III Air-Shower Array", ApJ **678**, 1165–1179 (2008).

[22] M. G. Aartsen et al., "Cosmic ray spectrum and composition from PeV to EeV using 3 years of data from IceTop and IceCube", Phys. Rev. D **100**, 082002, 082002 (2019).

[23] M. G. Aartsen et al., "Measurement of the cosmic ray energy spectrum with IceTop-73", Phys. Rev. D **88**, 042004, 042004 (2013).

[24] M. Bertaina et al., "KASCADE-Grande energy spectrum of cosmic rays interpreted with post-LHC hadronic interaction models", in 34th international cosmic ray conference (icrc2015), Vol. 34, International Cosmic Ray Conference (July 2015), page 359.

[25] N. M. Budnev et al., "The primary cosmic-ray energy spectrum measured with the Tunka-133 array", Astroparticle Physics **117**, 102406, 102406 (2020).

[26] V. Verzi, "Measurement of the energy spectrum of ultra-high energy cosmic rays using the Pierre Auger Observatory", in 36th international cosmic ray conference (icrc2019), Vol. 36, International Cosmic Ray Conference (July 2019), page 450.

[27] D. Ivanov, "Energy Spectrum Measured by the Telescope Array", in 36th international cosmic ray conference (icrc2019), Vol. 36, International Cosmic Ray Conference (July 2019), page 298.

[28] M. Aguilar et al., "Towards Understanding the Origin of Cosmic-Ray Electrons", Phys. Rev. Lett. **122**, 101101, 101101 (2019).

[29] O. Adriani et al., "Cosmic-Ray Electron Flux Measured by the PAMELA Experiment between 1 and 625 GeV", Phys. Rev. Lett. **106**, 201101, 201101 (2011).

[30] M. Aguilar et al., "Towards Understanding the Origin of Cosmic-Ray Positrons", Phys. Rev. Lett. **122**, 041102, 041102 (2019).

[31] O. Adriani et al., "Cosmic-Ray Positron Energy Spectrum Measured by PAMELA", Phys. Rev. Lett. **111**, 081102, 081102 (2013).

[32] M. Aguilar et al., "Antiproton Flux, Antiproton-to-Proton Flux Ratio, and Properties of Elementary Particle Fluxes in Primary Cosmic Rays Measured with the Alpha Magnetic Spectrometer on the International Space Station", Phys. Rev. Lett. **117**, 091103, 091103 (2016).

[33] O. Adriani et al., "Measurement of the flux of primary cosmic ray antiprotons with energies of 60 MeV to 350 GeV in the PAMELA experiment", Soviet Journal of Experimental and Theoretical Physics Letters **96**, 621–627 (2013).

[34] M. Ackermann et al., "The Spectrum of Isotropic Diffuse Gamma-Ray Emission between 100 MeV and 820 GeV", ApJ **799**, 86, 86 (2015).

[35] M. G. Aartsen et al., "A Combined Maximum-likelihood Analysis of the High-energy Astrophysical Neutrino Flux Measured with IceCube", ApJ **809**, 98, 98 (2015).

[36] D. Maurin et al., "Cosmic-Ray Database Update: Ultra-High Energy, Ultra-Heavy, and Antinuclei Cosmic-Ray Data (CRDB v4.0)", Universe **6**, 102 (2020).

[37] *KASCADE Cosmic Ray Data Centre (KCDC) / Open β*, `https://kcdc.ikp.kit.edu` (visited on 01/14/2020).

[38] F. Ochsenbein et al., *The VizieR database of astronomical catalogues*.

[39] Z. N. Shen and G. Qin, "Modulation of Galactic Cosmic Rays in the Inner Heliosphere over Solar Cycles", ApJ **854**, 137, 137 (2018).

[40] I. Leya, J. Hirtz, and J.-C. David, "Galactic Cosmic Rays, Cosmic-Ray Variations, and Cosmogenic Nuclides in Meteorites", ApJ **910**, 136, 136 (2021).

[41] I. V. Moskalenko, "Galactic cosmic rays and diffuse radiation", in Russian, Doctor of Sciences in Physics and Mathematics (Hansen Experimental Physics Laboratory, Physics Department, Stanford University, 2016).

[42] O. Adriani et al., "An anomalous positron abundance in cosmic rays with energies 1.5-100GeV", Nature **458**, 607–609 (2009).

[43] M. Ackermann et al., "Measurement of Separate Cosmic-Ray Electron and Positron Spectra with the Fermi Large Area Telescope", Phys. Rev. Lett. **108**, 011103, 011103 (2012).

[44] M. Aguilar et al., "First Result from the Alpha Magnetic Spectrometer on the International Space Station: Precision Measurement of the Positron Fraction in Primary Cosmic Rays of 0.5-350 GeV", Phys. Rev. Lett. **110**, 141102, 141102 (2013).

[45] I. V. Moskalenko and A. W. Strong, "Production and Propagation of Cosmic-Ray Positrons and Electrons", ApJ **493**, 694–707 (1998).

[46] O. Adriani et al., "New Measurement of the Antiproton-to-Proton Flux Ratio up to 100 GeV in the Cosmic Radiation", Phys. Rev. Lett. **102**, 051101, 051101 (2009).

[47] M. Aguilar et al., "Precision Measurement of the Boron to Carbon Flux Ratio in Cosmic Rays from 1.9 GV to 2.6 TV with the Alpha Magnetic Spectrometer on the International Space Station", Phys. Rev. Lett. **117**, 231102, 231102 (2016).

[48] O. Adriani et al., "Measurement of Boron and Carbon Fluxes in Cosmic Rays with the PAMELA Experiment", ApJ **791**, 93, 93 (2014).

[49] M. Ackermann et al., "Inferred Cosmic-Ray Spectrum from Fermi Large Area Telescope γ-Ray Observations of Earth's Limb", Phys. Rev. Lett. **112**, 151103, 151103 (2014).

[50] M. Aguilar et al., "Precision Measurement of the Helium Flux in Primary Cosmic Rays of Rigidities 1.9 GV to 3 TV with the Alpha Magnetic Spectrometer on the International Space Station", Phys. Rev. Lett. **115**, 211101, 211101 (2015).

[51] W. R. Binns et al., "Observation of the ^{60}Fe nucleosynthesis-clock isotope in galactic cosmic rays", Science **352**, 677–680 (2016).

[52] G. V. Kulikov and G. B. Khristiansen, "On the size spectrum of extensive air showers", Soviet Physics JETP **8**, 441–444 (1959).

[53] M. A. Lawrence, R. J. O. Reid, and A. A. Watson, "The cosmic ray energy spectrum above 4×10^{17} eV as measured by the Haverah Park array", Journal of Physics G Nuclear Physics **17**, 733–757 (1991).

[54] M. Nagano et al., "Energy spectrum of primary cosmic rays above $10^{17.0}$ eV determined from extensive air shower experiments at Akeno", Journal of Physics G Nuclear Physics **18**, 423–442 (1992).

[55] D. J. Bird et al., "Evidence for correlated changes in the spectrum and composition of cosmic rays at extremely high energies", Phys. Rev. Lett. **71**, 3401–3404 (1993).

[56] D. J. Bird et al., "The Cosmic-Ray Energy Spectrum Observed by the Fly's Eye", ApJ **424**, 491 (1994).

[57] M. Ave et al., "The energy spectrum of cosmic rays in the range 3×10^{17}-4×10^{18} eV as measured with the Haverah Park array", Astroparticle Physics **19**, 47–60 (2003).

[58] A. M. Hillas, "The Origin of Ultra-High-Energy Cosmic Rays", ARA&A **22**, 425–444 (1984).

[59] K. V. Ptitsyna and S. V. Troitsky, "Physical conditions in potential accelerators of ultra-high-energy cosmic rays: updated Hillas plot and radiation-loss constraints", Physics Uspekhi **53**, 691–701 (2010).

[60] B. Peters, "Primary cosmic radiation and extensive air showers", Il Nuovo Cimento **22**, 800–819 (1961).

[61] T. K. Gaisser, "The Cosmic-ray Spectrum: from the knee to the ankle", in Journal of physics conference series, Vol. 47, Journal of Physics Conference Series (Oct. 2006), pages 15–20.

[62] M. Takeda et al., "Energy determination in the Akeno Giant Air Shower Array experiment", Astroparticle Physics **19**, 447–462 (2003).

[63] R. Abbasi et al., "Observation of the ankle and evidence for a high-energy break in the cosmic ray spectrum", Physics Letters B **619**, 271–280 (2005).

[64] A. Aab et al., "Features of the Energy Spectrum of Cosmic Rays above 2.5 $\times 10^{18}$ eV Using the Pierre Auger Observatory", Phys. Rev. Lett. **125**, 121106, 121106 (2020).

[65] A. Aab et al., "Measurement of the cosmic-ray energy spectrum above 2.5 $\times 10^{18}$ eV using the Pierre Auger Observatory", Phys. Rev. D **102**, 062005, 062005 (2020).

[66] K. Greisen, "End to the Cosmic-Ray Spectrum?", Phys. Rev. Lett. **16**, 748–750 (1966).

[67] G. T. Zatsepin and V. A. Kuz'min, "Upper Limit of the Spectrum of Cosmic Rays", Soviet Journal of Experimental and Theoretical Physics Letters **4**, 78 (1966).

[68] Y. Génolini et al., "Current status and desired precision of the isotopic production cross sections relevant to astrophysics of cosmic rays: Li, Be, B, C, and N", Phys. Rev. C **98**, 034611, 034611 (2018).

[69] R. Alves Batista et al., "Open questions in cosmic-ray research at ultrahigh energies", Frontiers in Astronomy and Space Sciences **6**, 23, 23 (2019).

[70] H. Dembinski et al., "Data-driven model of the cosmic-ray flux and mass composition from 10 GeV to 10^{11} GeV", in 35th international cosmic ray conference (icrc2017), Vol. 301, International Cosmic Ray Conference (Jan. 2017), page 533.

[71] K. Kotera and A. V. Olinto, "The Astrophysics of Ultrahigh-Energy Cosmic Rays", ARA&A **49**, 119–153 (2011).

[72] T. K. Gaisser and M. Honda, "Flux of atmospheric neutrinos", Annual Review of Nuclear and Particle Science **52**, 153–199 (2002).

[73] J. R. Hörandel, "On the knee in the energy spectrum of cosmic rays", Astroparticle Physics **19**, 193–220 (2003).

[74] V. I. Zatsepin and N. V. Sokolskaya, "Three component model of cosmic ray spectra from 10 GeV to 100 PeV", A&A **458**, 1–5 (2006).

[75] T. K. Gaisser, "Spectrum of cosmic-ray nucleons, kaon production, and the atmospheric muon charge ratio", Astroparticle Physics **35**, 801–806 (2012).

[76] T. K. Gaisser, T. Stanev, and S. Tilav, "Cosmic ray energy spectrum from measurements of air showers", Frontiers of Physics **8**, 748–758 (2013).

[77] K. Greisen, "Cosmic Ray Showers", Annual Review of Nuclear and Particle Science **10**, 63–108 (1960).

[78] T. K. Gaisser, *Cosmic Rays and Particle Physics* (1991).

[79] J. Matthews, "A Heitler model of extensive air showers", Astroparticle Physics **22**, 387–397 (2005).

[80] H. J. Bhabha and W. Heitler, "The Passage of Fast Electrons and the Theory of Cosmic Showers", Proceedings of the Royal Society of London Series A **159**, 432–458 (1937).

[81] J. F. Carlson and J. R. Oppenheimer, "On Multiplicative Showers", Physical Review **51**, 220–231 (1937).

[82] B. Rossi and K. Greisen, "Cosmic-Ray Theory", Reviews of Modern Physics **13**, 240–309 (1941).

[83] K. Kamata and J. Nishimura, "The Lateral and the Angular Structure Functions of Electron Showers", Progress of Theoretical Physics Supplement **6**, 93–155 (1958).

[84] J. Nishimura and K. Kamata, "On the Theory of Cascade Showers, I", Progress of Theoretical Physics **7**, 185–192 (1952).

[85] "43 - The Angular Distribution of the Shower Particles", in *Collected papers of L.D. Landau*, edited by D. ter Haar (Pergamon, 1965), pages 280–288.

[86] J. Nishimura, "Theory of cascade showers", in *Kosmische Strahlung II / Cosmic Rays II*, edited by K. Sitte (Springer Berlin Heidelberg, Berlin, Heidelberg, 1967), pages 1–114.

[87] K.-H. Kampert and M. Unger, "Measurements of the cosmic ray composition with air shower experiments", Astroparticle Physics **35**, 660–678 (2012).

[88] H. P. Dembinski et al., "Report on Tests and Measurements of Hadronic Interaction Properties with Air Showers", in European physical journal web of conferences, Vol. 210, European Physical Journal Web of Conferences (Oct. 2019), page 02004.

[89] L. Cazon, "Working Group Report on the Combined Analysis of Muon Density Measurements from Eight Air Shower Experiments", in 36th international cosmic ray conference (icrc2019), Vol. 36, International Cosmic Ray Conference (July 2019), page 214.

[90] L. Landau and G. Rumer, "The Cascade Theory of Electronic Showers", Proceedings of the Royal Society of London Series A **166**, 213–228 (1938).

[91] H. V. Bradt and S. A. Rappaport, "Three-Dimensional Monte Carlo Simulation of Extensive Air Showers", Physical Review **164**, 1567–1583 (1967).

[92] P. K. F. Grieder, "The relation between extensive air shower data and high-energy particle production models", Nuovo Cimento Rivista Serie **7**, 1–79 (1977).

[93] R. Engel, D. Heck, and T. Pierog, "Extensive Air Showers and Hadronic Interactions at High Energy", Annual Review of Nuclear and Particle Science **61**, 467–489 (2011).

[94] T. Pierog et al., "EPOS LHC: Test of collective hadronization with data measured at the CERN Large Hadron Collider", Phys. Rev. C **92**, 034906, 034906 (2015).

[95] S. Ostapchenko, "Monte Carlo treatment of hadronic interactions in enhanced Pomeron scheme: QGSJET-II model", Phys. Rev. D **83**, 014018, 014018 (2011).

[96] A. Fedynitch et al., "Hadronic interaction model sibyll 2.3c and inclusive lepton fluxes", Phys. Rev. D **100**, 103018, 103018 (2019).

[97] S. Roesler, R. Engel, and J. Ranft, "DPMJET-III, a hadronic interaction model for cascade simulations", in International cosmic ray conference, Vol. 2, International Cosmic Ray Conference (Jan. 2001), page 439.

[98] A. Fedynitch et al., "Calculation of conventional and prompt lepton fluxes at very high energy", in European physical journal web of conferences, Vol. 99, European Physical Journal Web of Conferences (Aug. 2015), page 08001.

[99] D. Heck et al., "CORSIKA: A Monte Carlo code to simulate extensive air showers", (1998).

[100] S. J. Sciutto, "AIRES: A system for air shower simulations", arXiv e-prints, astro-ph/9911331, astro–ph/9911331 (1999).

[101] T. Sako et al., "COSMOS X as a general purpose air shower simulation tool", PoS **ICRC2021**, 431 (2021).

[102] F. G. Schroeder, "The Surface Array planned for IceCube-Gen2", PoS **ICRC2021**, 407 (2021).

[103] D. Kostunin et al., "New insights from old cosmic rays: A novel analysis of archival KASCADE data", PoS **ICRC2021**, 319 (2021).

[104] F. G. Schröder, "News from Cosmic Ray Air Showers (ICRC 2019 – Cosmic Ray Indirect Rapport)", arXiv e-prints, arXiv:1910.03721, arXiv:1910.03721 (2019).

[105] Pierre Auger Collaboration et al., "Observation of a large-scale anisotropy in the arrival directions of cosmic rays above 8×10^{18} eV", Science **357**, 1266–1270 (2017).

[106] A. Bracco et al., "Discovery of a 30-degree-long ultraviolet arc in Ursa Major", A&A **636**, L8, L8 (2020).

[107] W. Baade and F. Zwicky, "Cosmic Rays from Super-novae", Proceedings of the National Academy of Science **20**, 259–263 (1934).

[108] V. Berezinsky, "Extragalactic cosmic rays and their signatures", Astroparticle Physics **53**, 120–129 (2014).

[109] A. A. Abdo et al., "Detection of the Small Magellanic Cloud in gamma-rays with Fermi/LAT", A&A **523**, A46, A46 (2010).

[110] R.-z. Yang, E. de Oña Wilhelmi, and F. Aharonian, "Probing cosmic rays in nearby giant molecular clouds with the Fermi Large Area Telescope", A&A **566**, A142, A142 (2014).

[111] M. Ackermann et al., "Detection of the Characteristic Pion-Decay Signature in Supernova Remnants", Science **339**, 807–811 (2013).

[112] HESS Collaboration et al., "Acceleration of petaelectronvolt protons in the Galactic Centre", Nature **531**, 476–479 (2016).

[113] Lhaaso Collaboration et al., "Peta-electron volt gamma-ray emission from the Crab Nebula", Science **373**, 425–430 (2021).

[114] Z. Cao et al., "Ultrahigh-energy photons up to 1.4 petaelectronvolts from 12 γ-ray Galactic sources", Nature **594**, 33–36 (2021).

[115] H. Abdalla et al., "A very-high-energy component deep in the γ-ray burst afterglow", Nature **575**, 464–467 (2019).

[116] M. G. Aartsen et al., "Time-Integrated Neutrino Source Searches with 10 Years of IceCube Data", Phys. Rev. Lett. **124**, 051103, 051103 (2020).

[117] IceCube Collaboration et al., "Multimessenger observations of a flaring blazar coincident with high-energy neutrino IceCube-170922A", Science **361**, eaat1378, eaat1378 (2018).

[118] R. Stein et al., "A tidal disruption event coincident with a high-energy neutrino", Nature Astronomy **5**, 510–518 (2021).

[119] IceCube Collaboration et al., "Neutrino emission from the direction of the blazar TXS 0506+056 prior to the IceCube-170922A alert", Science **361**, 147–151 (2018).

[120] A. Plavin et al., "Observational Evidence for the Origin of High-energy Neutrinos in Parsec-scale Nuclei of Radio-bright Active Galaxies", ApJ **894**, 101, 101 (2020).

[121] X. Rodrigues et al., "Multiwavelength and Neutrino Emission from Blazar PKS 1502 + 106", ApJ **912**, 54, 54 (2021).

[122] P. Picozza et al., "PAMELA A payload for antimatter matter exploration and light-nuclei astrophysics", Astroparticle Physics **27**, 296–315 (2007).

[123] R. Battiston, "The antimatter spectrometer (AMS-02): A particle physics detector in space", Nuclear Instruments and Methods in Physics Research A **588**, 227–234 (2008).

[124] A. Kounine, "The Alpha Magnetic Spectrometer on the International Space Station", International Journal of Modern Physics E **21**, 1230005, 1230005 (2012).

[125] S. Torii and Calet Collaboration, "The CALorimetric Electron Telescope (CALET): a High-Energy Astroparticle Physics Observatory on the International Space Stati", in 34th international cosmic ray conference (icrc2015), Vol. 34, International Cosmic Ray Conference (July 2015), page 581.

[126] J. Chang et al., "The DArk Matter Particle Explorer mission", Astroparticle Physics **95**, 6–24 (2017).

[127] P. K. F. Grieder, *Extensive Air Showers* (2010).

[128] T. Antoni et al., "The cosmic-ray experiment KASCADE", Nuclear Instruments and Methods in Physics Research A **513**, 490–510 (2003).

[129] The Pierre Auger Collaboration et al., "The Pierre Auger Observatory Upgrade - Preliminary Design Report", arXiv e-prints, arXiv:1604.03637, arXiv:1604.03637 (2016).

[130] J. B. Birks, *The theory and practice of scintillation counting* (Pergamon Press, 1964).

[131] G. Aielli et al., "Layout and performance of RPCs used in the Argo-YBJ experiment", Nuclear Instruments and Methods in Physics Research A **562**, 92–96 (2006).

[132] P. Fonte, "Survey of physical modelling in Resistive Plate Chambers", Journal of Instrumentation **8**, P11001, P11001 (2013).

[133] J. V. Jelley, *Čerenkov radiation and its applications* (Pergamon Press, 1958).

[134] Pierre Auger Collaboration et al., "The surface detector system of the Pierre Auger Observatory", Nuclear Instruments and Methods in Physics Research A **586**, 409–420 (2008).

[135] R. Abbasi et al., "IceTop: The surface component of IceCube", Nuclear Instruments and Methods in Physics Research A **700**, 188–220 (2013).

[136] M. Ave et al., "The accuracy of signal measurement with the water Cherenkov detectors of the Pierre Auger Observatory", Nuclear Instruments and Methods in Physics Research A **578**, 180–184 (2007).

[137] J. E. Dickinson, "Studies of the mass composition of cosmic rays with the SPASE-2/VULCAN instrument at the South Pole", in 26th international cosmic ray conference (icrc26), volume 3, Vol. 3, International Cosmic Ray Conference (Aug. 1999), page 136.

[138] D. Kostunin et al., "Tunka Advanced Instrument for cosmic rays and Gamma Astronomy", in Journal of physics conference series, Vol. 1263, Journal of Physics Conference Series (June 2019), page 012006.

[139] A. A. Ivanov, S. V. Matarkin, and L. V. Timofeev, "Measuring temporal characteristics of the Cherenkov radiation signal from extensive air showers of cosmic rays with a wide field-of-view telescope addendum to the Yakutsk array", arXiv e-prints, arXiv:2111.11587, arXiv:2111.11587 (2021).

[140] R. Mirzoyan, "Brief history of ground-based very high energy gamma-ray astrophysics with atmospheric air Cherenkov telescopes", Astroparticle Physics **53**, 91–99 (2014).

[141] Cherenkov Telescope Array Consortium et al., *Science with the Cherenkov Telescope Array* (2019).

[142] J. Abraham et al., "The fluorescence detector of the Pierre Auger Observatory", Nuclear Instruments and Methods in Physics Research A **620**, 227–251 (2010).

[143] A. Aab et al., "Depth of maximum of air-shower profiles at the Pierre Auger Observatory. I. Measurements at energies above 1 $0^{17.8}$ eV", Phys. Rev. D **90**, 122005, 122005 (2014).

[144] T. Huege, "Radio detection of cosmic ray air showers in the digital era", Phys. Rep. **620**, 1–52 (2016).

[145] F. G. Schröder, "Radio detection of cosmic-ray air showers and high-energy neutrinos", Progress in Particle and Nuclear Physics **93**, 1–68 (2017).

[146] R. A. Millikan and G. H. Cameron, "The Origin of the Cosmic Rays", Physical Review **32**, 533–557 (1928).

[147] E. Fermi, "On the Origin of the Cosmic Radiation", Physical Review **75**, 1169–1174 (1949).

[148] V. L. Ginzburg and S. I. Syrovatskii, *The Origin of Cosmic Rays* (1964).

[149] H. Dembinski et al., "The Muon Puzzle in air showers and its connection to the LHC", PoS **ICRC2021**, 037 (2021).

[150] *Attenuation by atmospheric gases and related effects. Recommendation P.676-12* (ITU, Geneva, Switzerland, Aug. 2019).

[151] F. D. Kahn and I. Lerche, "Radiation from Cosmic Ray Air Showers", Proceedings of the Royal Society of London Series A **289**, 206–213 (1966).

[152] S. A. Colgate, "The detection of high-energy cosmic-ray showers by the combined optical and electromagnetic pulse", J. Geophys. Res. **72**, 4869–4879 (1967).

[153] T. Huege, "Theory and simulations of air shower radio emission", in 5th international workshop on acoustic and radio eev neutrino detection activities: arena 2012, Vol. 1535, edited by R. Lahmann et al., American Institute of Physics Conference Series (May 2013), pages 121–127.

[154] J. D. Jackson, *Classical Electrodynamics, 3rd Edition* (1998).

[155] R. P. Feynman, *Feynman lectures on physics - Volume 1* (1963).

[156] L. D. Landau and E. M. Lifshitz, *The classical theory of fields* (1975).

[157] J. Clay and H. P. Berlage, "Variation der Ultrastrahlung mit der geographischen Breite und dem Erdmagnetismus", Naturwissenschaften **20**, 687–688 (1932).

[158] A. H. Compton, "Variation of the Cosmic Rays with Latitude", Physical Review **41**, 111–113 (1932).

[159] G. A. Askar'yan, "Excess negative charge of an electron-photon shower and its coherent radio emission", Soviet Physics JETP **14**, 441–443 (1962).

[160] J. V. Jelley et al., "Radio Pulses from Extensive Cosmic-Ray Air Showers", Nature **205**, 327–328 (1965).

[161] G. A. Askar'yan, "Coherent radio emission from cosmic showers in air and in dence media", Soviet Physics JETP **21**, 658–659 (1965).

[162] H. R. Allan, "Radio emission from extensive air showers", Prog. in Element. Part. and Cos. Ray Phys. **10** (1971).

[163] D. Saltzberg et al., "Observation of the Askaryan Effect: Coherent Microwave Cherenkov Emission from Charge Asymmetry in High-Energy Particle Cascades", Phys. Rev. Lett. **86**, 2802–2805 (2001).

[164] C. Glaser et al., "Simulation of radiation energy release in air showers", J. Cosmology Astropart. Phys. **2016**, 024, 024 (2016).

[165] L. B. Okun, "Comments on Testing Charge Conservation and Pauli Exclusion Principle", Comments Nucl. Part. Phys. **19**, 99–116 (1989).

[166] M. Agostini et al., "Test of Electric Charge Conservation with Borexino", Phys. Rev. Lett. **115**, 231802, 231802 (2015).

[167] N. N. Bogoliubov and D. V. Shirkov, *Quantum fields* (1982).

[168] V. L. Ginzburg and V. N. Tsytovich, *Transition radiation and transition scattering.* (1990).

[169] G. A. Gusev et al., "Possibility of studying cosmic rays with energies $> 10^{20}$ eV", Soviet Journal of Experimental and Theoretical Physics Letters **36**, 268–271 (1982).

[170] R. Šmída et al., "Observation of microwave emission from extensive air showers with CROME", in European physical journal web of conferences, Vol. 53, European Physical Journal Web of Conferences (June 2013), page 08010.

[171] D. Kostunin, "Reconstruction of air-shower parameters with a sparse radio array", PhD thesis (2015).

[172] H. R. Allan, "The Lateral Distribution of the Radio Emission, and its Dependence on the Longitudinal Structure of the Air Shower.", in 12th international cosmic ray conference (icrc12), volume 3, Vol. 3, International Cosmic Ray Conference (Jan. 1971), page 1108.

[173] H. R. Allan, "Radio Emission and the Structure of the Shower Disc.", in 12th international cosmic ray conference (icrc12), volume 3, Vol. 3, International Cosmic Ray Conference (Jan. 1971), page 1113.

[174] A. Aab et al., "Energy estimation of cosmic rays with the Engineering Radio Array of the Pierre Auger Observatory", Phys. Rev. D **93**, 122005, 122005 (2016).

[175] P. Schellart et al., "Polarized radio emission from extensive air showers measured with LOFAR", J. Cosmology Astropart. Phys. **2014**, 014, 014 (2014).

[176] H. R. Allan and K. P. Neat, "Mechanism of Radio Emission from Extensive Air Showers", Nature **215**, 267–268 (1967).

[177] W. E. Hazen et al., "Polarization of Radio Pulses from Extensive Air Showers", Phys. Rev. Lett. **22**, 35–37 (1969).

[178] H. R. Allan and R. W. Clay, "Radio Pulse Production in Extensive Air Showers", Nature **222**, 635–637 (1969).

[179] H. R. Allan et al., "The Mechanism of EAS Radio Emission.", in 12th international cosmic ray conference (icrc12), volume 3, Vol. 3, International Cosmic Ray Conference (Jan. 1971), page 1097.

[180] J. R. Prescott, J. H. Hough, and J. K. Pidcock, "Properties of radio emission of extensive air showers", in International cosmic ray conference, Vol. 29, International Cosmic Ray Conference (Jan. 1970), page 717.

[181] J. R. Prescott, J. H. Hough, and J. K. Pidcock, "Mechanism of Radio Emission from Extensive Air Showers", Nature Physical Science **233**, 109–110 (1971).

[182] H. Schoorlemmer and Pierre Auger Collaboration, "Results from polarization studies of radio signals induced by cosmic rays at the Pierre Auger Observatory", Nuclear Instruments and Methods in Physics Research A **662**, S134–S137 (2012).

[183] A. Aab et al., "Probing the radio emission from air showers with polarization measurements", Phys. Rev. D **89**, 052002, 052002 (2014).

[184] A. Bellétoile et al., "Evidence for the charge-excess contribution in air shower radio emission observed by the CODALEMA experiment", Astroparticle Physics **69**, 50–60 (2015).

[185] O. Scholten et al., "Measurement of the circular polarization in radio emission from extensive air showers confirms emission mechanisms", Phys. Rev. D **94**, 103010, 103010 (2016).

[186] E. Zas, F. Halzen, and T. Stanev, "Electromagnetic pulses from high-energy showers: Implications for neutrino detection", Phys. Rev. D **45**, 362–376 (1992).

[187] C. W. James et al., "General description of electromagnetic radiation processes based on instantaneous charge acceleration in "endpoints"", Phys. Rev. E **84**, 056602, 056602 (2011).

[188] O. Scholten, K. Werner, and F. Rusydi, "A macroscopic description of coherent geo-magnetic radiation from cosmic-ray air showers", Astroparticle Physics **29**, 94–103 (2008).

[189] K. Werner, K. D. de Vries, and O. Scholten, "A realistic treatment of geomagnetic Cherenkov radiation from cosmic ray air showers", Astroparticle Physics **37**, 5–16 (2012).

[190] T. Pierog et al., "First results of fast one-dimensional hybrid simulation of EAS using CONEX", Nuclear Physics B Proceedings Supplements **151**, 159–162 (2006).

[191] J. Alvarez-Muñiz, W. R. Carvalho, and E. Zas, "Monte Carlo simulations of radio pulses in atmospheric showers using ZHAireS", Astroparticle Physics **35**, 325–341 (2012).

[192] K. Belov, "Radio emission from air showers. Comparison of theoretical approaches", in 5th international workshop on acoustic and radio eev neutrino detection activities: arena 2012, Vol. 1535, edited by R. Lahmann et al., American Institute of Physics Conference Series (May 2013), pages 157–161.

[193] P. A. Bezyazeekov et al., "Measurement of cosmic-ray air showers with the Tunka Radio Extension (Tunka-Rex)", Nuclear Instruments and Methods in Physics Research A **802**, 89–96 (2015).

[194] *Radio noise. Recommendation P.372-14* (ITU, Geneva, Switzerland, Aug. 2019).

[195] A. Aab et al., "Measurement of the Radiation Energy in the Radio Signal of Extensive Air Showers as a Universal Estimator of Cosmic-Ray Energy", Phys. Rev. Lett. **116**, 241101, 241101 (2016).

[196] M. Gottowik et al., "Determination of the absolute energy scale of extensive air showers via radio emission: Systematic uncertainty of underlying first-principle calculations", Astroparticle Physics **103**, 87–93 (2018).

[197] K. Mulrey et al., "On the cosmic-ray energy scale of the LOFAR radio telescope", PoS **ICRC2021**, 371 (2021).

[198] A. Rehman et al., "Classification and Denoising of Cosmic-Ray Radio Signals using Deep Learning", PoS **ICRC2021**, 417 (2021).

[199] P. Bezyazeekov et al., "Reconstruction of sub-threshold events of cosmic-ray radio detectors using an autoencoder", PoS **ICRC2021**, 223 (2021).

[200] A. Aab et al., "Observation of inclined EeV air showers with the radio detector of the Pierre Auger Observatory", J. Cosmology Astropart. Phys. **2018**, 026, 026 (2018).

[201] F. Schlüter et al., "Refractive displacement of the radio-emission footprint of inclined air showers simulated with CoREAS", European Physical Journal C **80**, 643, 643 (2020).

[202] Pierre Auger Collaboration, "The Pierre Auger Cosmic Ray Observatory", Nuclear Instruments and Methods in Physics Research A **798**, 172–213 (2015).

[203] Pierre Auger Collaboration et al., "Prototype muon detectors for the AMIGA component of the Pierre Auger Observatory", Journal of Instrumentation **11**, P02012 (2016).

[204] A. Aab et al., "Design and implementation of the AMIGA embedded system for data acquisition", Journal of Instrumentation **16**, T07008, T07008 (2021).

[205] H. Klages and Pierre Auger Collaboration, "Enhancements to the Southern Pierre Auger Observatory", in Journal of physics conference series, Vol. 375, Journal of Physics Conference Series (July 2012), page 052006.

[206] P. Abreu et al., "Antennas for the detection of radio emission pulses from cosmic-ray induced air showers at the Pierre Auger Observatory", Journal of Instrumentation **7**, P10011 (2012).

[207] B. Dawson, "The Energy Scale of the Pierre Auger Observatory", in 36th international cosmic ray conference (icrc2019), Vol. 36, International Cosmic Ray Conference (July 2019), page 231.

[208] M. Gottowik, "Measurements of Inclined Air Showers with the Auger Engineering Radio Array at the Pierre Auger Observatory", in 36th international cosmic ray conference (icrc2019), Vol. 36, International Cosmic Ray Conference (July 2019), page 274.

[209] B. Pont, "A Large Radio Detector at the Pierre Auger Observatory - Measuring the Properties of Cosmic Rays up to the Highest Energies", in 36th international cosmic ray conference (icrc2019), Vol. 36, International Cosmic Ray Conference (July 2019), page 395.

[210] A. Aab et al., "Data-driven estimation of the invisible energy of cosmic ray showers with the Pierre Auger Observatory", Phys. Rev. D **100**, 082003, 082003 (2019).

[211] W. D. Apel et al., "The KASCADE-Grande experiment", Nuclear Instruments and Methods in Physics Research A **620**, 202–216 (2010).

[212] W. D. Apel et al., "A comparison of the cosmic-ray energy scales of Tunka-133 and KASCADE-Grande via their radio extensions Tunka-Rex and LOPES", Physics Letters B **763**, 179–185 (2016).

[213] C. Glaser, "Absolute energy calibration of the pierre auger observatory using radio emission of extensive air showers", PhD thesis (RWTH Aachen University, 2017).

[214] F. Briechle, "Measurement of the radiation energy releaseusing radio emission from extensive air showersat the pierre auger observatory", PhD thesis (RWTH Aachen University, 2021).

[215] F. James, *Statistical Methods in Experimental Physics: 2nd Edition* (2006).

[216] H. Dembinski, P. Ongmongkolkul, and et al., "Scikit-hep/iminuit", `10.5281/zenodo.4310361` (2020).

[217] D. Foreman-Mackey et al., "emcee: The MCMC Hammer", PASP **125**, 306 (2013).

[218] D. Foreman-Mackey et al., "emcee v3: A Python ensemble sampling toolkit for affine-invariant MCMC", The Journal of Open Source Software **4**, 1864, 1864 (2019).

[219] E. M. Holt, "Combined detection of muons and radio emission of cosmic-ray air showers", PhD thesis (2018).

[220] P. A. Bezyazeekov et al., "Radio measurements of the energy and the depth of the shower maximum of cosmic-ray air showers by Tunka-Rex", J. Cosmology Astropart. Phys. **2016**, 052, 052 (2016).

[221] A. Chulliat et al., *The US/UK World Magnetic Model for 2015-2020: Technical Report*, National Geophysical Data Center, NOAA, Technical Report, 2015.

[222] W. D. Apel et al., "Final results of the LOPES radio interferometer for cosmic-ray air showers", European Physical Journal C **81**, 176, 176 (2021).

[223] F. G. Schroeder, "The Surface Array planned for IceCube-Gen2 (ICRC 2021)", arXiv e-prints, arXiv:2108.00364, arXiv:2108.00364 (2021).

[224] K. Kotera, "The Giant Radio Array for Neutrino Detection (GRAND) Project", arXiv e-prints, arXiv:2108.00032, arXiv:2108.00032 (2021).

[225] A. Escudie et al., "From the Observation of UHECR Radio Signal in [1-200] MHz to the Composition: CODALEMA and EXTASIS Status Report", in 36th international cosmic ray conference (icrc2019), Vol. 36, International Cosmic Ray Conference (July 2019), page 246.

[226] M. P. van Haarlem et al., "LOFAR: The LOw-Frequency ARray", A&A **556**, A2, A2 (2013).

[227] K. Plant et al., "Updates from the OVRO-LWA: Commissioning a Full-Duty-Cycle Radio-Only Cosmic Ray Detector", PoS **ICRC2021**, 204 (2021).

[228] D. V. Chernov et al., "The Tunka Experiment:. Towards a 1-KM^2 Cherenkov EAS Array in the Tunka Valley", International Journal of Modern Physics A **20**, 6796–6798 (2005).

[229] N. Budnev et al., "Tunka-25 Air Shower Cherenkov array: The main results", Astroparticle Physics **50**, 18–25 (2013).

[230] V. V. Prosin et al., "Depth of the Maximum of Extensive Air Showers (EASes) and the Mean Mass Composition of Primary Cosmic Rays in the 1015–1018 eV Range of Energies, According to Data from the TUNKA-133 and TAIGA-HiSCORE Arrays for Detecting EAS Cherenkov Light in the Tunkinsk Valley", Bulletin of the Russian Academy of Sciences, Physics **85**, 395–397 (2021).

[231] N. M. Budnev et al., "Tunka-133 EAS Cherenkov Array: Status of 2007", in International cosmic ray conference, Vol. 5, International Cosmic Ray Conference (Jan. 2008), pages 973–976.

[232] R. D. Monkhoev et al., "The Tunka-Grande experiment", Journal of Instrumentation **12**, C06019 (2017).

[233] R. D. Monkhoev et al., "The Tunka-Grande experiment: Status and prospects", Bulletin of the Russian Academy of Sciences, Physics **81**, 468–470 (2017).

[234] V. V. Prosin et al., "Energy Spectrum of Primary Cosmic Rays, According to TUNKA-133 and TAIGA-HiSCORE EAS Cherenkov Light Data", Bulletin of the Russian Academy of Sciences, Physics **83**, 1016–1019 (2019).

[235] V. Lenok, "Modeling the Aperture of Radio Instruments for Air-Shower Detection", in 36th international cosmic ray conference (icrc2019), Vol. 36, International Cosmic Ray Conference (July 2019), page 331.

[236] S. Argirò et al., "The offline software framework of the Pierre Auger Observatory", Nuclear Instruments and Methods in Physics Research A **580**, 1485–1496 (2007).

[237] R. Hiller et al., "Calibration of the absolute amplitude scale of the Tunka Radio Extension (Tunka-Rex)", in 34th international cosmic ray conference (icrc2015), Vol. 34, International Cosmic Ray Conference (July 2015), page 573.

[238] P. A. Bezyazeekov et al., "Reconstruction of cosmic ray air showers with Tunka-Rex data using template fitting of radio pulses", Phys. Rev. D **97**, 122004, 122004 (2018).

[239] V. Lenok et al., "Estimation of aperture of the Tunka-Rex radio array for cosmic-ray air-shower measurements", PoS **ICRC2021**, 210 (2021).

[240] F. James and M. Roos, "Minuit — A System for Function Minimization and Analysis of the Parameter Errors and Correlations", Computer Physics Communications **10**, 343–367 (1975).

[241] V. Koroliuk et al., *Handbook of probability theory and mathematical statistics* (Nauka, 1985).

[242] M. Springer, *The algebra of random variables*, Probability and Statistics Series (Wiley, 1979).

[243] D. Scott, *Multivariate density estimation: theory, practice, and visualization* (Wiley, 1992).

[244] A. S. Leszczyńska, "Potential of the IceTop Enhancement with a Scintillation Detector Array", 51.13.04; LK 01, PhD thesis (Karlsruher Institut für Technologie (KIT), 2021), 121 pages.

[245] P. Abreu et al., "The exposure of the hybrid detector of the Pierre Auger Observatory", Astroparticle Physics **34**, 368–381 (2011).

[246] V. Lenok et al., "Current Status and New Challenges of The Tunka Radio Extension", in Journal of physics conference series, Vol. 1181, Journal of Physics Conference Series (Feb. 2019), page 012027.

[247] C. H. L. Beentjes, "Quadrature on a spherical surface", in (2016).

[248] C. Ahrens and G. Beylkin, "Rotationally invariant quadratures for the sphere", Proceedings of the Royal Society of London Series A **465**, 3103–3125 (2009).

[249] D. Kostunin et al., "Seven years of Tunka-Rex operation", in 36th international cosmic ray conference (icrc2019), Vol. 36, International Cosmic Ray Conference (July 2019), page 319.

[250] H. Schoorlemmer et al., "Energy and flux measurements of ultra-high energy cosmic rays observed during the first ANITA flight", Astroparticle Physics **77**, 32–43 (2016).

ACKNOWLEDGMENT

There are many people who I ought to acknowledge for making this work possible and who assisted me during the writing of my dissertation.

First, I want to thank my referee, Prof. Dr. Frank G. Schöder, who became an Assistant Professor in University of Delaware, USA, during my PhD studies, for giving me an opportunity to working on this project, Prof. Dr. Ralph Engel for acting as my co-referee, and the German Academic Exchange Service (DAAD) for funding my research.

Prof. Dr. Frank G. Schröder played a big role in the present work, especially with his broad experience in all aspects of the observations of the cosmic-ray radio emission and related instrumentation.

Dmitriy Kostunin, the PI of Tunka-Rex and my consultant throughout my work on the Tunka-Rex analysis and the efficiency model, contributed the most in the present work. His background in theoretical physics and programming helped me in the very beginning of my work in KIT.

Moreover, I want to thank all my colleagues in the cosmic-ray technology group at KIT and especially Andreas Haungs, the leader of the group, for his positive and enthusiastic approach to all things and Tim Huege, guru of CoREAS, who gave me many insights into the computing of the air-shower radio emission and its physics and for his large organizational and scientific support of the AERA related work. Very special thanks must go to Doris Wochele for providing any computing and data-storage capabilities that are possible in our institute and beyond and to Sabine Bucher for covering all administrative work and providing help on any question.

Three bright colleagues from the cosmic-ray community helped me a lot in the final stage of my PhD studies and I want to thank them for this: Hans Dembinski, who thoroughly checked the mathematical and physical correctness of the efficiency model, the core part of this work; Michael Unger, who thoroughly read the cosmic ray review chapter and clarified several important aspects which definitely improved the overall quality of the review, and Darko Veberic for valuable recommendations about the proper mathematical typesetting in physics.

I want to warmly thank Agnieszka Leszczyńska who supported me during my entire work in KIT with her bright outlook on the world, big enthusiasm towards science, and irresistible energy to work.

The most valuable acknowledgment ought to be paid to my mother, Galina Lenok, who always put knowledge and education above all else and who supported me during my entire PhD studies with all the ups and downs.

I am grateful to my teachers Nikolay Kirichkov, Alexander Vall, Maxim Polyakov, Mikhail Merkin, Nikolai Zamiatin, and Nina Ivanova, who showed me that physics is interesting and fascinating.

ERKLÄRUNG

Eggenstein-Leopoldshafen, den 29.11.2021

Erklärung der selbständigen Anfertigung meiner Dissertationsschrift

Hiermit versichere ich, dass ich die Dissertationsschrift mit dem Titel

Measurement of the Cosmic-Ray Energy Spectrum Using a Novel Approach to Model the Aperture of Radio Arrays

selbständig und ohne unerlaubte fremde Hilfe verfasst habe. Dabei habe ich keine anderen, als die von mir angegebenen Hilfsmittel benutzt.

Vladimir Lenok